

COMPRESSED SENSING BASED  
COMPUTERIZED TOMOGRAPHY IMAGING

A THESIS SUBMITTED TO  
THE GRADUATE SCHOOL OF NATURAL AND APPLIED SCIENCES  
OF  
MIDDLE EAST TECHNICAL UNIVERSITY

BY

AYDIN BİÇER

IN PARTIAL FULFILLMENT OF THE REQUIREMENTS  
FOR  
THE DEGREE OF DOCTOR OF PHILOSOPHY  
IN  
ELECTRICAL AND ELECTRONICS ENGINEERING

FEBRUARY 2012

Approval of the thesis:

**COMPRESSED SENSING BASED  
COMPUTERIZED TOMOGRAPHY IMAGING**

submitted by **AYDIN BİÇER** in partial fulfillment of the requirements for the degree of **Doctor of Philosophy in Electrical and Electronics Engineering Department, Middle East Technical University** by,

Prof. Dr. Canan Özgen \_\_\_\_\_  
Dean, Graduate School of **Natural and Applied Sciences**

Prof. Dr. İsmet Erkmen \_\_\_\_\_  
Head of Department, **Electrical and Electronics Engineering**

Prof. Dr. Zafer Ünver \_\_\_\_\_  
Supervisor, **Electrical and Electronics Engineering Dept., METU**

**Examining Committee Members:**

Prof. Dr. Tolga Çiloğlu \_\_\_\_\_  
Electrical and Electronics Engineering Dept., METU

Prof. Dr. Zafer Ünver \_\_\_\_\_  
Electrical and Electronics Engineering Dept., METU

Prof. Dr. Salim Kayhan \_\_\_\_\_  
Electrical and Electronics Engineering Dept., Hacettepe Univ.

Prof. Dr. Aydın Alatan \_\_\_\_\_  
Electrical and Electronics Engineering Dept., METU

Assist. Prof. Dr. Yeşim Serinağaoğlu \_\_\_\_\_  
Electrical and Electronics Engineering Dept., METU

**Date:** \_\_\_\_\_

**I hereby declare that all information in this document has been obtained and presented in accordance with academic rules and ethical conduct. I also declare that, as required by these rules and conduct, I have fully cited and referenced all material and results that are not original to this work.**

Name, Last name: AYDIN BİÇER

Signature :

# ABSTRACT

## COMPRESSED SENSING BASED COMPUTERIZED TOMOGRAPHY IMAGING

Biçer, Aydın

Ph.D., Department of Electrical and Electronics Engineering

Supervisor: Prof. Dr. Zafer Ünver

February 2012, 114 pages

There is no doubt that computerized tomography (CT) is highly beneficial for patients when used appropriately for diagnostic purposes. However, worries have been raised concerning the possible risk of cancer induction from CT because of the dramatic increase of CT usage in medicine. It is crucial to keep the radiation dose as low as reasonably achievable to reduce this probable risk. This thesis is about to reduce X-ray radiation exposure to patients and/or CT operators via a new imaging modality that exploits the recent compressed sensing (CS) theory. Two efficient reconstruction algorithms based on total variation (TV) minimization of estimated images are proposed. Using fewer measurements than the traditional filtered back projection based algorithms or algebraic reconstruction techniques require, the proposed algorithms allow reducing the radiation dose without sacrificing the CT image quality even in the case of noisy measurements. Employing powerful methods to solve the TV minimization problem, both schemes have higher reconstruction speed than the recently introduced CS based algorithms.

**Keywords:** Computerized tomography imaging, radiation absorption, compressed sensing, total variation.

## ÖZ

### SIKIŞTIRILMIŞ ALGILAMA TABANLI BİLGİSAYARLI TOMOGRAFİK GÖRÜNTÜLEME

Biçer, Aydın  
Doktora, Elektrik ve Elektronik Mühendisliği Bölümü  
Tez Yöneticisi: Prof. Dr. Zafer Ünver

Şubat 2012, 114 sayfa

Hastalık teşhisi için uygun olarak kullanıldığı takdirde Bilgisayarlı Tomografinin (BT) son derece yararlı olduğu tartışmasızdır. Ancak, tıpta kullanımının dramatik artışı sebebiyle BT'den kaynaklanan kanser riski ile ilgili endişeler artmaktadır. Söz konusu riskin azaltılmasında, radyasyon dozunun mümkün olan en düşük düzeyde tutulması çok önemlidir. Bu tez, güncel sıkıştırılmış algılama (SA) kuramından yararlanarak oluşturulmuş yeni bir imgeleme yöntemi ile hastaların ve/veya BT operatörlerinin maruz kaldığı X-ışını radyasyonunun azaltılması hakkındadır. Kestirilen imgenin toplam değişimini (TD) enküçültmeye dayalı iki verimli geriçatım algoritması önerilmektedir. Önerilen algoritmalar, süzgeçlenmiş geri izdüşüme dayalı geleneksel görüntü oluşturma algoritmalarından ve cebirsel geriçatım tekniklerinden daha az sayıda ölçüm kullanarak gürültülü ölçümlerde bile görüntü kalitesinden ödün vermeksizin radyasyon dozunu azaltmaya olanak sağlamaktadır. TD enküçültme problemini çözmek için güçlü yöntemler kullanan her iki yaklaşım, güncel SA tabanlı algoritmalarından daha yüksek geriçatım hızına sahiptir.

**Anahtar Kelimeler:** Bilgisayarlı tomografik görüntüleme, radyasyon Emilimi, sıkıştırılmış algılama, toplam değişim.

*To my daughter, Zeynep...*

## **ACKNOWLEDGEMENTS**

The author wishes to express his deepest gratitude to his supervisor Prof. Dr. Zafer ÜNVER for his guidance, advice, criticism and insight throughout the research.

The author would like to thank his wife and parents for love, freedom and support.

This study was supported in part by Aselsan Inc., MGEO Division, Image Processing Department, Turkey.

## TABLE OF CONTENTS

|  |      |
|--|------|
| ABSTRACT .....                               | iv   |
| ÖZ.....                                      | v    |
| DEDICATION .....                             | vi   |
| ACKNOWLEDGEMENTS .....                       | vii  |
| TABLE OF CONTENTS .....                      | viii |
| LIST OF TABLES .....                         | xi   |
| LIST OF FIGURES.....                         | xii  |
| NOMENCLATURE.....                            | xiv  |
| CHAPTERS                                     |      |
| 1. INTRODUCTION.....                         | 1    |
| 1.1 Data Acquisition .....                   | 1    |
| 1.2 Image Reconstruction .....               | 2    |
| 1.3 Cancer Risk in X-ray Imaging.....        | 4    |
| 1.4 Risk Reduction.....                      | 5    |
| 1.5 Compressed Sensing .....                 | 6    |
| 1.6 Compressed Sensing Based CT Imaging..... | 7    |
| 1.7 Contributions .....                      | 8    |
| 1.8 Organization of the Thesis.....          | 9    |
| 2. COMPUTERIZED TOMOGRAPHY IMAGING.....      | 11   |
| 2.1 Linear Imaging Model .....               | 11   |
| 2.2 Traditional Image Reconstruction .....   | 15   |



|       |   |    |
|-------|---|----|
| 2.3   | Algebraic Reconstruction Techniques .....                 | 18 |
| 2.3.1 | ART .....   | 18 |
| 2.3.2 | SART .....  | 19 |
| 2.3.3 | Numerical Illustrations .....                             | 20 |
| 3.    | COMPRESSED SENSING .....                                  | 24 |
| 3.1   | Introduction.....   | 24 |
| 3.2   | The Theory of CS .....                                    | 25 |
| 3.3   | Intuitive Examples of CS and Applications.....            | 27 |
| 4.    | COMPRESSED SENSING BASED CT IMAGING.....                  | 33 |
| 4.1   | Compressed Sensing for CT Imaging.....                    | 33 |
| 4.2   | POCS Based Solution .....                                 | 35 |
| 4.3   | Fourier Transform Based Solution .....                    | 38 |
| 5.    | SECOND ORDER CONE PROGRAMMING .....                       | 40 |
| 5.1   | General Perspective .....                                 | 40 |
| 5.2   | Problem Reformulation.....                                | 41 |
| 5.3   | Solution Algorithm .....                                  | 43 |
| 5.4   | Experimental Results .....                                | 45 |
| 5.4.1 | <i>E1</i> : Comparison with Conventional Techniques ..... | 46 |
| 5.4.2 | <i>E2</i> : Robustness Test in Large Scale Problems ..... | 49 |
| 5.4.3 | <i>E3</i> : Comparison with Other CS-Based Solutions..... | 51 |
| 6.    | FAST TOTAL VARIATION MINIMIZATION.....                    | 56 |
| 6.1   | Problem Reformulation.....                                | 56 |
| 6.2   | Quadratic Approximation .....                             | 59 |

|       |   |     |
|-------|---|-----|
| 6.3   | Conjugate Gradient Based Algorithm.....                   | 61  |
| 6.4   | Regularization Parameter.....                             | 63  |
| 6.5   | Experimental Results .....                                | 66  |
| 6.5.1 | <i>E1</i> : Comparison with FBP .....                     | 68  |
| 6.5.2 | <i>E2</i> : Extended Comparison with FBP .....            | 72  |
| 6.5.3 | <i>E3</i> : Robustness to Additive Noise .....            | 75  |
| 6.5.4 | <i>E4</i> : A Multi-Purpose Performance Test .....        | 78  |
| 6.5.5 | <i>E5</i> : Comparison with Other CS-Based Solutions..... | 81  |
| 7.    | CONCLUSIONS .....   | 85  |
|       | REFERENCES.....   | 89  |
|       | APPENDICES  |     |
| A.    | PROJECTION GEOMETRY .....                                 | 99  |
| A.1   | Ray Equation.....   | 99  |
| A.2   | Fan Beam Geometry .....                                   | 101 |
| B.    | LOGARITHMIC BARRIER METHOD FOR SOCP.....                  | 105 |
| B.1   | TV Minimization with Equality Constraints.....            | 105 |
| B.2   | TV Minimization with Quadratic Constraints .....          | 109 |
|       | CURRICULUM VITAE .....                                    | 114 |

## LIST OF TABLES

### TABLES

|   |     |
|---|-----|
| Table 2.1 Relative amounts of radiation absorbed .....                      | 17  |
| Table 3.1 1-D signal recovery errors, $\ x - s\ _2$ .....                   | 28  |
| Table 3.2 PSNRs (dB) of the 2-D signal recoveries .....                     | 32  |
| Table 5.1 Total number of Newton iterations in SOCP .....                   | 47  |
| Table 5.2 Parameters set in ASD-POCS and ASD-FT .....                       | 52  |
| Table 6.1 FTV Parameters setting in experiments .....                       | 68  |
| Table 6.2 PSNR versus relative radiation absorbed (RRA) .....               | 74  |
| Table 6.3 PSNRs of images reconstructed by FTV using noisy measurements ... | 75  |
| Table A.1.1 Projection line cases .....                                     | 99  |
| Table A.2.1 Fan beam projection cases .....                                 | 101 |

## LIST OF FIGURES

### FIGURES

|  |    |
|--|----|
| Fig. 1.1 X-ray penetration .....   | 2  |
| Fig. 2.1 Tomographic imaging model .....   | 12 |
| Fig. 2.2 Images reconstructed by FBP .....   | 16 |
| Fig. 2.3 Sinogram illustrations .....  | 17 |
| Fig. 2.4 Images reconstructed by ART ( $k = 1$ ).....                                      | 21 |
| Fig. 2.5 Images reconstructed by SART ( $k = 1$ ).....                                     | 22 |
| Fig. 2.6 Images reconstructed by iterative techniques ( $k = 1, 10$ ).....                 | 23 |
| Fig. 3.1 1-D sparse signal reconstruction.....   | 28 |
| Fig. 3.2 1-D compressible signal reconstruction.....                                       | 29 |
| Fig. 3.3 Sparse representations of the phantom image.....                                  | 30 |
| Fig. 3.4 Pilot of the magnitude sorted coefficients in Figs. 3.3(b)-(d).....               | 30 |
| Fig. 3.5 CS reconstruction of the phantom image.....                                       | 31 |
| Fig. 5.1 A $32 \times 32$ test image .....   | 46 |
| Fig. 5.2 Plot of PSNR versus radiation absorbed (SOCP, FBP, and SART) .....                | 47 |
| Fig. 5.3 Plot of reconstruction time versus number of rays .....                           | 48 |
| Fig. 5.4 Recoveries of the $32 \times 32$ test image .....                                 | 49 |
| Fig. 5.5 Recoveries of the phantom image (SOCP and FT).....                                | 50 |
| Fig. 5.6 PSNR and time records in iterations of SOCP ( $c = 600, n_{mw} = 50$ ).....       | 53 |
| Fig. 5.7 PSNR and time records in iterations of ASD-POCS ( $k_p = 200, n_{sd} = 20$ )..... | 53 |
| Fig. 5.8 PSNR and time records in iterations of ASD-FT ( $k_f = 200, n_{sd} = 20$ ) .....  | 54 |
| Fig. 5.9 PSNR and time records in iterations of DFP .....                                  | 54 |
| Fig. 5.10 Performance comparison of SOCP with other CS-based solutions .....               | 55 |
| Fig. 6.1 3-D illustration of $TV(x)$ , $RS(x)$ and $f(x)$ .....                            | 58 |
| Fig. 6.2 GMIs used in experimenting FTV .....  | 67 |
| Fig. 6.3 The Shepp-Logan image reconstructed in $EI$ .....                                 | 69 |
| Fig. 6.4 Reconstructed image profiles in $EI$ .....  | 70 |

|   |     |
|---|-----|
| Fig. 6.5 Function values as FTV iterates in $E1$ .....                      | 71  |
| Fig. 6.6 The cranial CT image reconstructed in $E2$ .....                   | 73  |
| Fig. 6.7 The Shepp-Logan image reconstructed in $E3$ .....                  | 76  |
| Fig. 6.8 Reconstructed image profiles in $E3$ .....                         | 77  |
| Fig. 6.9 Function values as FTV iterates in $E3$ .....                      | 77  |
| Fig. 6.10 The cranial CT image reconstructed in $E4$ (Part 1) .....         | 79  |
| Fig. 6.11 The cranial CT image reconstructed in $E4$ (Part 2) .....         | 80  |
| Fig. 6.12 PSNR and time records in iterations of FTV .....                  | 82  |
| Fig. 6.13 PSNR and time records in iterations of SOCP.....                  | 83  |
| Fig. 6.14 PSNR and time records in iterations of ASD-POCS .....             | 83  |
| Fig. 6.15 PSNR and time records in iterations of ASD-FT.....                | 84  |
| Fig. 6.16 Performance comparison of FTV with other CS-based solutions ..... | 84  |
| Fig. A.1.1 Ray equation, case 1.....  | 99  |
| Fig. A.1.2 Ray equation, case 2.....  | 100 |
| Fig. A.1.3 Ray equation, case 3.....  | 100 |
| Fig. A.1.4 Ray equation, case 4.....  | 101 |
| Fig. A.2.1 Fan geometry, case 1.....  | 102 |
| Fig. A.2.2 Fan geometry, case 2.....  | 102 |
| Fig. A.2.3 Fan geometry, case 3.....  | 103 |
| Fig. A.2.4 Fan geometry, case 4.....  | 103 |
| Fig. A.2.5 Fan geometry, case 5.....  | 104 |
| Fig. A.2.6 Fan geometry, case 6.....  | 104 |
| Fig. A.2.7 Fan geometry, case 7.....  | 105 |
| Fig. A.2.8 Fan geometry, case 8.....  | 105 |

# NOMENCLATURE

## ABBREVIATIONS

|       |   |
|-------|---|
| ART   | Algebraic Reconstruction Technique              |
| ASD   | Adaptive Steepest Descent                       |
| CG    | Conjugate Gradient                              |
| CS    | Compressed Sensing                              |
| CT    | Computed (Computerized) Tomography              |
| CTI   | Computerized Tomographic Imaging                |
| dB    | Decibel   |
| DCT   | Discrete Cosine Transform                       |
| DFP   | Davidon-Fletcher-Powell Method                  |
| DWT   | Discrete Wavelet Transform                      |
| FBP   | Filtered Back Projection                        |
| FT    | Fourier Transform                               |
| FTV   | Fast Total Variation Minimization Algorithm     |
| GMI   | Gradient Magnitude Image                        |
| mGy   | mili-Gray                                       |
| MRI   | Magnetic Resonance Imaging                      |
| mSv   | mili-Sievert                                    |
| POCS  | Projection onto Convex Sets                     |
| PSNR  | Peak Signal to Noise Ratio                      |
| SART  | Simultaneous Algebraic Reconstruction Technique |
| SMMLQ | Symmetric LQ Algorithm                          |
| SNR   | Signal to Noise Ratio                           |
| SOCP  | Second Order Cone Programming                   |
| TV    | Total Variation                                 |
| UP    | Unconstrained Problem                           |

## SYMBOLS

|                     |  |
|---------------------|--|
| $c$                 | Maximum number of CG or SMMLQ iterations in SOCP                         |
| $F(x)$              | Fourier operator acting on $x$   |
| $k_b$               | Maximum number of log-barrier iterations                                 |
| $k_c$               | Maximum number of CG iterations in FTV                                   |
| $k_f$               | Maximum number of main loop iterations of ASD-FT                         |
| $k_o$               | Maximum number of main loop iterations of CG-based algorithm             |
| $k_p$               | Maximum number of main loop iterations of ASD-POCS                       |
| $\mu_j$             | Attenuation coefficient at the $j^{\text{th}}$ image element             |
| $\mu(x,y)$          | Attenuation function of a two-dimensional object                         |
| $n_{nw}$            | Maximum number of Newton iterations allowed                              |
| $n_{sd}$            | Maximum number of steepest-descent iterations allowed                    |
| $p_i$               | Projection data corresponding to $i^{\text{th}}$ ray                     |
| $p_\theta(t)$       | Projection function  |
| $\ x\ _p$           | $l_p$ -norm of a vector $x$  |
| $\ x\ _{\text{TV}}$ | TV-norm of a vector $x$  |
| $W$                 | Data acquisition (weighting) matrix                                      |
| $w_i$               | $i^{\text{th}}$ row vector of $W$  |
| $w_{ij}$            | The element of $W$ at the $i^{\text{th}}$ row and $j^{\text{th}}$ column |

# CHAPTER 1

## INTRODUCTION

The story of X-ray imaging started with the discovery of X-rays by Röntgen in 1895. For his work, Röntgen received the first Nobel Prize in Physics in 1901. This discovery constitutes the historic starting point of medical imaging. The initial work ground for computerized tomography was laid by Radon in 1917 when he demonstrated that an object could be reconstructed from an infinite number of projections through that object [1]. In the 1960's, Cormack began to apply Radon's principles to medical applications. This led to the development of the first clinically useful computerized tomography (CT) scanner by Hounsfield in 1972 [2]. The 1979 Nobel Prize in Medicine was shared between these two pioneers of CT. Since its inception, CT scanners have improved in many perspectives including data acquisition and image reconstruction [3].

### 1.1 Data Acquisition

CT relies on the fact that X-rays passing through an object are absorbed or scattered and the resulting loss in intensity is computed. Consider an incremental thickness of the slab shown in Fig. 1(a). It is assumed that  $N_0$  monochromatic photons cross the left layer of this slab and that only  $N_0 - dN_0$  emerge from the other side. These  $N_0 - dN_0$  photons, unaffected by either absorption or scattering, propagate in their original direction of travel. If the photon energies are the same, the number of photons as a function of space is given by  $N_0(x) = N_0 e^{-\mu x}$  [4], where the attenuation coefficient,  $\mu$ , represents the constant photon loss rate on a per unit distance basis because of the photoelectric and Compton effects. When the width of the beam is sufficiently small, reasoning as in the one-dimensional case, the total number of photons entering and leaving an object,  $N_{in}$  and  $N_{out}$  (see Fig. 1(b)), respectively, are related by



$$N_{out} = N_{in} \cdot \exp\left(- \int_{ray\ AB} \mu(x,y) ds\right) \quad (1.1)$$

Using the equation of line  $AB$  shown in Fig. 1(b), the integrand  $\mu(x,y)ds$  can be replaced by  $\mu(x,y)\delta(x \cos \theta + y \sin \theta - t)dx dy$ . The natural logarithms of both sides in (1.1) results in the standard attenuation equation,

$$\ln \frac{N_{in}}{N_{out}} = \int_{ray\ AB} \mu(x,y)\delta(x \cos \theta + y \sin \theta - t)dx dy \quad (1.2)$$

The ray integral above gives the projection data  $p_\theta(t)$  as a function of angle  $\theta$  and distance  $t$ . Therefore, measurements like  $\ln(N_{in}/N_{out})$  taken for different rays at different angles can be used to generate projection data for reconstructing the function  $\mu(x,y)$ .

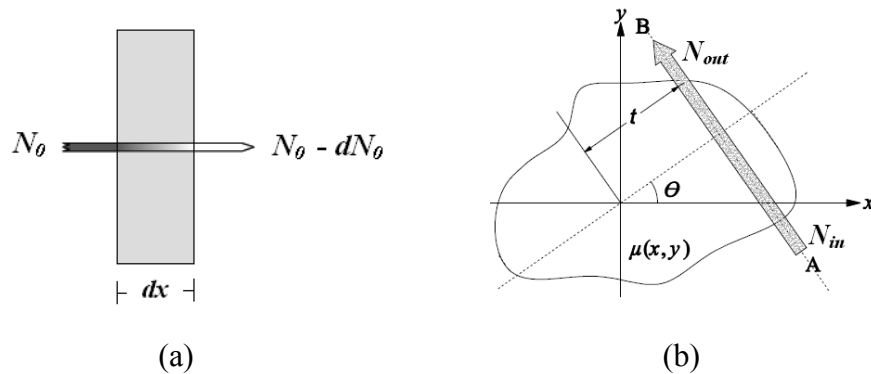


Fig. 1.1: X-ray penetration. (a)  $N_\theta$  monochromatic X-ray photons passing through an incremental thickness of the slab. (b)  $N_{in}$  monochromatic X-ray photons passing through an object represented by the attenuation distribution or density function,  $\mu(x,y)$ .

## 1.2 Image Reconstruction

The measurements obtained by a CT scanner result in a series of projection data. Image reconstruction algorithms exploit the projection data to estimate the attenuation density function,  $\mu(x,y)$ . The value of  $\mu(x,y)$  is also called the attenuation coefficient at  $(x,y)$ . The differences in attenuation coefficients at all locations

provide the contrast on the X-ray film. One of the most popular algorithms in use today is the *filtered back projection* (FBP). It was invented by Bracewell and Riddle [5], and later independently with additional insights by Ramachandran and Lakshminarayanan [6] who are also responsible for the convolution back-projection algorithm. This is the algorithm now used by almost all commercially available CT scanners [3].

The projection data corresponding to an X-ray keeps the attenuation faced by the X-ray on its trajectory. In back projection, this attenuation information is distributed back to the elements of the object through which the X-ray has passed. Each element takes the amount proportional to its interaction with the X-ray so as to recover its attenuation coefficient. The back projection operation is repeated for all projection data. The attenuation coefficient of a particular element will be built up from back projecting all X-rays' projection passing through this element. In continuous time, these elements are called *points* whereas in discrete time they are called *pixels*. In practice, it is assumed that the object under reconstruction is composed of discrete elements. The contribution of individual pixels to the projection data can be modeled in many ways [7]. The back projection alone results in a blurred reconstruction. Filtering must be applied to correct it and obtain a more accurate recovery. Filtering and back projection are both linear operations, so the order in which they are performed does not matter. However, filtering in one dimension is a much simpler task than in two dimensions. For this reason, the filtering is applied on projection data prior to back projection.

Alternative to filtered back projection, *algebraic reconstruction techniques* (ARTs) [8]-[12] can be used to iteratively solve the reconstruction problems arising from more complicated imaging models. Algebraic reconstruction techniques were used in early generation of CT scanners [13]. It was shown by Shepp and Logan [14] that the filtered back-projection method is much superior to other methods (especially the algebraic methods) in 1974 [3]. Today, iterative methods are to be in widespread clinical use, owing to improvements in computer power and development of efficient modeling techniques and fast reconstruction algorithms [7].

### 1.3 Cancer Risk in X-ray Imaging

The literature on diagnostic imaging and its effects is enormous [15]-[33]. It is hard to end with reliable risk estimations in both qualitative [15]-[19] and quantitative [20]-[33] endless discussions, but the concrete truth is X-rays can cause damage to cells in the body, which in turn can increase the risk of developing cancer. This increase in risk associated with each X-ray procedure is low but does slowly increase with the increasing number of X-ray tests and cumulative radiation doses absorbed.

The use of CT has increased rapidly in all developed countries since 1970s. It is estimated that about 3 million CT scans per year were performed in the UK in 2005-2006, compared with 0.25 million in 1980 [23]. The corresponding figures for the US are 69 million scans in 2007, compared with approximately 2 million scans in 1980. The dramatic increase in the number of CT examinations concerns doctors about potential risks [25]-[27]. They notify three-quarters of the collective dose from radiology is the result of high-dose procedures, in particular CT, interventional radiology and barium enemas. For these procedures, the organ doses involved are sufficiently large that there is direct statistical evidence of small increased cancer risks [23]. Even a small individual radiation risk, when multiplied by a huge number of population, adds up to a significant long-term public health problem that will not become evident for many years.

The effective doses applied in computed tomography in particular is much higher than that in other diagnostic examinations [21]. For example, typical doses to the lung from a conventional chest X-ray range from about 0.01 mGy (mGy: milli-Gray, the unit used to give absorbed dose) to 0.15 mGy, whereas a typical dose to an organ examined with CT is around 10 mGy to 20 mGy, and can be as high as 80 mGy for 64-slice CT coronary angiography [22]. Brenner and Elliston [25] state that the effective dose, which is a weighted average of doses to all organs in a single full-body CT examination, is about 12 mSv (mSv: milli-Sievert, the unit used to give effective dose). If, for example, 10 such examinations were undertaken in a lifetime, the effective dose would be about 120 mSv. To put these doses in perspective,

individuals in survivors of the atomic bomb in the dose category from 5 to 100 mSv (mean, 29 mSv) show a statistically significant increase in solid cancer risk.

There is also additional risk from follow up CT examinations. Because of the nature of the full body screening, the high false-positive rate necessitates further evaluations of more than one third of those screened, whereas only a small fraction (a few percent) of the overall reveals cancer evidence [23]. The patients undergoing CT of neck, chest, abdomen, or pelvis in emergency departments have high cumulative rates of multiple or repeated imaging. Collectively, this patient subgroup may have a heightened risk of developing cancer from cumulative CT radiation exposure. Their increased risk of carcinogenesis is reflected in estimated lifetime attributable risks ranging from 1 in 625 to 1 in 17 [32].

#### **1.4 Risk Reduction**

A consensus about the efficacy of the recent screening with CT applications has not been reached [19], [23]. The patient here is left to trade a small statistical risk of cancer in the distant future, or maybe in the near future for the case of a baby in the womb, for the immediate preservation of his life. Irrespective of the absolute levels of CT-associated risk, it is clearly desirable to reduce CT doses and/or usages. The latter is not an easy task. Physicians are often subject to significant pressures from the medical system, the medico-legal system and from the public to prescribe CT. In most scenarios, CT is the appropriate choice, but there are undoubtedly significant proportion of potential situations where CT is not medically justifiable or where equally effective alternatives exist [23]. The trend towards a somewhat less selective use of diagnostic CT due to underestimated radiation dose from a CT scan or unbelief of increased cancer risk by a great majority of the radiologist and/or emergency room physicians is unfortunately in considerable part responsible for the rapid increases in CT use.

Minimizing the radiation dose usually includes fine adjustment of, but not limited to, the following CT settings while scanning patients [20], [22], [34]: 1) Tube voltage, 2) Tube current and exposure time, 3) Pitch. Reduction of the tube voltage is used for decreasing the average photon energy and thus the patient

exposure [20]. Being a measure of the amount of radiation, the product of X-ray tube current and exposure time is usually reduced for pediatric patients, because they are smaller in size and therefore easier to penetrate [22]. The pitch is the table movement per tube rotation/slice collimation. While keeping the other parameters constant, increasing the pitch spreads the radiation energy over a larger patient volume, thereby decreasing the patient dose [34].

In general, exposure control is based on the notion that lower CT image noise will typically be achieved at the cost of higher doses, so image noise level should be no better than sufficient for the diagnostic test. Given a desired noise level and the geometry of the patient, either manually or automated exposure control techniques can be used to generate a CT setting that will minimize the patient dose [23]. However, even with the same CT settings, different scanners will produce different doses and therefore different risks. In particular, the calculated organ dose to the lung is 15.5 mGy for the Siemens scanner, 16.1 mGy for the Philips scanner, and 21.2 mGy for the GE Medical Systems scanner [25].

## **1.5 Compressed Sensing**

Image compression algorithms convert high-resolution images into a relatively short bit streams (while keeping the essential features unchanged), in effect turning a large digital data set into a substantially smaller one. There is an extensive body of literature on image compression; the principle is that the image is transformed into an appropriate basis and then only the significant expansion coefficients are coded. The main problem is to find a good transform, which has been studied extensively from both theoretical [35] and practical [36] standpoints. The most remarkable product of this research is the wavelet transform [37]-[38]; switching from sinusoid-based representations to wavelets made a significant advance in image compression standards; namely from the classical JPEG [39] to modern JPEG2000 [40]. These standards are put into practice by acquiring the full signal at the beginning. Following the computation of transform coefficients, only a small fraction of the coefficients is encoded and the rest is discarded. While using this modality, one can fairly ask the question: Is there a way to avoid the large data set to begin with if the

majority of the collected data will be discarded at the end? Is there a way of building the data compression directly into the acquisition? The answer is yes exploiting the recently emerging compressed sensing (CS) theory [41].

CS, also known as compressive sampling or compressive sensing is a technique for finding sparse solutions to underdetermined linear systems. An underdetermined system of linear equations has more unknowns than equations and generally has an infinite number of solutions. However, if there is a unique sparse solution to the underdetermined system, then the recovery of that solution is allowed in the CS framework. It typically starts with taking a weighted linear combination of samples also called compressive measurements in a basis different from the basis in which the signal is known to be sparse. The results [41]-[42] found by Donoho, Candes, Romberg and Tao showed that the number of these compressive measurements can be small and still contain nearly all the useful information. Therefore, the task of converting the image back into the intended domain involves solving an underdetermined matrix equation since the number of compressive measurements taken is smaller than the number of pixels in the full image. Adding the constraint that the initial signal is sparse enables one to solve this underdetermined system of linear equations.

The field of compressive sensing is related to other topics in signal processing and computational mathematics, such as to error correction, inverse problems, compressive DSP, data compression, data acquisition [43].

## **1.6 Compressed Sensing Based CT Imaging**

Different ways of decreasing the radiation dose [44]-[45] basically aim to use the most dose-efficient technique to achieve the target image quality for each diagnostic task. The dose efficiency in CT can be improved by optimizing dose performance of the CT system, using either manual or automated exposure control techniques, and also our interest in this thesis, improving data processing and image reconstruction. In CT imaging system, numerous X-ray beams and detectors rotate concurrently around a body, and the amount of radiation absorbed throughout the body is computed. Using these large data sets, the traditional FBP based image

reconstruction algorithms provide high contrast images at the expense of so called high radiation absorption. On the other hand, FBP is inefficient with insufficient coverage in the scanning configuration or under-sampling. The recent advances in image reconstruction techniques [42], [46]-[47] have shown that accurate image reconstruction from incomplete data sets is possible using sparseness prior based iterative methods. Based on the compressed sensing theory [47], [41], these methods employ incoherent measurements from an object of interest and, as a solution, seek the sparsest object or its most compressible representation in a sparsifying domain (e.g., Fourier, wavelet, etc.). The impressive results have immediately inspired applications in Magnetic Resonance Imaging (MRI) [48]-[51] and then in CT Imaging (CTI) [52]-[63]. The studies have shown that incorporating the sparsity feature of CT images into the reconstruction problem results in more accurate recoveries from few projection data.

## **1.7 Contributions**

Today, commercial CT scanners employ traditional FBP based algorithms for image reconstruction [64]. Many considerations including the communication problems between CT engineers and theoreticians, and economic conflicts for CT manufacturers can be stated as reasoning. In addition, that FBP based algorithms can be implemented to achieve high reconstruction speeds make them expedient as compared to iterative methods. In this thesis, we propose two CS based image reconstruction algorithms that allow reducing radiation dose without sacrificing the CT image quality even in the case of noisy measurements. The first one, log-barrier algorithm, recasts the optimization problem that aims to minimize the estimated image's total variation (TV) as second order cone programming (SOCP) and solves it via a logarithmic barrier method. The second one, fast TV minimization algorithm, (FTV), reformulates the TV minimization problem as an unconstrained problem to solve it rapidly using the conjugate gradient (CG) method. Using few measurements, the proposed schemes provide better reconstructed images as compared to the solutions of the traditional FBP based algorithms or ARTs.

Although complexity order of the log-barrier method is higher than the state-of-the-art algorithms [57], [59], it is capable of converging faster to a better solution especially for small scale problems. It takes advantage of Newton's method to end up with an accurate solution rapidly. When the problem size gets large, on the other hand, it suffers from huge matrix vector multiplications. To justify our claims, we performed numerical experiments involving performance comparisons of the log-barrier algorithm with other CS based and traditional algorithms.

FTV offers faster reconstruction of images than the log-barrier algorithm. Keeping CG method [65] at its core, it has higher reconstruction speed than the recent algorithms [57], [59], [62] that have attracted broad interest in, but not limited to [52]-[62]. To justify our claims, we categorized these algorithms into three classes: Projection onto Convex Sets (POCS), Fourier Transform, and Second Order Cone Programming. They were investigated in detail to clarify their (dis)advantages. Our studies include those demonstrating both the performance of FTV on non-sparse images and the relations between the quality of reconstructed images and the amount of radiation absorbed; issues that hardly take part in literature in the field as far as we know.

We also brought intuitive examples of CS and discussions on CS integration into the CT system to better give the concept of CS based CTI in our study.

## **1.8 Organization of the Thesis**

The thesis is organized as follows: In Chapter 2, the traditional FBP algorithm and ARTs are reviewed together with the data acquisition model used in these reconstruction methods. Besides, constructions of data acquisition matrices that are used in experiments throughout the thesis, and example images reconstructed by FBP and ARTs are given. In Chapter 3, CS is reviewed from both theoretical and practical standpoints. In Chapter 4, we discuss the concept of CS based CT imaging, leading to the reconstruction problem reformulated in the CS framework. Furthermore, the state-of-the-art algorithms solving the CS problem are considered. In Chapter 5, SOCP and its solution via the log-barrier algorithm are presented. Its performance against FBP, SART (an effective iterative method), and the state-of-



the-art algorithms are tested in three numerical experiments. In Chapter 6, we present FTV in detail and test its performance against FBP and the state-of-the-art algorithms in four numerical experiments. In the last chapter, the concluding remarks are given.

## CHAPTER 2

### COMPUTERIZED TOMOGRAPHY IMAGING

#### 2.1 Linear Imaging Model

A CT scanner measures the intensities of X-ray beams that pass through the body and generates the projection data  $p_\theta(t)$ . The space parameters  $(t, \theta)$  define the projection line  $t = x \cdot \cos\theta + y \cdot \sin\theta$  along which an X-ray beam travels as shown in Fig. 2.1(a). Assuming the beam width is infinitesimally narrow, the projection data is expressed by line integral of the body cross-sectional function  $\mu(x,y)$  as

$$p_\theta(t) = \int_{-\infty}^{\infty} \int_{-\infty}^{\infty} \mu(x,y) \delta(x \cos \theta + y \sin \theta - t) dx dy \quad (2.1)$$

In a modern CT scanner, an X-ray fan beam and detector sweep around the patient and provide thousands of projections at different angles. The objective is to estimate  $\mu(x,y)$  from all projections. The differences in values of  $\mu(x,y)$  at different  $(x, y)$  coordinates provide the contrast on CT images.

For computing purposes, the reconstructed images cannot be represented by a continuous-domain function; instead a sampled version of the image described in a discrete domain is estimated. That is, a square grid is superimposed on the image  $\mu(x,y)$  as shown in Fig. 2.1(b). It is assumed that the size of the grid cells is small and the function  $\mu(x,y)$  is approximately constant within a cell. Let  $\mu_j$  be this constant value in the  $j^{\text{th}}$  cell and  $N$  be the total number of cells. Under the assumptions above, the line integral in (2.1) is expressed by

$$p_i = \sum_{j=1}^N w_{ij} \mu_j \quad (2.2)$$

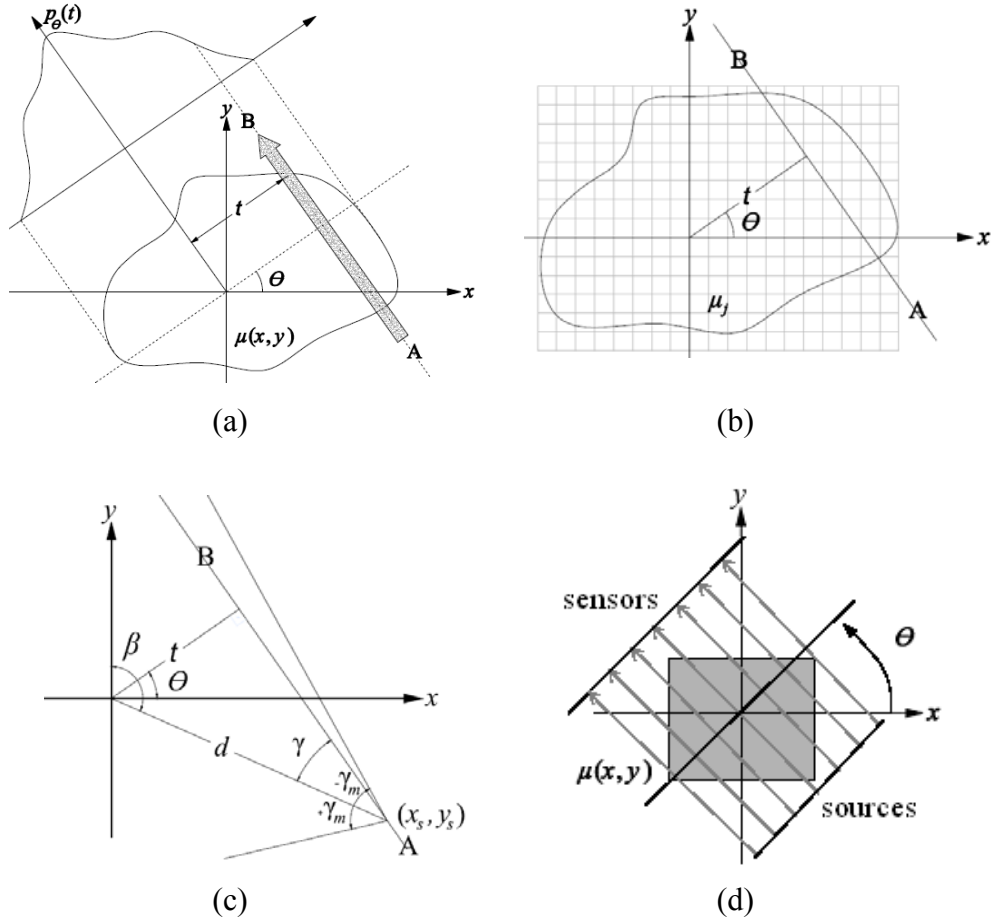


Fig. 2.1: Tomographic imaging model. (a) An object,  $\mu(x, y)$  and its projection,  $p_\theta(t)$  along the projection line AB. The X-ray beam emerging from A to B is assumed to have infinitesimally narrow width, meaning that the beam has a single X-ray. CT scanner measures the amount of attenuation,  $p_\theta(t)$ , of the X-ray traveling through the object. (b) Square grid is superimposed over the unknown body. Body values are assumed to be constant within each cell of the grid. (c) Fan beam projection geometry. The fan opening at source location  $(x_s, y_s)$  is defined by  $[\gamma_{\min} = -\gamma_m, \gamma_{\max} = +\gamma_m]$ . Each ray in the fan is identified by its angle  $\gamma$  from the central ray.  $d$  is the distance from the source to the origin over the central ray.  $\beta$  is the angle of central ray from  $y$ -axis. (d) Illustration of parallel beam projection. X-rays radiated from multiple sources are aligned in parallel. Typically, the projection angle  $\theta$  ranges in the interval  $[\theta_{\min} = 0, \theta_{\max} = 2\pi]$ .

where  $p_i$  denotes the ray sum value for the  $i^{\text{th}}$  ray and  $w_{ij}$  is the weighting factor that represents the contribution of the  $j^{\text{th}}$  cell to the  $i^{\text{th}}$  ray-sum. Assuming there are  $m$  number of X-ray projections, the set of linear equations, corresponding to  $i=1,2,3,\dots,m$ , is written in matrix form:

$$WM = P \quad (2.3)$$

or explicitly,

$$\underbrace{\begin{bmatrix} w_{11} & w_{12} & w_{13} & \dots & w_{1N} \\ w_{21} & w_{22} & w_{23} & \dots & w_{2N} \\ \vdots & \vdots & \vdots & \vdots & \vdots \\ w_{m1} & w_{m2} & w_{m3} & \dots & w_{mN} \end{bmatrix}}_W \underbrace{\begin{bmatrix} \mu_1 \\ \mu_2 \\ \vdots \\ \mu_N \end{bmatrix}}_M = \underbrace{\begin{bmatrix} p_1 \\ p_2 \\ \vdots \\ p_m \end{bmatrix}}_P$$

There are several different approaches for projecting a cell (see Appendices in [17]). Being a computationally efficient one, the line length approach defines  $w_{ij}$  as the length of the ray in the region bounded by the cell. Once  $w_{ij}$ 's are computed for a fixed scanning configuration, the matrix  $W$  is stored in memory, ensuring a time saving for the ongoing image recovery practices. Typically, for the fan projection geometry shown in Fig. 2.1(c) (see Appendix A for the detailed geometric interpretation),  $W$  can be constructed in the following manner:

---

**Method I:** Constructing the fan projection matrix.

---

```

1   initialize  $d, \beta_{\min}, \beta_{\max}, \gamma_{\min}, \gamma_{\max}, \mathbf{u}, \mathbf{v}, W$ 
2   repeat for index  $u \leftarrow 1$  to  $u$ 
3      $\beta \leftarrow \beta_u \in [\beta_{\min}, \beta_{\max}]$ 
4      $x_s \leftarrow d \sin \beta, y_s \leftarrow d \cos \beta$ 
5     repeat for index  $v \leftarrow 1$  to  $v$ 
6        $\gamma \leftarrow \gamma_v \in [\gamma_{\min}, \gamma_{\max}]$ 
7        $\theta' \leftarrow -(\beta - \gamma)$ 
8        $\theta \leftarrow \begin{cases} \theta' & \text{if } 0 \leq \theta' < 180 \\ \theta' - 180 & \text{if } 180 \leq \theta' < 360 \\ \theta' + 180 & \text{if } -180 \leq \theta' < 0 \\ \theta' + 360 & \text{if } -360 \leq \theta' < -180 \end{cases}$ 
9        $t \leftarrow x_s \cos \theta + y_s \sin \theta$ 
10       $W \leftarrow$  compute  $w_{ij}$ 's for this ray
11    end
12  end

```

---

In Method I,  $u$  and  $v$  are the number of source locations and rays in a fan beam, respectively. The outer loop localizes the point source whose coordinate  $(x_s, y_s)$  is computed at line 4. The inner loop serves the purpose of computing weighting

factors for each ray in the fan beam emerging from the source location  $(x_s, y_s)$ . The ray projection angle  $\theta$  and its distance to the origin  $t$  are computed at lines 8 and 9, respectively. Let the  $(t, \theta)$  pair identify the  $i^{\text{th}}$  projection line. All weighting factors along the  $i^{\text{th}}$  ray are computed at line 10. Ordinarily,  $W$  is a large matrix. Consider the scanning of a discrete image of size  $256 \times 256$ . If fan beams are emitted from 180 distinct locations with 1 degree angle of separation,  $m \approx 46\text{K}$  measurements are collected by means of 256 detectors. For such an experiment, it is necessary to keep approximately 2.8 Gbytes of data ( $w_{ij}$ 's) forming a  $W \in \mathbf{R}^{46,000 \times 65,536}$  to recover the image. Keeping such huge data in memory is difficult and techniques should be developed to avoid the memory limitations and lessen its computation time for different data acquisition configurations.

Besides the fan beam projection, other projection methods like parallel or cone beam can be used to acquire data. Typically, for the parallel projection geometry illustrated in Fig. 2.1(d),  $W$  can be constructed in the following manner:

---

**Method II:** Constructing the parallel projection matrix.

---

```

1   initialize  $\theta_{\min}, \theta_{\max}, t_{\min}, t_{\max}, u, v, W$ 
2   repeat for index  $u \leftarrow 1$  to  $u$ 
3      $\theta \leftarrow \theta_u \in [\theta_{\min}, \theta_{\max}]$ 
4     repeat for index  $v \leftarrow 1$  to  $v$ 
5        $t \leftarrow t_v \in [t_{\min}, t_{\max}]$ 
6        $W \leftarrow$  compute  $w_{ij}$ 's for this ray
7     end
8   end

```

---

Method II has the same spirit with Method I such that  $u$  and  $v$  in both are used for indexing view angles and X-rays' distance to the origin, respectively. Given a pair of  $(\theta, t)$  parameters for an X-ray, the same function is used at lines 10 and 6 in Methods I and II, respectively, to compute the elements of  $W$ . Since the projection angle is fixed for all rays in a given view (parallel beam), constructing the parallel beam projection matrix is easier than implementing Method I. In this thesis, both parallel and fan beam projection data are used while experimenting the proposed schemes in Chapters 5 and 6, respectively. The fan beam projection is also considered within traditional and iterative image reconstruction algorithms discussed in the following subsections.

## 2.2 Traditional Image Reconstruction

The FBP is a commonly used technique in CTI today [64].  $\mu_j$ 's are estimated by the weighted back projection of filtered  $p_i$ 's:

$$\sum_i w_{ij} p_i' = \hat{\mu}_j, \quad i = 1, 2, 3, \dots, m \quad (2.4)$$

where  $p_i'$  and  $\hat{\mu}_j$  denote the filtered value of  $p_i$  and the estimation for  $\mu_j$ , respectively. Let  $P'$  and  $\hat{M}$  be vectors of  $p_i'$ 's and  $\hat{\mu}_j$ 's, respectively. The equation set in (2.4) can be expressed in the closed form as

$$W^T P' = \hat{M} \quad (2.5)$$

The  $p_i'$ 's belonging to the set of a view (fan beam) projection data are high pass filtered by a discrete time filter  $h$  [4] of the form:

$$h_n = \begin{cases} \frac{1}{8(\Delta_\gamma)^2} & n = 0 \\ 0 & n \neq 0, n \text{ is even} \\ \frac{-0.5}{\pi^2 \sin^2(\Delta_\gamma)} & n \text{ is odd} \end{cases} \quad (2.6)$$

where  $\Delta_\gamma$  is the angle of ray separation in a fan beam. The high pass filtering or a certain amount of smoothing combined with (2.6) gets rid of very high amplification of low frequencies inherent in recoveries without filtering. The matrix-vector multiplication provides a very fast reconstruction in (2.5). Despite its speed of implementation, FBP requires a large  $m$  at the expense of increased radiation absorption so as to provide a high accuracy in reconstructed images. Consider the real image in Fig. 2.2(a) and some of its recoveries in Fig. 2.2(b)-(f). In all cases, the projection data are collected over a half angular range of  $\pi$  by equiangular set of detectors. The best recovery shown in Fig. 2.2(f) is obtained from a large data set:  $\sim 1.4$  times the number of samples in the original image. When  $m$  is reduced a few orders, the reconstructed images have high degradations as perceived in Fig. 2.2(b)-(e).

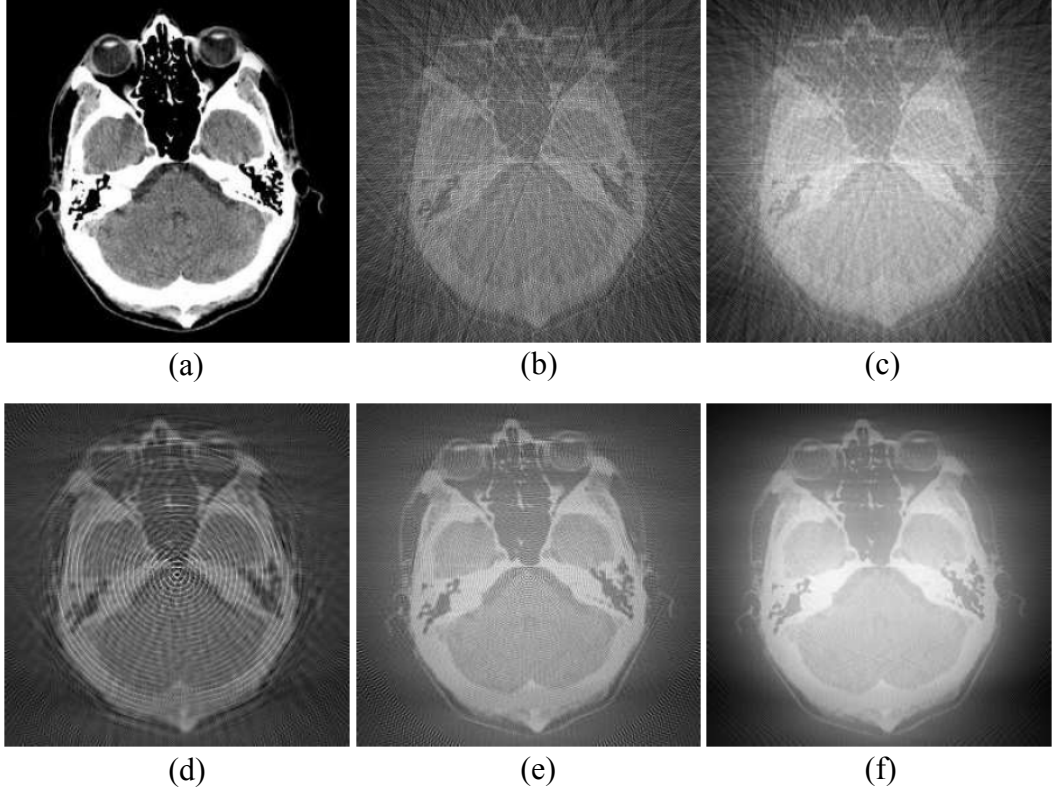


Fig. 2.2: Images reconstructed by FBP. (a)  $256 \times 256$  original image. The following images are recovered using FBP with (b)  $m = 7680$  measurements ( $30$  views  $\times$   $256$  rays/view), (c)  $m = 15360$  measurements ( $30$  views  $\times$   $512$  rays/view), (d)  $m = 23040$  measurements ( $180$  views  $\times$   $128$  rays/view), (e)  $m = 46080$  measurements ( $180$  views  $\times$   $256$  rays/view), (f)  $m = 92160$  measurements ( $180$  views  $\times$   $512$  rays/view). The system settings in all recoveries are  $d = 1.5 \times 256 \times \sqrt{2}$ ,  $\beta_{\min} = -\pi/2$ ,  $\beta_{\max} = \pi/2$ ,  $\gamma_{\min} = -\pi/7$ ,  $\gamma_{\max} = \pi/7$ .

The amount of radiation absorption by a body is related with the energy difference of photons that enter and leave the body. The contribution of a single X-ray projection,  $e_{X\text{-ray}}$ , to this amount is given by

$$e_{X\text{-ray}} \propto 1 - \exp[-p_{\theta}(t)] \quad (2.7)$$

which is normalized with respect to the number of incidence photons [47]. The overall radiation absorption is reduced by elimination of a ray ( $p_{\theta}(t) = 0$ ), which necessitates decreasing  $m$  in a CTI system. The rays' elimination is depicted on the sinograms in Fig. 2.3(a)-(b). The horizontal and vertical axes represent the detector

bin and projection angle  $\theta$ , respectively. The fan beam scanning configuration in Fig. 2.3(b) leads to 91.6% missing dark portions of the data and a 91.6% reduction in the radiation absorption compared to the best recovery configuration in Fig. 2.3(a). The relative absorption amounts for all configurations in Fig. 2.2 as well as the 30-fan  $\times$  128-ray are summarized in Table 2.1.

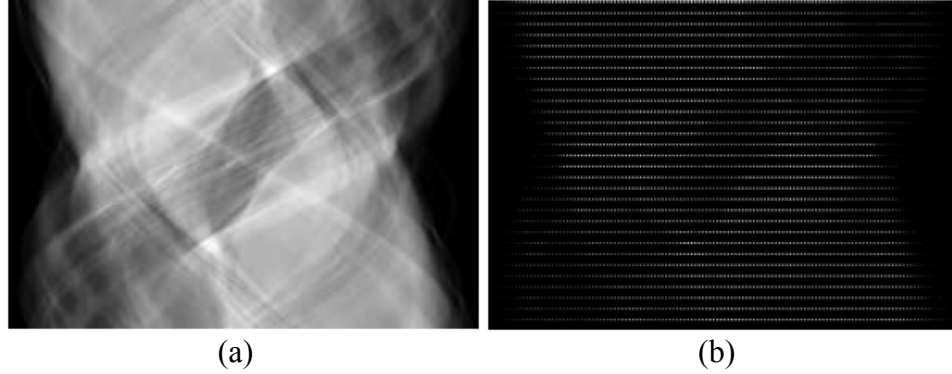


Fig. 2.3: Sinogram illustrations. (a) Sinogram for 180 views  $\times$  512 rays/view configuration. It is used for the recovery in Fig. 2.2(f). (b) Sinogram for 30 views  $\times$  256 rays/view configuration. It is used for the recovery in Fig. 2.2(b).

Table 2.1: Relative amounts of radiation absorbed.

|         | 128-ray | 256-ray | 512-ray |
|---------|---------|---------|---------|
| 30-fan  | 0.5     | 1       | 2       |
| 180-fan | 3       | 6       | 12      |

Although the total number of rays used in each experiment changes linearly, the linear relationship among the values in Table 2.1 is a coincidence. In fact, the attenuation characteristics of the tissue that X-ray passes through and the physical characteristics of X-rays determine the output of (2.7). Regarding the X-ray absorption reduction, the significance of a ray cancellation is evident in any circumstances. When quality of the reconstructed images is considered, a more *efficient* algorithm than FBP is needed. The word *efficient* means it is capable of reconstructing the image fast and accurately by using less number of projections.



A good efficiency is achieved by exploiting CS, the theory we benefited from in this study.

## 2.3 Algebraic Reconstruction Techniques

The reconstruction algorithms in the class of algebraic reconstruction techniques are iterative, i.e., they refine the estimated image progressively in a repetitive calculation. Contrary to FBP based algorithms that necessitate a large number of projections uniformly distributed over an angular range of  $\pi$  or  $2\pi$ , the iterative methods have unique advantages especially in cases of incomplete, random data sets. Besides, they are able to solve more complicated problems than problem (2.3) as a result of the improved imaging models that allow a rich description of the noise and attenuation mechanisms. “The principle trade-off between iterative techniques and FBP is one of accuracy versus efficiency. Iterative algorithms require repeated calculations of projection and back projection operations. Thus, they can require substantially greater computation time than FBP. Accurate modeling of physical effects in iterative algorithms can improve accuracy, but this added refinement can further compound the processing time.” “There is not yet a consensus that iterative reconstructions are always superior to FBP images or, at least, that the benefits of iterative reconstructions always justify the increased computational costs; therefore, the two approaches will continue to coexist for some time.” [7]. The iterative methods that are used in this thesis are the algebraic reconstruction technique (ART) and the simultaneous algebraic reconstruction technique (SART). They are detailed in the following subsections.

### 2.3.1 ART

ART updates the estimated image,  $\hat{M}^{(k)}$  at iteration step  $k$ , according to the following formula:

$$\hat{M}^{(k+1)} = \hat{M}^{(k)} + \lambda_{art}^{(k)} \frac{p_i - \langle w_i, \hat{M}^{(k)} \rangle}{\langle w_i, w_i \rangle} \cdot w_i, \quad i = 1, 2, \dots, m \quad (2.8)$$

where  $w_i$  is the  $i^{\text{th}}$  row vector (the vector along the direction of  $i^{\text{th}}$  ray) of matrix  $W$  and  $\lambda_{art}$  is a relaxation parameter. It can be inferred from the reformulation of (2.8)

$$\hat{M}^{(k+1)} = \hat{M}^{(k)} + \lambda_{art}^{(k)} \frac{p_i - \langle w_i, \hat{M}^{(k)} \rangle}{\|w_i\|_2} \cdot \frac{w_i}{\|w_i\|_2}, \quad i = 1, 2, \dots, m \quad (2.9)$$

that the error term  $p_i - \langle w_i, \hat{M}^{(k)} \rangle$  corresponding to the  $i^{\text{th}}$  projection data of the current image estimate,  $\hat{M}^{(k)}$ , is first normalized with respect to  $w_i$  and then back projected along the unit vector,  $w_i / \|w_i\|_2$ . Notice that the error in projection data is simply expressed by the difference between the observation  $p_i$  and the estimation  $\langle w_i, \hat{M}^{(k)} \rangle$ . At the outer iteration step  $k$ ,  $\hat{M}^{(k+1)}$  is obtained after back projecting the error terms for all  $i$ . The order of rays involved in successive processing of the error terms may affect the convergence speed and therefore the maximum number of iterations required. For example, when the rays are orthogonal, the solution is reached in one step ( $k=1$ ) no matter what the initial guess is. On the other hand, when the rays are more likely to be parallel, more and more iterations are needed to reach a solution [66]. The initial estimate  $\hat{M}^{(0)}$  is usually set to uniform image of zero attenuation (see § 4 in [67]).

### 2.3.2 SART

SART updates the  $j^{\text{th}}$  image element,  $\hat{\mu}_j^{(k)}$  at iteration step  $k$ , according to the following formula:

$$\hat{\mu}_j^{(k+1)} = \hat{\mu}_j^{(k)} + \lambda_{art}^{(k)} \frac{\sum_{p_i \in \varphi_\ell} \frac{p_i - \langle w_i, \hat{\mu}^{(k)} \rangle}{\|w_i\|_0} \cdot w_{ij}}{\sum_{p_i \in \varphi_\ell} w_{ij}}, \quad \ell = 1, 2, \dots, L, \quad i = 1, 2, \dots, \frac{m}{L} \quad (2.10)$$

where  $w_i$  and  $\lambda_{art}$  are as in ART,  $L$  is the number of views, and  $\varphi_\ell$  is the set of rays in the  $\ell^{\text{th}}$  view. The  $l_0$ -norm denoted by  $\|\cdot\|_0$  is the sum of terms in  $w_i$ , i.e., the length of the  $i^{\text{th}}$  ray inside the object. In contrast to ART where the output image is updated using  $p_i$ 's one by one, the average contribution of the rays in a view projection is computed, and then the output image is corrected in SART [67]. The back projection of the error terms corresponding to rays in the same view are given by the term

$$\sum_{p_i \in \varphi_i} \frac{p_i - \langle w_i, \hat{\mu}^{(k)} \rangle}{\|w_i\|_0} \cdot w_{ij}$$

in the numerator of (2.10). If angle of ray separations is large, few rays penetrate the  $j^{\text{th}}$  image element, i.e., the great majority of  $w_{ij}$ 's become zero. As a result, few error terms contribute to the summation for the  $j^{\text{th}}$  image element. The idea behind SART is to reduce the background noise by averaging these contributions before correcting the output  $\hat{\mu}_j^{(k)}$ . An iteration of SART is completed when the rays in all views are processed. SART usually yields reconstructions of better quality and numerical accuracy than ART images [4]. The convergence speed is affected by view separation angles as analogous to the angular difference of rays in ART.

### 2.3.3 Numerical Illustrations

The real image shown in Fig. 2.2(a) is recovered from different number of measurements used in the FBP experiment. The images reconstructed by ART and SART as a result of a single iteration are shown in Fig. 2.4 and Fig. 2.5, respectively. In both cases, the initial estimates started from the zero image. The relaxation parameters were updated according to  $\lambda^{(k+1)} = r \times \lambda^{(k)}$  where  $r = 0.95$  and  $\lambda^{(0)} = 0.9$ . Although it is not easy to realize the visual improvements on the quality of reconstructed images by SART, they have slightly higher PSNRs than those reconstructed by ART. The slight difference is due to large angle of ray separations. The X-ray point source which is located at  $d = 1.5 \times 256 \times \sqrt{2}$  in relative to pixel width away from the object center emits X-rays separated by  $\gamma = 2 \times (\pi/7) / (m/L - 1)$  radians. Assuming the object has elements of unity length, two successive rays crosses the same image element closest to the point source only when  $\tan \gamma < 1/(d-128)$ , meaning that the number of rays used in a view,  $m/L$ , should be greater than or equal to 374. In fact, it is the least amount and usually many more rays than that are preferred in practice. Therefore, the background noise reduction characteristic of SART can be realized for recoveries in the last column of Fig. 2.5 when compared to the corresponding images in Fig. 2.4.

When the number of iterations is increased tenfold, better recoveries are obtained as shown in Fig. 2.6. In this particular case, the PSNR improvement is

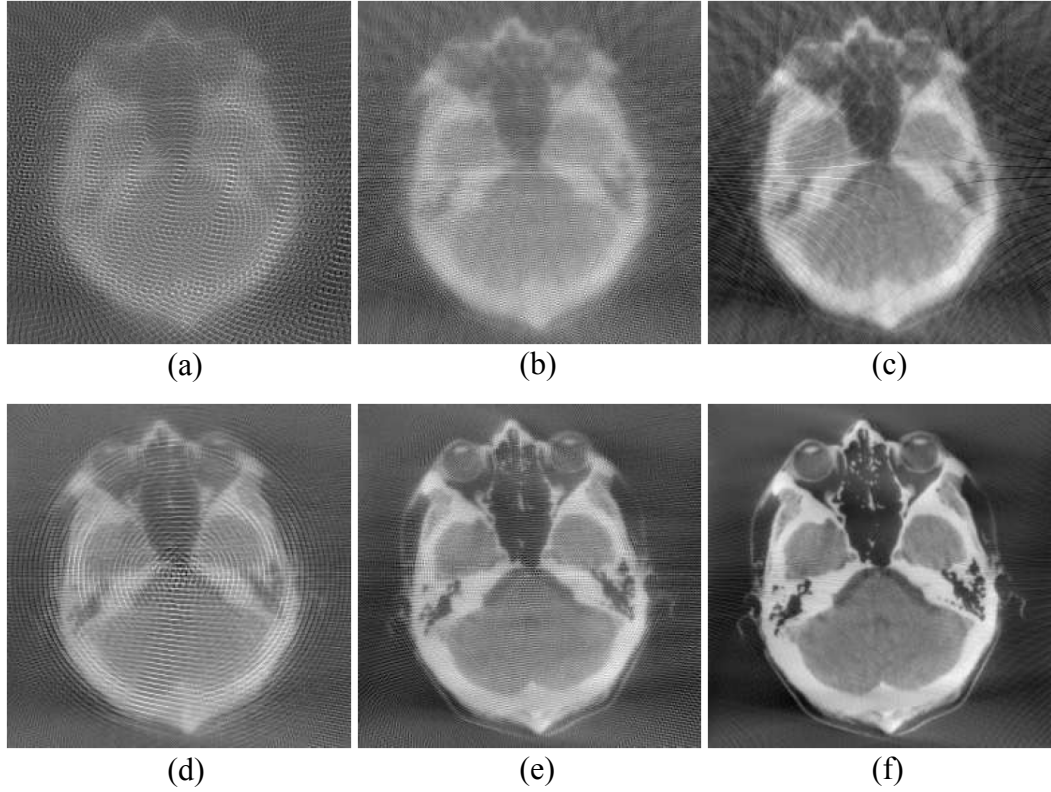


Fig. 2.4: Images reconstructed by ART ( $k = 1$ ). The original image is shown in Fig. 2.2(a). The following images are recovered from (a)  $m = 3840$  measurements ( $30 \text{ views} \times 128 \text{ rays/view}$ ), (b)  $m = 7680$  measurements ( $30 \text{ views} \times 256 \text{ rays/view}$ ), (c)  $m = 15360$  measurements ( $30 \text{ views} \times 512 \text{ rays/view}$ ), (d)  $m = 23040$  measurements ( $180 \text{ views} \times 128 \text{ rays/view}$ ), (e)  $m = 46080$  measurements ( $180 \text{ views} \times 256 \text{ rays/view}$ ), (f)  $m = 92160$  measurements ( $180 \text{ views} \times 512 \text{ rays/view}$ ). The system settings in all recoveries are  $d = 1.5 \times 256 \times \sqrt{2}$ ,  $\beta_{\min} = -\pi/2$ ,  $\beta_{\max} = \pi/2$ ,  $\gamma_{\min} = -\pi/7$ ,  $\gamma_{\max} = \pi/7$ .

approximately 5 dB in both ART and SART reconstructions. Further iterations lead to gradual improvements at the expense of linearly increasing reconstruction time.

Our final remark is about the recoveries via FBP and iterative techniques: The FBP recoveries in Fig. 2.2 have lower contrast resolution than those in Fig. 2.4 and Fig. 2.5. On the other hand, the spatial resolution provided by FBP is acceptable, and when the reconstruction speeds are considered, FBP is more attractive than the iterative techniques. While the reconstruction time required by ART or SART, in

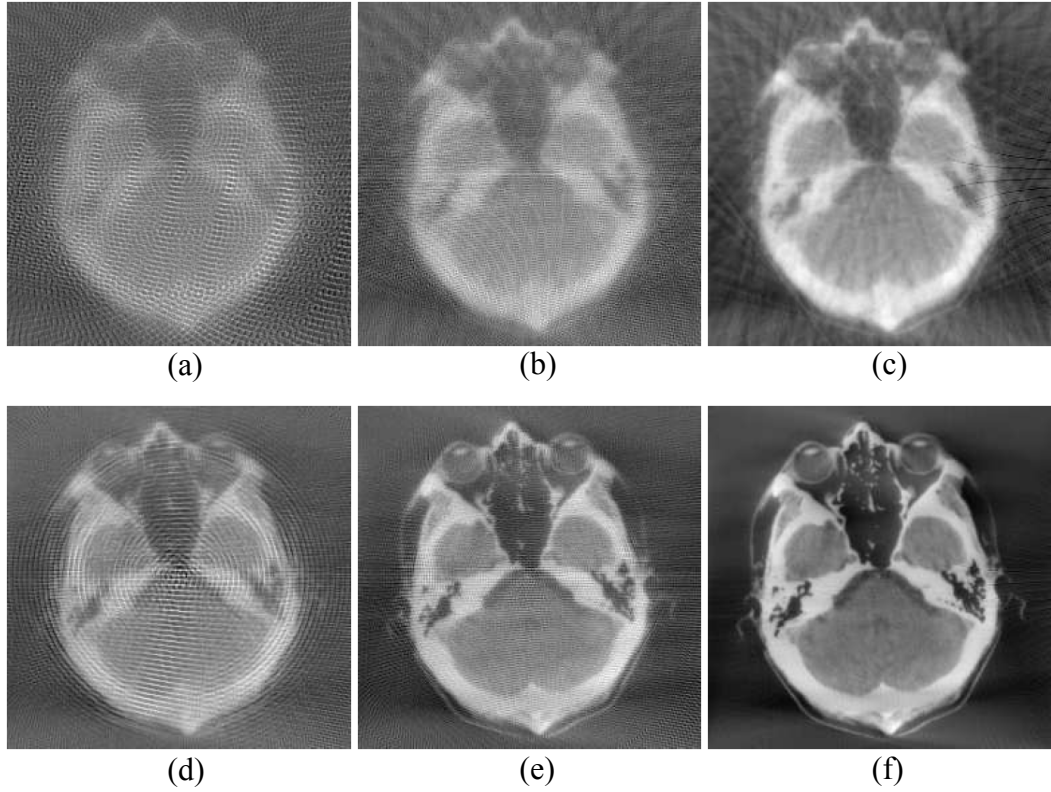


Fig. 2.5: Images reconstructed by SART ( $k = 1$ ). The original image is shown in Fig. 2.2(a). The following images are recovered from (a)  $m = 3840$  measurements ( $30 \text{ views} \times 128 \text{ rays/view}$ ). (b)  $m = 7680$  measurements ( $30 \text{ views} \times 256 \text{ rays/view}$ ). (c)  $m = 15360$  measurements ( $30 \text{ views} \times 512 \text{ rays/view}$ ). (d)  $m = 23040$  measurements ( $180 \text{ views} \times 128 \text{ rays/view}$ ). (e)  $m = 46080$  measurements ( $180 \text{ views} \times 256 \text{ rays/view}$ ). (f)  $m = 92160$  measurements ( $180 \text{ views} \times 512 \text{ rays/view}$ ). The system settings in all recoveries are  $d = 1.5 \times 256 \times \sqrt{2}$ ,  $\beta_{\min} = -\pi/2$ ,  $\beta_{\max} = \pi/2$ ,  $\gamma_{\min} = -\pi/7$ ,  $\gamma_{\max} = \pi/7$ .

particular, extends to an hour, FBP has much higher reconstruction speed; completes its operation in a few seconds.

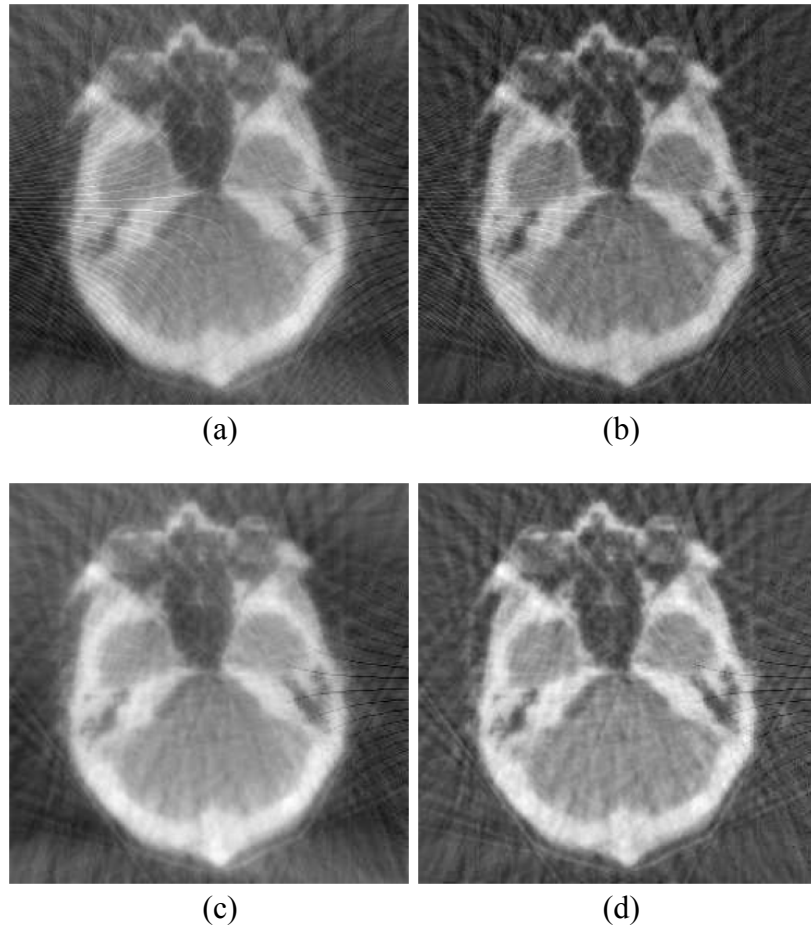


Fig. 2.6: Images reconstructed by iterative techniques ( $k = 1, 10$ ).  $m = 15360$  measurements ( $30$  views  $\times$   $512$  rays/view) are used by (a) ART ( $k = 1$ ), (b) ART ( $k = 10$ ), (c) SART ( $k = 1$ ), (d) SART ( $k = 10$ ).

## CHAPTER 3

### COMPRESSED SENSING

#### 3.1 Introduction

CS enables the accurate recovery of signals, images, and other data from much fewer samples than those obeying the Nyquist criterion [68]-[69]. There are two crucial observations in the CS framework. The first is that most objects we are interested in acquiring are sparse or compressible in the sense that they can be encoded with just a few numbers without much numerical or perceptual loss. The second observation is that the useful information content in sparse or compressible signals can be captured via sampling or sensing protocols that condense signals into a small amount of data. Surprisingly, many such protocols do nothing more than linearly correlate the signal with a fixed set of signal-independent waveforms. These waveforms, however, need to be incoherent with the family of waveforms in which the signal is compressible. One then typically uses numerical optimization to reconstruct the signal from the linear measurements of the form,

$$Ax = b \tag{3.1}$$

which is an underdetermined system of equations. Having the measurements  $b$  and the acquisition model  $A$ , the aim is to find a solution for the unknown  $x$ . The least-squares solution to such problems is to minimize the  $l_2$ -norm, i.e., the minimization of the amount of energy in the system. This is usually simple mathematically, involving only a matrix multiplication and pseudo-inversion. However, this leads to poor results for many practical applications for which the unknown elements have nonzero energy. To enforce the sparsity constraint when solving for the underdetermined system of linear equations, one can minimize the number of nonzero components of the solution. Recall that the function counting the number of

non-zero components of a vector is called the  $l_0$ -norm. Solving the problem of  $l_0$ -norm minimization usually requires combinatorial optimization. Donoho [41] proved that for many problems it is probable that  $l_1$ -norm is equivalent to  $l_0$ -norm in a technical sense: This equivalence result allows one to solve the  $l_1$  problem, which is easier than the  $l_0$  problem. Finding the candidate with the smallest  $l_1$ -norm can be expressed relatively easily as a linear program for which efficient solution methods already exist [70].

### 3.2 The Theory of CS

Suppose  $s$  is an unknown vector (a discrete time signal) in  $\mathbf{R}^N$  and compressible by transform coding using a known transform (e.g., wavelet, Fourier). All we have about  $s$  are  $m$  linear measurements of the form

$$y_k = \langle s, \varphi_k \rangle \quad k=1, \dots, m \quad \text{or} \quad y = \Phi s \quad (3.2)$$

where  $\varphi_k \in \mathbf{R}^N$  are known measurement vectors. The CS theory [41] asserts reconstructing  $s$  using these  $m$  observations under certain assumptions. Of special interest is the vastly underdetermined case,  $m \ll N$ , where there are many more unknowns than observations.

Let  $\Psi$  be an  $N \times N$  unitary transformation matrix with basis vector  $\psi_i$  as the  $i^{\text{th}}$  column. Suppose that  $s$  has a sparse representation in basis  $\psi_i$ , meaning that  $K$  most important coefficients in the representation allow a reconstruction with  $l_2$  error,

$$\|s - s_K\|_2 = \|\zeta - \zeta_K\|_2 < \varepsilon \quad (3.3)$$

where  $\zeta$  is the transform coefficient vector,  $\zeta_K$  is the vector of  $K$  most important coefficients appearing in  $\zeta$  and zeros elsewhere, and  $s_K$  is the reconstruction from  $\zeta_K$ . In this framework,  $s$  is said to be compressible when the error  $\|s - s_K\|_2$  is less than a tolerable noise level  $\varepsilon$ . It is possible to reconstruct  $s$  from  $m = O(K \log(N))$  measurements through (3.2) with accuracy comparable to that which would be possible if the  $K$  most important coefficients of  $s$  were directly observable [41]. Moreover, a good approximation to the  $K$  important coefficients can be extracted from the  $m$  measurements by solving the convex optimization problem:



$$\min_x \|\Psi^T x\|_1 \quad \text{subject to} \quad \Phi x = y \quad (3.4)$$

provided that the matrix  $\Phi \in \mathbf{R}^{m \times N}$  obeys the *uniform uncertainty principle* (UUP) [46] or equivalently the *restricted isometry property* (RIP) [71]. In words, we seek an  $x$  having coefficients  $\xi = \Psi^T x$  with smallest  $l_1$ -norm that is consistent with the information  $y_k = \langle \Psi^T s, \varphi_k \rangle$ . In transform domain, a good approximation to  $s_K$  can also be sought explicitly by solving

$$\min_{\xi} \|\xi\|_1 \quad \text{subject to} \quad \Phi \Psi \xi = y \quad (3.5)$$

When the sought vector itself is exactly  $K$ -sparse, meaning that only  $K$  of its elements are non-zero, an almost exact recovery from the  $m$  measurements is possible with minimum  $l_1$ -norm,

$$\min_x \|x\|_1 \quad \text{subject to} \quad \Phi x = y \quad (3.6)$$

In most practical situations, observations are imperfect, i.e., measurements are noisy:  $y = \Phi s + e$ . It is assumed that the perturbation is bounded by a known amount  $\|e\|_2 < \varepsilon$ . Having inaccurate observations and incomplete information, a stable recovery of sparse  $s$  is possible by solving

$$\min_x \|x\|_1 \quad \text{subject to} \quad \|\Phi x - y\|_2 \leq \varepsilon \quad (3.7)$$

When  $s$  is compressible,  $x$  in the  $l_1$ -norm minimization problem is replaced by  $\Psi^T x$  and  $\varepsilon$  is set so as to bound the error in (3.3) as well [68].

It is compulsory to design a measurement matrix that obeys UUP or RIP in (3.4)-(3.7) for a good recovery. It is notable to say that *random matrices with independent identically distributed entries, matrices with rows from the discrete Fourier transform matrix, and more generally matrices with rows from an orthonormal matrix* obey such properties [46]. Depending on the obedience of  $\Phi$ , the success of a recovery, i.e., the approximation to  $s$  (or  $s_K$ ) is a probabilistic issue [47]. It may be necessary to get more measurements than the theory suggests in

order to fetch useful information content in  $\varsigma$  (or  $\varsigma_K$ ). For practical purposes, the probability of failure is zero [68] as long as  $m$  is sufficiently large.

### 3.3 Intuitive Examples of CS and Applications

Let  $x$  be a reconstruction for  $s$  (either sparse or compressible) with constraint  $y = \Phi s$  or  $y = \Phi s + e$ . A popular choice for  $x$  is the solution of the least norm,

$$\min_x \|\Phi x - y\|_2 \quad (3.8)$$

i.e.,  $(\Phi^T \Phi)^{-1} \Phi^T y$ . Given the constraint, the CS based approach extracts the one which is the most sparse (or the most compressible in the case of compressible  $s$ ) among all solutions in the set  $\{\text{Null}(\Phi) + x\}$  where  $\text{Null}(\Phi)$  denotes the null space of  $\Phi$ . As an illustration, consider the cases listed in Table 3.1: 20-sparse and compressible signals are recovered from compressive measurements. Both signals have equal length 512 and norm 4.47. Entries of  $\Phi \in \mathbf{R}^{128 \times 512}$  are selected from  $\mathcal{N}(0,1)$  distribution, i.e., zero mean Gaussian ensembles with unit variance ( $\sigma^2 = 1$ ). The noise pattern in the measurements is additive:  $y_k = \langle s, \varphi_k \rangle + e_k$  with  $e_k \sim \mathcal{N}(0, 0.25)$ . Table 3.1 also summarizes the recovery errors in different configurations.

For noisy configurations,  $\varepsilon$  is 6.32, a little bit larger than the error norm,  $\|e\|_2 = 5.58$ ; the SNR values,  $\|\Phi s\|_2 / \|e\|_2$ , are 9.08 and 9.27, respectively in the 1<sup>st</sup> and 2<sup>nd</sup> rows of Table 3.1. The same signal is used in all sparse cases. The recoveries shown in Figs. 3.1 and 3.2 are consistent with the error results. Namely, the least norm solution in Fig. 3.1(b) does not provide a reasonable approximation to the desired  $s$ . Fig. 3.1(c) shows an almost perfect recovery of the 20-sparse signal in the noiseless case. Even with significant noise perturbations, (SNR: 9.08  $\equiv$   $\sim$ 19.1 dB, 9.27  $\equiv$   $\sim$ 19.3 dB), the CS based solutions provide good approximations to significant terms in Fig. 3.1(d) and Fig. 3.2(b).

Table 3.1: 1-D signal recovery errors,  $\|x - s\|_2$ .

| case                 | solution of | $\ x - s\ _2$         |
|----------------------|-------------|-----------------------|
| 20-sparse, noisy     | (13)        | 1.08                  |
| compressible, noisy  | (13)        | 0.95                  |
| 20-sparse, noiseless | (12)        | $1.69 \times 10^{-5}$ |
| 20-sparse, noiseless | (14)        | 3.87                  |

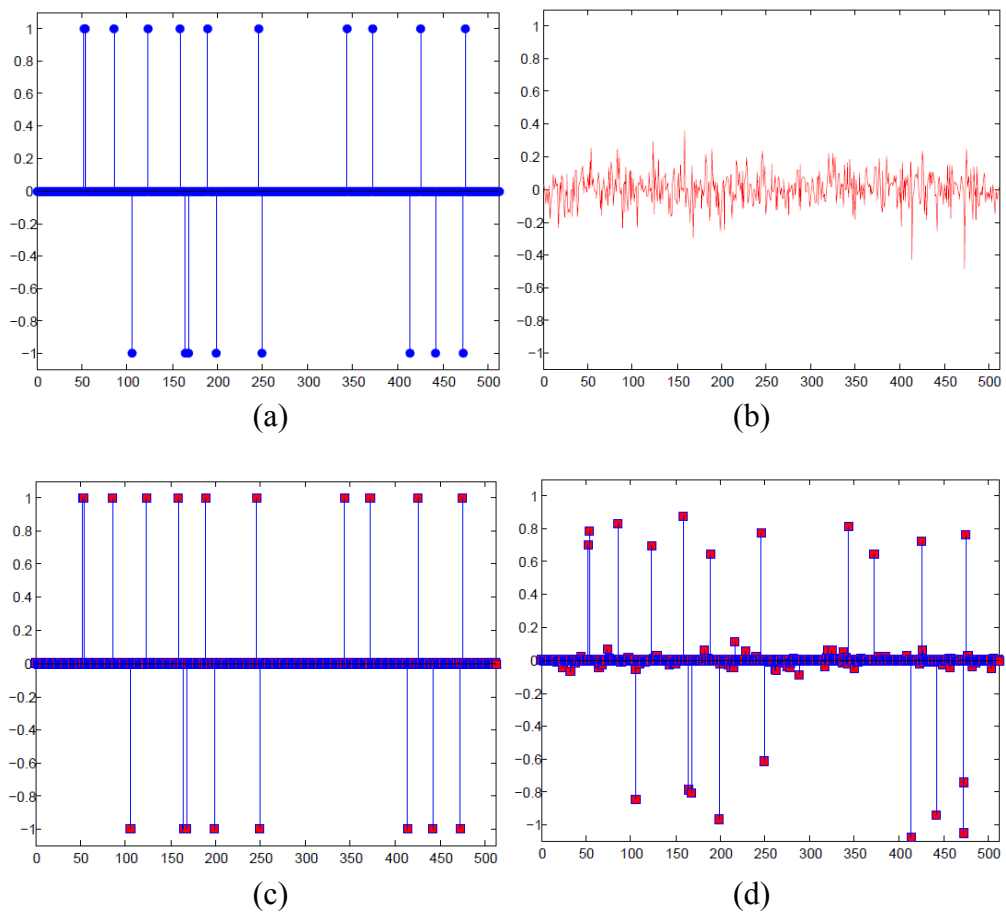


Fig. 3.1: 1-D sparse signal reconstruction. (a) Original sparse signal. There are  $K = 20$  non-zero coefficients taking values  $\pm 1$ . (b) Minimum error norm solution from noiseless measurements by using  $\Phi^T(\Phi^T\Phi)^{-1}y$ . (c) Sparse signal recovered from noiseless measurements by  $l_1$ -norm minimization in (3.6). (d) Sparse signal recovered from noisy measurements ( $\sigma = 0.5$ ) by  $l_1$ -norm minimization in (3.7).

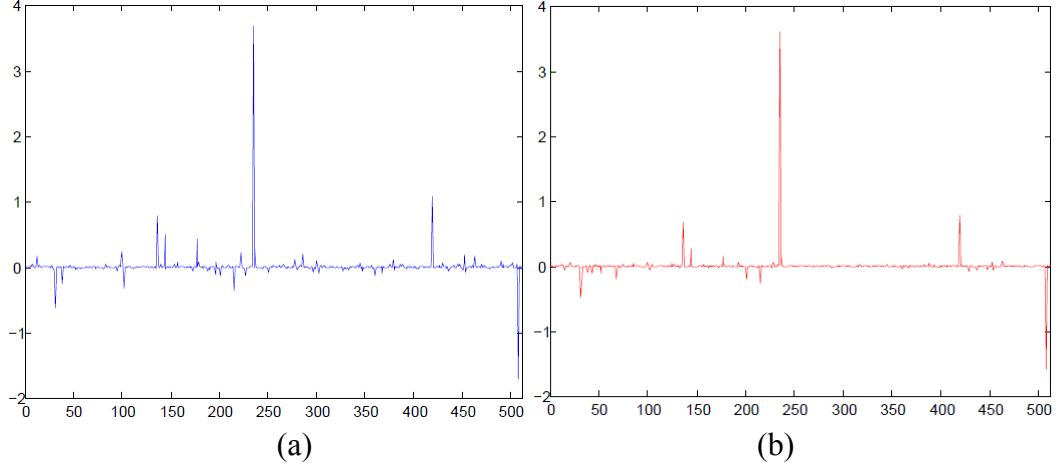


Fig. 3.2: 1-D compressible signal reconstruction. (a) Original compressible signal. (b) Compressible signal recovered from noisy measurements ( $\sigma = 0.5$ ) by  $l_1$ -norm minimization in (3.7).

Extension of the 1-D CS based reconstruction examples to 2-D signals or images is made simply by representing images as a single column vector provided that the images have good sparse representations. Many natural images are not sparse, but they are compressible in the sense that they have concise representations when expressed in the proper basis. The selection of basis is important to exploit the compressibility of an image. For example, consider the  $256 \times 256$  non-sparse head phantom image shown in Fig. 3.3(a) and some of its representations in Fig. 3.3(b)-(d). The gradient magnitude image (GMI) which is defined by the  $l_2$ -norm of its discrete gradient is the most compressible representation. It has less number of terms that are closer to zero as compared to other transform coefficients (see Fig. 3.4). Having the least  $l_1$ -norm, the vector of GMI is utilized in (3.6) to recover the original image from few Fourier measurements:

$$\min_x \|g_x\|_1 \quad \text{subject to} \quad F_r(x) = y \quad (3.9)$$

where  $g_x$  is the GMI of  $x \in \mathbf{R}^{256 \times 256}$  in vector form and  $F_r(\bullet)$  is the row deficient Fourier operator. The data acquisition matrix  $\Phi \in \mathbf{R}^{5482 \times 65536}$  which consists of a randomly shifted delta spike in its rows is inherent in  $F_r(\bullet)$ .  $y \in \mathbf{R}^{5482}$  whose distribution is shown in Fig. 3.5(a) is the vector of under-sampled Fourier

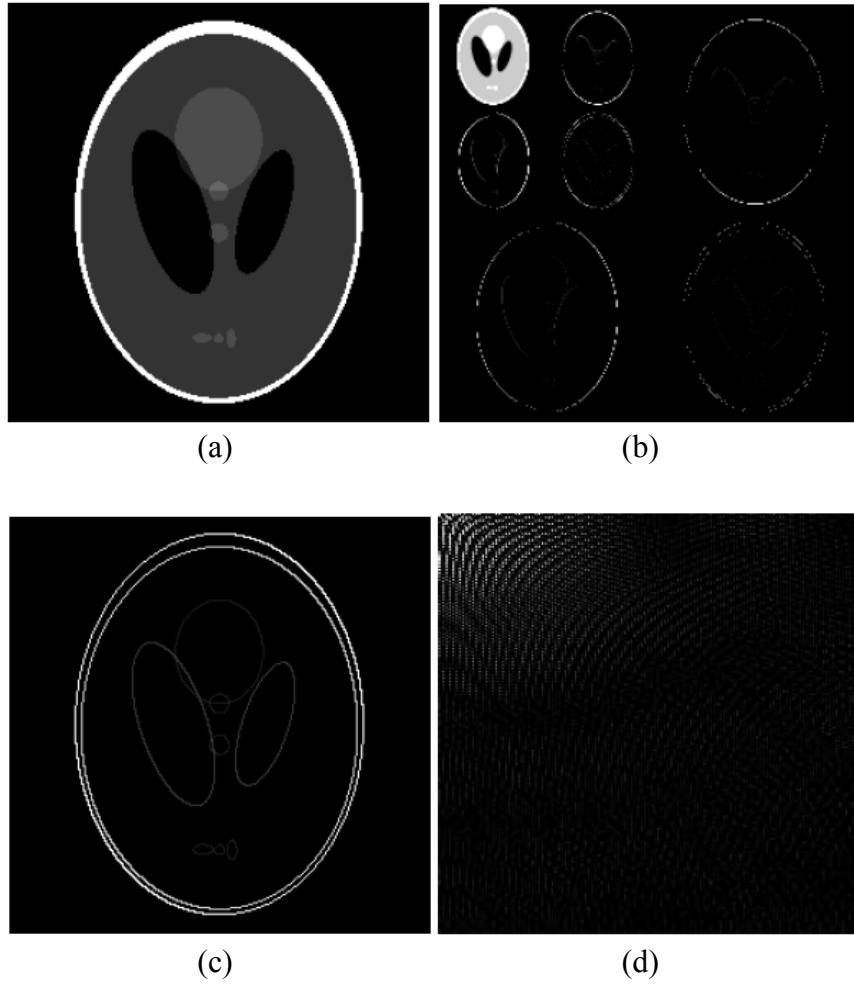


Fig. 3.3: Sparse representations of the phantom image. (a)  $256 \times 256$  synthetically generated head phantom image. (b) Imaging of (Haar) DWT coefficients. It is 4765-sparse. (c) GMI. It is 2184-sparse (d) Imaging the DCT coefficients. All coefficients are non-zero.

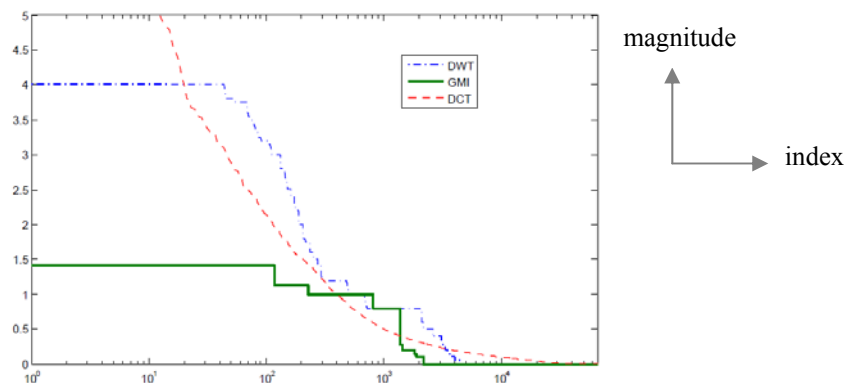


Fig. 3.4: Plot of the magnitude sorted coefficients in Fig. 3.3(b)-(d). The  $l_1$ -norm values are 2985, 1460 and 4137 for DWT, GMI and DCT, respectively.

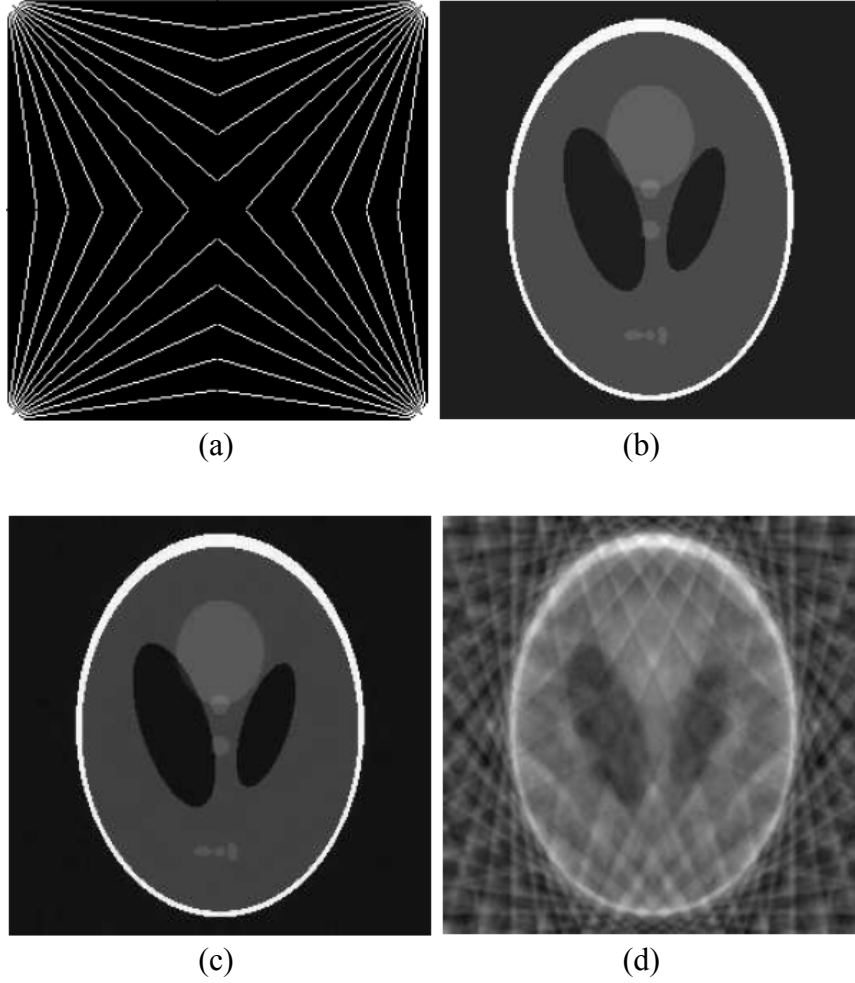


Fig. 3.5: CS reconstruction of the phantom image. (a) The sampling pattern of Fourier coefficients on 2-D Fourier space. The display area is  $[0, 2\pi) \times [0, 2\pi)$ . Only the sampled coefficients are used for recoveries in (b)-(d). (b) Image recovered from noise-free Fourier coefficients by using  $l_1$ -norm minimization in (3.9). (c) Image recovered from noisy Fourier coefficients ( $\sigma=5 \times 10^{-3}$ ) by using  $l_1$ -norm minimization in (3.10) ( $\varepsilon=1$ ). (d) Image recovered from noise-free Fourier coefficients by inverse FT.

coefficients of  $x$ . An almost perfect recovery shown in Fig. 3.5(b) is obtained by solving (3.9). When  $y$  is perturbed by an additive Gaussian ensemble with  $\mathcal{N}(0, 25 \times 10^{-6})$ , the stable recovery shown in Fig. 3.5(c) is obtained through

$$\min_x \|g_x\|_1 \quad \text{subject to} \quad \|F_r(x) - y\|_2 < \varepsilon \quad (3.10)$$

Even with noisy coefficients, the CS solution has better visual quality than the noise-free solution of the inverse Fourier transform shown in Fig. 3.5(d). Table 3.2 summarizes the PSNR values in recoveries for different noise power and error bounds in (3.10). No stable recovery is obtained for the parameter settings corresponding to the striped cells.

Table 3.2: PSNRs (dB) of the 2-D signal recoveries.

| $\sigma \downarrow, \varepsilon \rightarrow$ | <b>0.05</b> | <b>0.5</b> | <b>1</b> | <b>2</b> | <b>4</b> |
|--|-------------|------------|----------|----------|----------|
| $5 \times 10^{-4}$                           | 96.16       | 92.11      | 89.95    | 87.01    | 83.22    |
| $5 \times 10^{-3}$                           |             | 88.59      | 87.59    | 85.30    | 82.22    |
| $5 \times 10^{-2}$                           |             |            |          |          | 76.48    |

The examples above essentially serve the purpose of giving insights about the CS theory and its applications. A large collection of resources where CS has been studied from both theoretical and practical standpoint can be found in <http://dsp.rice.edu/cs>. Similar to our image reconstruction example, the initial applications in MRI [48]-[51] are based on recovering from few Fourier coefficients in  $k$ -space. In addition to GMI, they include studies considering image representations in wavelet and Fourier domains. More recently, the sparsity of CT images has also been exploited in image reconstruction algorithms [52], [54], [57], [59], [62]. Both the data acquisition system which is expected to provide incoherent measurements and the image reconstruction algorithm having high convergence speed are crucial for integration of CS into CTI systems. Regarding these issues, we discuss the recent modalities in the next Chapter before proceeding with the proposed algorithms.

## CHAPTER 4

### COMPRESSED SENSING BASED COMPUTERIZED TOMOGRAPHY IMAGING

#### 4.1 Compressed Sensing for CT Imaging

Using less than 10% of the coefficients, the CS solution reveals a significant improvement over the recoveries from 2-D inverse Fourier transform. In a CTI system, we are supplied with projection data only, not the Fourier samples of the original image. At first glance, it can be thought that the 2-D Fourier space can be filled by the coefficients of view projection data with the aid of Fourier Slice Theorem (FST) [4]. The acquired data has the fidelity

$$F(Wx) = C \quad (4.1)$$

where  $F$  is the Discrete Fourier Transform (DFT) operator, and  $C$  is the vector of DFT coefficients of  $p_i$ 's. The overall measurement system  $F(W\bullet)$  operates on  $x$  in the following order:

- 1) compute  $p_i$ 's for each parallel beam,
- 2) compute DFT coefficients of  $p_i$ 's in each beam.

The  $F(W\bullet)$  operates similar to  $F_r(\bullet)$  in (3.9) since  $W \in \mathbb{R}^{m \times N}$  is a row deficient matrix. The DFT coefficients constitute radial samples on the 2-D Fourier space. These samples can be considered as random measurements from the original image if view angles are aligned randomly. Defining the data acquisition system as the row deficient Fourier operator is reasonable in the sense that the forward/backward Fast Fourier Transform (FFT) routines are available in a regular coordinate system and few Fourier measurements suffice for recovery. The processing load and time are reduced by using FFT routines without creating large DFT matrices explicitly. To



exploit FFT algorithms, however, Fourier measurements should be mapped into the regular rectangular system. The estimation of Fourier samples on the rectangular system is error prone due to interpolations. It is possible to keep error at a lower level if the 2-D forward/backward Fourier transform is defined directly on the polar system and conversion to the rectangular system is avoided. However, there is no such a well defined transformation on the polar coordinate system as far as we know. Since the density of radial points becomes sparser as one gets farther away from the center, the interpolation error also becomes larger. This implies that there is greater error in the calculation of high frequency components in an image than in low frequency ones. To reduce the interpolation errors, the sampling rate along the radial and angular directions should be high enough. However, the high sampling rate requires using more beams and/or rays at the expense of high radiation absorption.

Instead of employing an effective interpolation method or searching a suitable FFT routine for the polar coordinate system, only  $W$  can be used in

$$Wx = P \quad (4.2)$$

which is the same as equation (2.3). Dropping DFT operator out of (4.1) does not violate incoherence which says that unlike  $x$  the sensing waveforms have very dense representation in a sparsifying domain such as GMI. The stack of noise-like row vectors of  $W$  forms a random measurement matrix such that the sparsity basis need not even be known [68], [72]. Therefore, it is possible to have a good recovery with the CS based solution to

$$\min_x \|g_x\|_1 \quad \text{subject to } Wx = P \quad (4.3)$$

If the projection data  $P$  is contaminated, the data fidelity is relaxed by  $\|Wx-P\|_2 \leq \varepsilon$ .

If the number of rows obeys

$$m = O(K \log N) \quad (4.4)$$

then with probability very close to one  $W$  obeys UUP [73]. That is to say, while  $x$  is entirely concentrated on a small set in the sparsifying domain, it is spread out more or less evenly in the measurement domain. The number of measurements that we need to reconstruct an image depends on how different the two domains are. For example, more than 10520 rays are required to reconstruct the image in Fig. 3.3(a) by minimizing the  $l_1$ -norm of its GMI. If the number of rays is kept constant at 512, very few numbers of beams seem to suffice. Most practices including our numerical studies, however, necessitate more views than the theory suggests.

Switching from (4.1) to (4.2) has the following benefits: 1) The interpolation errors imposed by polar to rectangular conversion are avoided. 2) Contrary to the necessity of handling the imaginary parts of DFT coefficients, we are free to use up our quota for the number of measurements by getting all real and only desired projections. 3)  $W$  can be formed for any scanning configuration including the common fan beam projection. (It is not limited to the parallel beam.)

The  $l_1$ -norm of GMI is commonly known as the TV of the reconstructed image:

$$\sum_{r,c} \sqrt{|x_{r+1,c} - x_{r,c}|^2 + |x_{r,c+1} - x_{r,c}|^2} \quad (4.5)$$

where  $r$  and  $c$  denote the image pixel coordinates at *row* and *column* axes, respectively. Simply denoting (4.5) with the TV-norm, (4.3) can be equivalently expressed as

$$\min_x \|x\|_{\text{TV}} \quad \text{subject to } Wx = P \quad (4.6)$$

The following sub-sections discuss the recently introduced CS based algorithms that try to seek an  $x$  having the minimum TV and being subject to the constraint dictated by (4.2).

## 4.2 POCS Based Solution

The originally proposed ASD-POCS algorithm [59] solves the optimization problem (4.6) with an extension of the constraint  $x \geq 0$ . It alternates an iteration of

POCS with the steepest-descent step, while adapting the steepest-descent step-size to ensure that the image constraints are satisfied. POCS and ASD run consecutively in the following manner: 1) POCS enforces non-negativity and ensures data consistency that estimated image satisfies the measurements by a tolerable distance, i.e.,  $\|Wx-P\|_2 \leq \varepsilon$ . 2) ASD nudges the image toward the minimum-TV solution by changing the gradient-step-size  $\lambda_{asd}$  adaptively. POCS followed by ASD defines a single iteration of the ASD-POCS algorithm. The iterations cease when various controls pass: the optimality conditions derived from the necessary Karush-Kuhn-Tucker conditions are satisfied (see Section 2.3 of [59]); the distance to projection data is negligible or the POCS step size,  $\lambda_{art}$  (also called the *ART relaxation-parameter*), is too small. The steps of ASD-POCS algorithm are summarized below:

---

**Method III:** Pseudo code for ASD-POCS algorithm

---

```

1   initialize  $\lambda_{art}, \lambda_{asd}, r_{art}, r_{asd}, r_{max}, r, \varepsilon, x$ 
2   repeat until stopping criteria is satisfied
3    $f_0 \leftarrow x$ 
4    $x \leftarrow$  compute ART with POCS step size  $\lambda_{art}$ 
5    $x_j \leftarrow 0$  if  $x_j < 0, \forall j$ 
6    $\lambda_{art} \leftarrow \lambda_{art} \cdot r_{art}$ 
7   return  $x$  if last iteration
8    $dp \leftarrow \|f - x\|_2$ 
9    $dd \leftarrow \|Wx - P\|_2$ 
10   $f_0 \leftarrow x$ 
11   $\lambda_{asd} \leftarrow dp \cdot r$ , if 1st iteration
12   $x \leftarrow$  compute steepest-descent with step-size  $\lambda_{asd}$ 
13   $ds \leftarrow \|f_0 - x\|_2$ 
14   $\lambda_{asd} \leftarrow \lambda_{asd} \cdot r_{asd}$ , if  $(ds / dp) > r_{max}$  and  $dd > \varepsilon$ 
15  end

```

---

The image vector  $f_0$  at lines 3 and 10 is used as a place-holder image in order to compute changes in the image after POCS and ASD steps. The sets of lines {4, 5, 6} and {11, 12, 14} correspond to execution lines of POCS and ASD, respectively. At line 4, POCS employs ART which is working simply based on Kaczmarz-method (see Chapter 7 of [4]). The number of ART iterations is controlled by  $\lambda_{art}$  which is decreased steadily by  $r_{art} < 1$  at line 6. False image elements are negated at line 5. Line 10 initializes the steepest-descent step-size with the aid of a multiplier  $r < 1$  in the 1<sup>st</sup> iteration. Lines 12 and 14 are used to implement the steepest-descent algorithm and to adapt its step-size, respectively. The number of ASD iterations,

$n_{sd}$ , is determined based on the product  $n_{sd} \times r$  which is expected to be greater than or equal to 1 in order to make the change in the image due to the steepest-descent,  $ds$ , and the change in the image due to POCS,  $dp$ , are comparable. The adaptation rule is steadily decrease the steepest-descent step-size by  $r_{asd} < 1$  when the ratio of  $ds$  to  $dp$  is greater than  $r_{max} \approx 1$  except when the data residual computed at line 9 remains within the tolerance,  $\varepsilon$ . Once the current image satisfies the data-tolerance condition, the steepest descent step-size is not reduced any more. Therefore, it is allowed to become larger than POCS step-size, because POCS step-size decreases always as iterations proceed. As a result, the image drifts more toward the lower-TV images. This adaptation balances the POCS and steepest-descent steps in a controlled manner and lets the algorithm converge faster than those not having this balance [52]. ASD-POCS ensures the constraints by retaining the convergence properties of ART [74]. Given the set of images complying with these constraints, the algorithm, however, does not guarantee the minimum-TV image. The solution of the constrained TV-minimization problem depends on the initialization of the parameters at line 1. If the optimality conditions are violated, it should be rerun with new parameters.

There are some advantages coming with using ASD-POCS. Varied constraints and alternative methods are easily incorporated. For example, POCS steps can be extended by additional physical constraints to image non-negativity. The ART operator can be substituted entirely by superior techniques such as SART [56], [75]. ASD steps can be tailored to simply use a small constant step-size [54] or a step-size computed by back-tracking line-search. ASD can be also replaced by more effective gradient-descent methods. Another advantage of ASD-POCS is its usability to solve large linear systems. It does not require explicit knowledge of the system matrix. Only a row vector of  $W \in \mathbf{R}^{m \times N}$  is processed at each iteration of ART. If the gradient of TV-norm needed by ASD is approximately computed by

$$\frac{\partial}{\partial x_{r,c}} \|x\|_{TV} \cong \frac{(4x_{r,c} - x_{r+1,c} - x_{r,c+1} - x_{r-1,c} - x_{r,c-1})}{\|x\|_{TV}} \quad (4.7)$$

no matrix-vector multiplication except the residue at line 9 remains in Method III.

Assuming the main loop of ASD-POCS ends up with  $k_p$  iterations, the total number of operations (multiplication and addition) is of the order  $O(k_p(m+n_{sd})N)$ . The processing load is dominated by ART since  $m$  is usually greater than  $n_{sd}$ . Although ART is conceptually simpler than FBP, it lacks speed of implementation. Similarly, despite its simplicity, the steepest-descent method has also low convergence rate. Therefore, the slow convergence speed is the major drawback of the ASD-POCS algorithm.

### 4.3 Fourier Transform Based Solution

Fourier transform based algorithm brings the projection data into the image's Fourier space, ensuring the consistency of the transformed projection data with the reconstructed image's Fourier transform. Mathematically,

$$\|F_r(x) - C\|_2 < \varepsilon \quad (4.8)$$

where  $F_r(\bullet)$  and  $C$  are, respectively, as defined in (3.9) and (4.1). Having the same spirit with ASD-POCS, Fourier transform based algorithms that we call ASD-FT hereafter, consist of two major steps: ASD and FT. It minimizes the image TV reckoning with the constraints (4.8) and

$$\text{Re}(x) \geq 0, \quad \text{Im}(x) = 0 \quad (4.9)$$

in the following manner: 1) FT enforces constraints (4.8)-(4.9) and ASD reduces the total variation of the reconstructed image, 2) FT and ASD alternate inside the main loop of the algorithm. The major difference of ASD-FT as compared to ASD-POCS is the inspection of data consistency in the Fourier space. In particular, lines 4, 5 and 9 in Method III are replaced by the corresponding lines in Method IV.

---

**Method IV:** Pseudo code differing in ASD-FT.

---

4.1  $X \leftarrow$  **compute** image transform,  $F(x)$   
4.2  $X_r \leftarrow C$   
4.3  $x \leftarrow$  **compute** inverse transform,  $F^{-1}(X)$   
5.1  $x_j \leftarrow 0$  **if**  $x_j < 0$ ,  $\forall j$   
5.2  $x_j \leftarrow 0$  **if**  $\text{Im}(x_j) \neq 0$ ,  $\forall j$   
9  $dd \leftarrow \|F_r(x) - C\|_2$

---

The FT consists of the five sub-steps at lines 4.1-5.2 in Method IV. At line 4.1, the Fourier transform coefficients of the current estimate are computed. Being a reduced set of  $X$ ,  $X_r$  represents the set of transform coefficients only at frequencies corresponding to the locations on Fourier space of the transform coefficients in  $C$ . The elements of  $X_r$  are replaced by corresponding elements of  $C$  at line 4.2, enforcing the data consistency given by (4.8). The image estimation is updated by inverse Fourier transform at line 4.3. These ordered sub-steps, i.e., (4.1)-(4.3) correspond to ART computation in Method III. Positivity and realness of image elements are satisfied at lines 5.1 and 5.2, respectively. The POCS step-size in Method III may optionally be used in ASD-FT as a relaxation parameter at line 4.2: Instead of direct substitution of elements in  $X_r$  and  $C$ , the value of  $\lambda_{art}C + (1-\lambda_{art})C_c$  can be assigned to  $X_r$  [57]. ( $C_c$  represents the Fourier transform coefficients of the projection of current estimate.) The data residual is computed at line 9 where  $F_r(x)$  gives new  $X_r$  as a consequence of the FT step.

Due to the parallelism between the steps of ASD-FT and ASD-POCS, the advantages discussed in Section 4.2 are shared with ASD-FT as well. Moreover, the use of FFT routines at lines 4.1 and 4.3 reduces operations in data consistency steps and accelerates the convergence speed. Assuming  $k_f$  iterations are performed in the main loop, the total number of operations are of the order  $O(k_f(\log_2 N + n_{sd})N)$  (usually  $N \ll 2^m$ ). Despite the acceleration in the implementation, ASD-FT suffers from the mismatched samples of  $F_r(x)$  and  $C$ . For example, in non-diffracting parallel beam CT, FST places the transform coefficients of the projection data along the radial lines over the image's Fourier space. The linear imaging model is appropriate for this particular case and  $C$  obeys exactly (4.1). In diffraction tomography [57], on the other side, the transform coefficients are placed along semicircles rather than straight lines by Fourier diffraction projection theorem [76]. Since the contribution proportion of each image element to projection data is not explicit,  $C$  should be rather expressed by  $F(P)$  instead of  $F(Wx)$ . The critical issue in computing  $\|F_r(x) - C\|_2$  is to match the samples of  $F_r(x)$  and  $C$  accurately. Considering the discussions on interpolations in Section 4.1, the best matching samples should be corrected to improve the data consistency. Otherwise, solutions of ASD-FT show higher degradations than FBP.

## CHAPTER 5

### SECOND ORDER CONE PROGRAMMING

The integration of CS theory within the CT imaging system has been discussed in Chapter 4, and the recently introduced POCS and FT based algorithms have been gone over in this regard. Generally speaking, these algorithms have two parts running independently and sequentially in a repeated manner. While data fidelity to the constraints is satisfied in the first part, a lower TV image, i.e., a sparser gradient image representation is sought in the second part. Since the only interaction between them is using the one's output in the other, the reconstruction speeds are not as high as desired. In this chapter, we reformulate the original problem as second order cone programming and solve it via a generic logarithmic-barrier method. This scheme allows minimizing an unconstrained problem alone while staying inside the feasible region as iterations lead to the optimum solution. Therefore, it allows a closer approach to the solution rapidly than offered by other CS based algorithms.

#### 5.1 General Perspective

A second order cone program (SOCP) is a convex optimization problem of the form,

$$\min_x f^T x \text{ subject to } \|A_j x + b_j\|_2 \leq c_j^T x + d_j, \quad j = 1, 2, \dots, N \quad (5.1)$$

where  $x \in \mathbf{R}^N$  is the optimization variable, and the problem parameters are  $f \in \mathbf{R}^N$ ,  $A_j \in \mathbf{R}^{n_j \times N}$ ,  $b_j \in \mathbf{R}^{n_j}$ ,  $c_j \in \mathbf{R}^N$ , and  $d_j \in \mathbf{R}$ . The constraint

$$\|A_j x + b_j\|_2 \leq c_j^T x + d_j \quad (5.2)$$

is called the second order cone constraint of dimension  $n_j-1$ . The SOCP (5.1) is a convex programming since the objective is a convex function and the constraints define a convex set [77].

Second order cone constraints can be used to represent several common convex constraints. For example, when  $A_j = 0$  for  $j = 1, 2, \dots, N$ , the SOCP reduces to a linear program (LP). When  $c_j = 0$  for  $j = 1, 2, \dots, N$ , the SOCP is equivalent (assuming  $d_j \geq 0$ ) to the convex quadratically constraint quadratic program (QCQP),

$$\min_x f^T x \text{ subject to } \|A_j x + b_j\|_2^2 \leq d_j^2, \quad j = 1, 2, \dots, N \quad (5.3)$$

Many other nonlinear convex optimization problems can be reformulated as SOCP [77]-[78]. A special kind of these problems is that involving sums of norms. For  $F_j \in \mathbf{R}^{n_j \times N}$  and  $g_j \in \mathbf{R}^{n_j}$ , the unconstrained problem

$$\min_x \sum_{j=1}^N \|F_j x + g_j\|_2 \quad (5.4)$$

can be expressed as a SOCP by introducing auxiliary variables,  $t_j \in \mathbf{R}^N$

$$\min_x \sum_{j=1}^N t_j \text{ subject to } \|F_j x + g_j\|_2 \leq t_j, \quad j = 1, 2, \dots, N \quad (5.5)$$

Other second order cone constraints can be incorporated in problem (5.5), e.g., linear equalities on  $x$ . In the next subsection, we reformulate the TV minimization problem as SOCP.

## 5.2 Problem Reformulation

It is possible to solve problem (4.6) after recasting it as SOCP,

$$\min_{u,x} \sum_j u_j \text{ subject to } \|D_j x\|_2 \leq u_j \quad (5.6)$$

$$Wx = P$$



where the index  $j = 1, 2, \dots, N$  stands for the  $j^{\text{th}}$  image element and holds the row and column indices  $(r, c)$  implicitly. The 2-vector  $D_j x$  can be interpreted as a kind of discrete gradient of the image vector  $x$  at the  $(r, c)$  pixel:

$$D_j x = \begin{bmatrix} D_{hj} x \\ D_{vj} x \end{bmatrix} = \begin{bmatrix} x_{r+1,c} - x_{r,c} \\ x_{r,c+1} - x_{r,c} \end{bmatrix} \quad (5.7)$$

where the row vectors,  $D_{hj}$  and  $D_{vj}$ , act as horizontal and vertical difference operators for the  $j^{\text{th}}$  pixel, respectively. The norm  $\|D_j x\|_2$  represents the gradient magnitude or the image variation at the  $j^{\text{th}}$  pixel. If the measurements are polluted, (5.6) is replaced by

$$\begin{aligned} \min_{u, x} \sum_j u_j \quad \text{subject to} \quad & \|D_j x\| \leq u_j, \\ & \|Wx - P\| \leq \varepsilon \end{aligned} \quad (5.8)$$

where  $\varepsilon \geq 0$  helps numerical convergence as in ASD-POCS and ASD-FT, and  $u_j \geq 0$  represents the  $j^{\text{th}}$  entry in vector  $u \in \mathbf{R}^N$ . The objective is a function of  $(x, u)$ . Its dependency on  $x$  can be seen more clearly if the objective is written as the inner product,  $[0^T \ 1^T][x^T \ u^T]^T$ . The use of a single vectorial variable for  $[x^T \ u^T]^T$  requires  $D_h$ ,  $D_v$ , and  $W$  matrices to be appended by zeros. To get rid of unnecessary matrix vector multiplications, it is rather preferred to keep current variables and write the objective as  $1^T u$ . One straight-forward technique to solve SOCP is to implement it using a log-barrier method [70]. The standard log-barrier method combines the inequality constraints with the objective by utilizing a penalty function of the form  $-\log(-f(x))$  which is infinite when the constraint  $f(x) < 0$  is violated. Using the penalty function, SOCP (5.6) turns out to be a linear constraint program (see Appendix B for details). It is further recast as an unconstrained program by incorporating the Lagrange multipliers  $v \in \mathbf{R}^m$  with the linear constraint  $Wx = P$ ,

$$\min_{u, x} \left[ 1^T u - \frac{1}{\tau^k} \sum_j \log \frac{1}{2} \left( f_j(u) - \|D_j x\|_2^2 \right) + v^T (Wx - P) \right] \quad (5.9)$$

The incorporation of all inequality constraints into the objective in (5.8) also makes it a generic unconstrained program,

$$\min_{u,x} \left[ 1^T u - \frac{1}{\tau^k} \left( \sum_j \log \frac{1}{2} \left( f_j(u) - \|D_j x\|_2^2 \right) + \log \frac{1}{2} \left( \varepsilon^2 - \|Wx - P\|_2^2 \right) \right) \right] \quad (5.10)$$

The functional  $f_j(u)$  is  $u^T \delta_j \delta_j^T u$ , giving the scalar value  $u_j^2$ ; and  $\delta_j$  is the Kronecker vector that is 1 at the  $j^{\text{th}}$  entry and zero elsewhere. As the log-barrier iterations,  $k$ , proceed,  $\tau^k > \tau^{k-1} > 0$  gets larger, ensuring the solution to (5.9) and (5.10) to approach the solution of (5.6) and (5.8), respectively (see §11.2.2 in [79]).

### 5.3 Solution Algorithm

At each log-barrier iteration, a series of quadratic approximations to the objective in (5.9)-(5.10) is minimized based on the Newton's method, which is again iterative. The exception is that the Lagrangian term is not included in the quadratic approximation to the objective in (5.9). A set of linear equations as a result of the minimization of quadratic approximations is solved to find the Newton step-direction. It might be necessary to modify the step-size to stay inside the feasible region defined by the inequality constraints. If a sufficient decrement is not achieved with optimal step-size, the set of equations, or equivalently the quadratic approximations, are updated using the current  $(x,u)$  value for the next Newton iteration. The derivations leading to the set of linear equations are mathematically intensified. A very good introduction of the key mathematical insights can be found in [70], and an explicit presentation of details is ranked in Appendix B. In order to present the solution algorithm plainly, only the major steps of the complete log-barrier implementation are summarized in Method V.

---

**Method V:** Pseudo code for the log-barrier algorithm.

---

```

1   initialize  $\tau^1, r, k_b, \varepsilon, n_{nw}, x, u$ 
2   repeat for index  $k \leftarrow 1$  to  $k_b$ 
3   repeat until  $\|f_0 - f(x, u)\|_2 < \varepsilon$ 
4    $f_0 \leftarrow f(x, u)$ 
5    $(H, h) \leftarrow$  compute linearized system parameters
6    $(\Delta x, \Delta u) \leftarrow$  compute Newton step-direction
7    $\lambda_{nw} \leftarrow$  compute Newton step-size
8    $(x, u) \leftarrow (x + \lambda_{nw} \Delta x, u + \lambda_{nw} \Delta u)$ 
9   end
10   $\tau^k \leftarrow r \cdot \tau^k$ 
11  end

```

---

Method V is given as a common algorithm for both (5.9) and (5.10). The outer and inner loops are designed for the log-barrier and Newton iterations, respectively. The number of log-barrier iterations,  $k_b$ , is calculated in advance using the relation  $r^{k_b} \tau = N' / \varepsilon$  (see §11.5.3 in [79]) where  $N'$  is the number of inequality constraints, either  $N$  or  $N+1$  depending on the problem (5.6) or (5.8), and  $r > 1$  is a multiplicative constant increasing  $\tau^k$  in succeeding iterations at line 10. The functional  $f$  at line 4 gives the value of objective function without the Lagrangian term. The scalar  $f_0$  is used as a placeholder cost in order to compute the Newton decrements at line 3. The set of equations is expressed in closed form,  $H z = h$ , where  $H$  has sizes of  $(2N+m) \times (2N+m)$  and  $2N \times 2N$ , respectively, for the problems (5.9) and (5.10). It is symmetric in both cases but not necessarily positive definite. Depending on the system characteristics, either SYMMLQ [80] or CG [65] method is employed at line 6 to solve  $H z = h$  iteratively for  $z = [\Delta x^T \ \Delta u^T \ v^T]^T$ , where  $v$  is nonexistent in case of (5.10). Considering the possibility that unit step-length along  $[\Delta x^T \ \Delta u^T]^T$ , i.e., the Newton step-direction, may violate the inequality constraints, an optimum step-size,  $\lambda_{nw} \leq 1$  that ensures the new point  $(x+s\Delta x, u+s\Delta u)$  to stay in the interior is searched at line 7. Newton iterations proceed until the decrement in the current iteration is less than a predefined tolerance,  $\varepsilon$ , or additionally the maximum number of iterations,  $n_{nw}$  is completed.

The log-barrier algorithm is efficient for achieving very good solutions in polynomial time [62]. Its outer loop does not change with the increased number of measurements,  $m$ , but the number of CG iterations and its operation time. Most of the processing time is spent for solving  $H z = h$ . Extra Newton iterations because of starting from an infeasible point also prolongs the convergence time. The elimination of  $\Delta u$  from  $z$  in the implementation reduces the problem size to  $(N+m) \times (N+m)$  and  $N \times N$ , respectively, for (5.9) and (5.10), which in turn relaxes the computations. Despite the elimination, the use of iterative techniques is still compulsory for large scale problems, e.g.,  $N$  is 65536 for a typical  $256 \times 256$  image and  $m$  maybe  $\sim N/5$ . If  $c$  is assumed to be the number of SYMMLQ or CG iterations in one iteration of Newton's method, the total number of operations required to solve the problems (5.9) and (5.10) are of the order  $O(k_b n_{nw} c (N+m)^2)$  and

$O(k_b n_{nw} c N^2)$ , respectively. Although complexity order of the log-barrier algorithm is higher than POCS or Fourier transform based methods, it is capable of converging faster to a better solution especially for small scale problems. Roughly speaking,  $k_p \gg n_{sd} > k_b$  and  $N \gg c \cong m \gg n_{sd} \cong n_{nw} \cong \log_2 N$ . Considering the proportionality of  $m$  with  $N$  as well, the log-barrier algorithm takes the advantage of Newton's method to end up with an accurate solution rapidly. When the problem size gets large, on the other hand, it suffers from huge matrix vector multiplications. The adverse effect of nested loops on convergence time becomes clearer. The auxiliary variables such as  $u$  and  $v$  also increase the problem size by a factor of two or more. Their involvement in mid-processing cannot be avoided completely even if the problem size is reduced.

#### 5.4 Experimental Results

The performance of the SOCP is investigated in three experiments: The first experiment (*E1*) aims to compare SOCP with conventional image reconstruction techniques. The second experiment (*E2*) aims to investigate the robustness of SOCP against additive white Gaussian noise. Finally, the third experiment (*E3*) aims to compare SOCP with other CS based solutions. The projection data are obtained using projection matrices that are constructed according to Method II in all experiments. PSNR is used as an objective quality measure in all recoveries. The displayed images are scaled arbitrarily for illustrative purposes. All algorithms are run on Intel® Core™ i7-2630QM CPU @ 2.00 GHz processor running Windows®7 OS.

In order not to be frustrated by long processing times or memory limitations due to large sized  $W$ , a  $32 \times 32$  test image shown in Fig. 5.1(a) is used in *E1* and *E3*. A large scale problem such as the reconstruction of the  $256 \times 256$  head phantom image introduced in Fig. 3.3(a) is considered in *E2* where the sparseness of  $W$  is utilized. A modified Hamming window is used in *E1* to filter the projection data in the frequency domain.

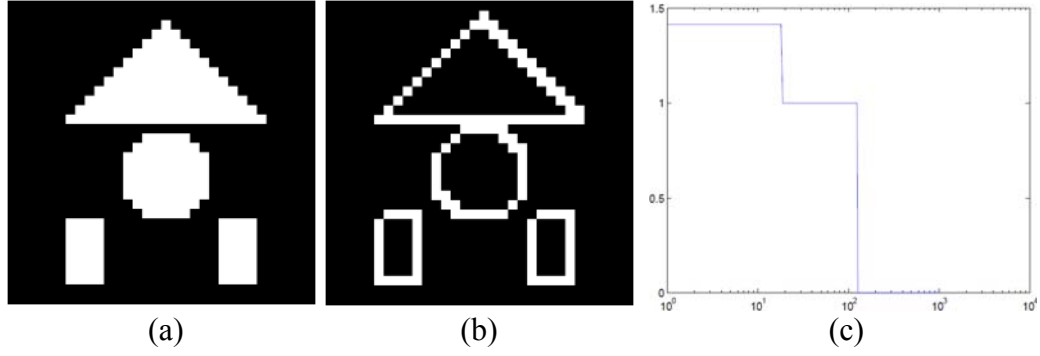


Fig. 5.1: A  $32 \times 32$  test image. (a) Original image. (b) Gradient magnitude image. It is 129-sparse. (c) Plot of the magnitude sorted coefficients in (b). Its  $l_1$ -norm is 133.

#### 5.4.1 *EI*: Comparison with Conventional Techniques

*EI* has two parts: The first one comprises the performance comparison of SOCP, FBP, and SART based on number of measurements. In the second part, the visual results are given for a certain number of measurements. As a consequence of the performance comparison, the quality of images with respect to the amount of X-ray radiation absorbed plus the reconstruction times with respect to the number of rays used in the experiment are given in Fig. 5.2 and Fig. 5.3, respectively. The relation (2.7) was benefited with unity proportionality constant to estimate the amount of absorption. Our main observations on Fig. 5.2 are: 1) As more X-rays are used to yield more measurements, all reconstruction algorithms provide better solutions at the expense of increased radiation absorption in general; 2) Given a certain amount of radiation absorbed, i.e., a fixed number of rays, higher PSNR values are obtained for images reconstructed by SOCP. However, we observed in Fig. 5.3 that the lowest reconstruction speed belongs to SOCP. Since increasing the number of measurements causes the problem size to enlarge, the solution comes to a conclusion in a long period of time after performing a lot of operations. On the other hand, the reason of the fluctuation in Fig. 5.3 when  $L$  is changed from 13 to 17 is that if the measurements are too many, less Newton iterations suffice to come to a solution rapidly in a given log-barrier iteration. For example, in our experiment, totally 76 and 49 Newton iterations took place, respectively, for  $m = 13 \times 32$  and

$17 \times 32$  measurements, until completing  $k_b = 8$  log-barrier iterations. In the latter case, additional Newton iterations do not provide significant decrements on the cost function. Therefore, it is allowed to exit from the Newton iterations earlier for time saving purpose. The total number of iterations realized in the first part of the experiment is given in Table 5.1. These recordings are consistent with the reconstruction times plotted in Fig. 5.3 such that both additional number of iterations and measurements cause the reconstruction time to increase. The Newton tolerance parameter,  $\varepsilon$  becomes the major factor on determining the number of Newton iterations required when the maximum allowable number,  $n_{nw}$ , is high. The values  $n_{nw} = 50$  and  $\varepsilon = 10^{-3}$  used in *EI* validated this fact.

Table 5.1: The total number of Newton iterations in SOCP

| $m (\times 32)$      | 5  | 7  | 9  | 11 | 13 | 17 |
|----------------------|----|----|----|----|----|----|
| number of iterations | 36 | 49 | 48 | 65 | 76 | 49 |

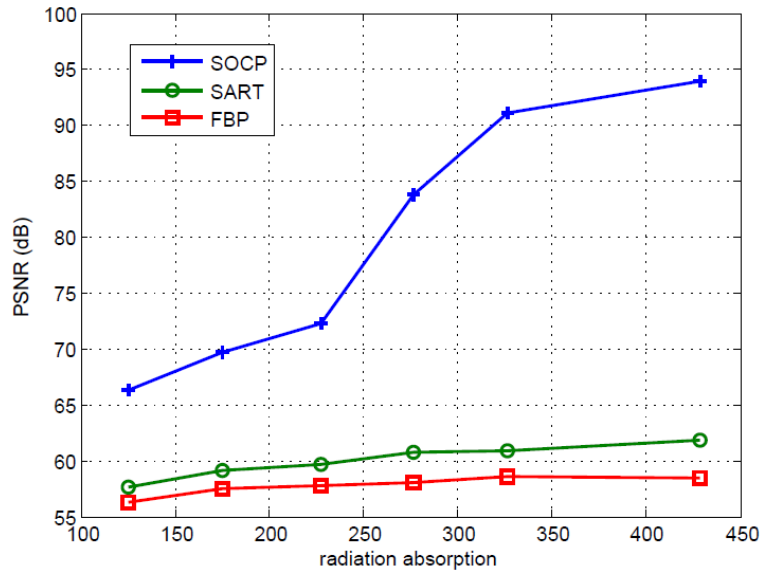


Fig. 5.2: Plot of PSNR versus radiation absorbed (SOCP, FBP, and SART). The test image shown in Fig. 5.1 is reconstructed using  $m = L$  views  $\times$  32 rays/view measurements for  $L = \{5, 7, 9, 11, 13, \text{ and } 17\}$ . While SART outer loop iterations is limited to 10, the maximum numbers of Newton and SYMMLQ iterations allowed in SOCP are fixed at 50 and 600, respectively.

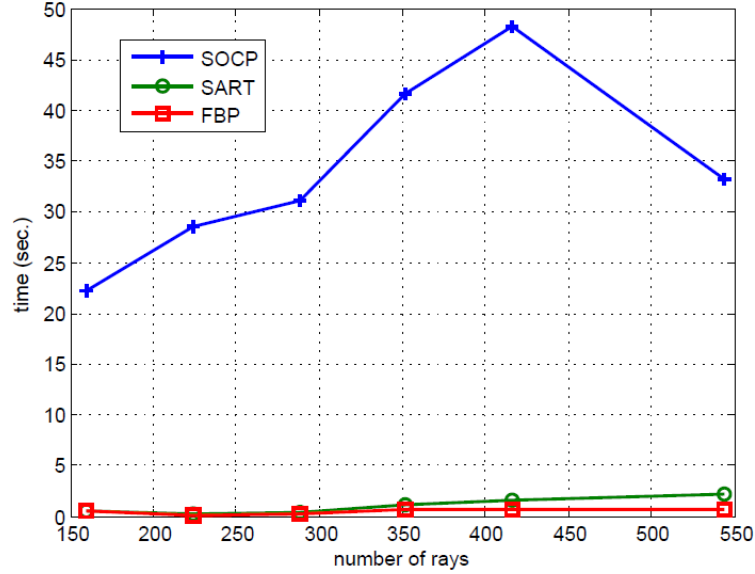


Fig. 5.3: Plot of reconstruction time versus number of rays (SOCP, FBP, and SART ( $k = 10$ )). The test image shown in Fig. 5.1 is reconstructed using  $m = L$  views  $\times$  32 rays/view measurements for  $L = \{5, 7, 9, 11, 13, \text{ and } 17\}$ . While SART outer loop iterations is limited to 10, the maximum numbers of Newton and SYMMLQ iterations allowed in SOCP are fixed at 50 and 600, respectively.

The test images reconstructed from  $m = 8$  views  $\times$  32 rays/view measurements in the second part of the experiment are shown in Fig. 5.4. While an almost perfect recovery is obtained via SOCP, FBP and SART solutions are not satisfactory. Although the solution of SOCP is obtained at the expense of a prolonged reconstruction time, neither FBP nor SART offers an almost perfect recovery in a moderate period of time. The performance of traditional techniques can be improved significantly only if a much larger data set is used. On the other hand, a high PSNR value ( $\sim 97$  dB) is attained for the recovery via SOCP after 68 Newton iterations in about 40 seconds. Although more iterations than recorded in  $m = 11 \times 32$  case are performed, less reconstruction time is required to get a better solution than the latter. Because the problem size is not very large in the former case, fewer operations were completed in a shorter period of time.

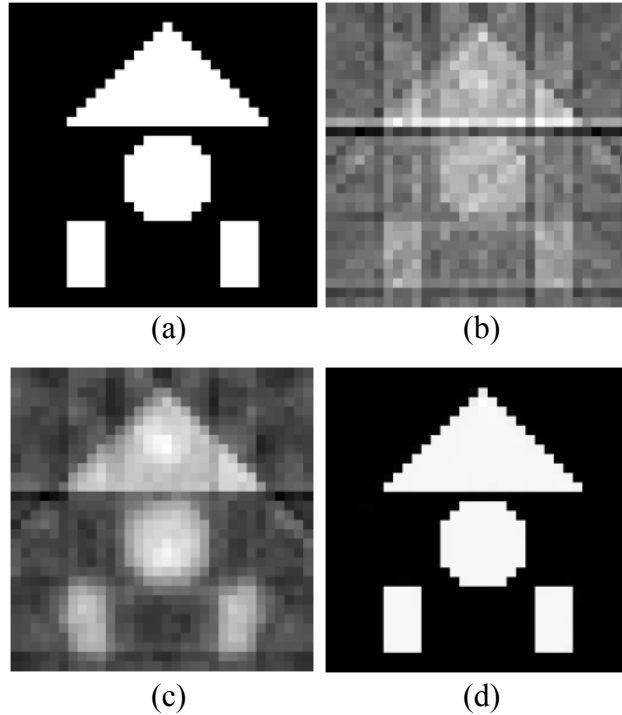


Fig. 5.4: Recoveries of the  $32 \times 32$  test image.  $m = 256$  measurements (8 views  $\times$  32 rays/view) obtained from equiangular (full) scanning of the test image are used for all reconstructions. (a) Original test image. (b) Image reconstructed by FBP, PSNR = 55.95 dB. (c) Image reconstructed by SART ( $k=10$ ), PSNR = 58.51 dB. (d) Image reconstructed by SOCP ( $c = 600$ ), PSNR = 97.84 dB.

#### 5.4.2 E2: Robustness Test in Large Scale Problems

A CS based solution may require the size of  $W$  matrix to be as large as  $20,000 \times 65,536$  to typically recover a  $256 \times 256$  image such as the head phantom shown in Fig. 3.3(a). The number of  $w_{ij}$ 's that is non-zero in a row of  $W$  can be up to 512, and therefore the total number of non-zero terms in  $W$  corresponds to a ratio of 1 to 128 with respect to the image size. Keeping only these non-zero terms and their locations allows deallocating 99% of the memory as compared to case of keeping every row element. In this regard, we recover the phantom image considering both noisy and noiseless measurements in E2. A zero mean white Gaussian noise with variance  $25 \times 10^{-6}$  is used to contaminate  $m = 22$  views  $\times$  256 rays/view measurements (SNR =  $\sim 77$  dB) obtained from equiangular (full) scanning of the phantom image. The reconstructed image via SOCP is shown in Fig. 5.5(d).



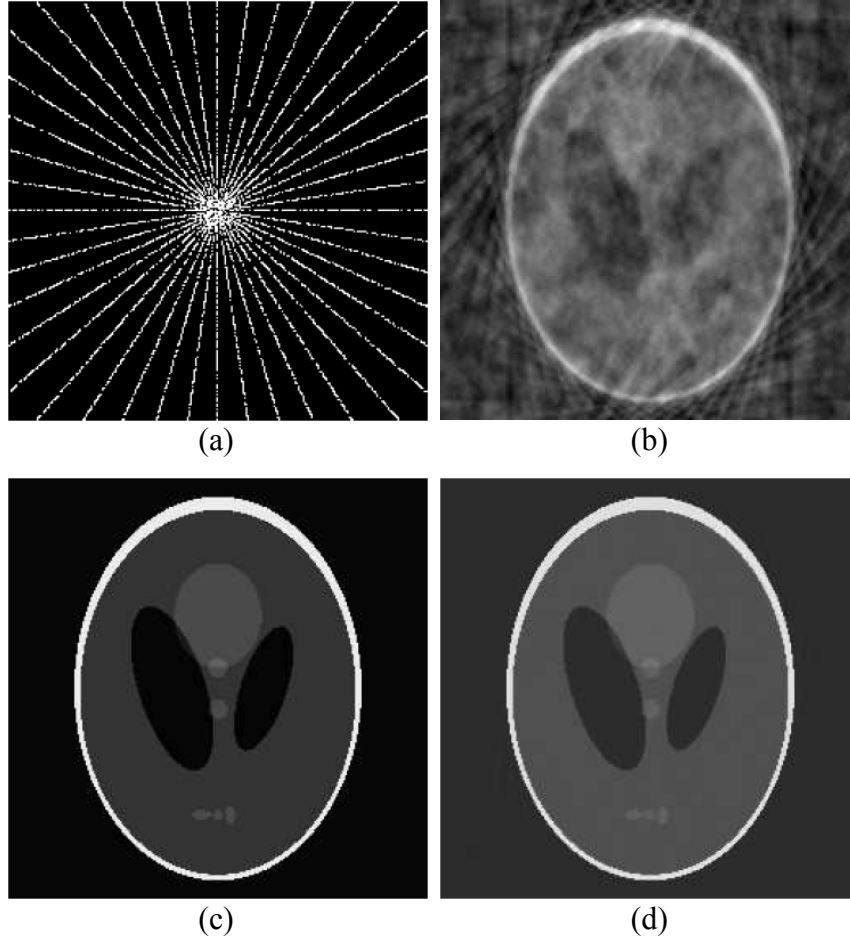


Fig. 5.5: Recoveries of the phantom image (SOCP and FT). (a) The sampling pattern of Fourier coefficients on 2-D Fourier space. The display area is  $[-\pi, \pi) \times [-\pi, \pi)$ . (b) Image reconstructed by inverse FT using Fourier coefficients in (a). PSNR = 65.66 dB. (c) Image reconstructed by SOCP using  $m = 5632$  measurements (22 views  $\times$  256 rays/view) from equiangular (full) scanning of the original image. PSNR = 101.6 dB. The number of SYMMLQ iterations is 5,000. (d) Image reconstructed by SOCP using  $m = 5632$  noisy measurements (22 views  $\times$  256 rays/view) from equiangular (full) scanning of the original image. PSNR = 85.56 dB. The noise pattern is additive Gaussian with  $\mathcal{N}(0, 25 \times 10^{-6})$  characteristics. The data fidelity relaxation parameter,  $\varepsilon$ , is set to  $5 \times 10^{-3}$ . The number of CG iterations is 10,000. The maximum number of Newton iterations allowed is fixed at 50 in both (c) and (d).

The noise-free solutions via SOCP and inverse FT are also given in Fig. 5.5. Although it is not feasible to get true Fourier coefficients of the original image, we exploit them to illustrate theoretically the best solution of FBP or SART. The Fourier coefficients are selected randomly on equally separated radial trajectories.

In fact, a better recovery than shown in Fig. 5.5(b) is possible by sorting the coefficients and then selecting the most significant ones. However, it would not be a fair comparison with CS based solutions since the measurements input to SOCP are not obtained using a special scanning pattern that are designed for providing significant information from the object. Under noisy circumstances, the reconstruction is performed using 10,000 CG iterations which is twice the number of SYMMLQ iterations in the noiseless case where  $c = 5000$  is sufficient to decrease the residue reasonably such as below the same predefined value, e.g., 0.5, set in both cases. Increasing the noise power, however, necessitates more CG iterations to help reducing the residue. Although the noise contamination causes the contrast resolution to decrease slightly as perceived in Fig. 5.5(c) and (d), the recovery from noisy measurements via SOCP still outweighs the noise free solution of the inverse Fourier transform. Considering spatial and contrast resolutions, the difference between the recoveries in Fig. 5.5(b) and (d) can be realized clearly. It is also remarkable that less reconstruction time is spent for recovery from noisy measurements although more CG iterations are required. In noisy situation, the problem size can be reduced more, and therefore, fewer operations are performed as explained in Section 5.3.

### 5.4.3 E3: Comparison with Other CS based Solutions

The solution of SOCP is compared with those of ASD-POCS, ASD-FT, and Davidon-Fletcher-Powell method (DFP). DFP is used for solving the following unconstrained reformulation of problem (4.6):

$$\text{UP: } \min_x \left[ \lambda \cdot \|x\|_{\text{TV}} + (1 - \lambda) \cdot \|Wx - P\|_2 \right] \quad (5.11)$$

where  $0 < \lambda < 1$  regulates the cost function such that depending on its value UP may turn out to be the minimization of either the TV-norm or the Euclidian norm of the residue completely. Employing the cubic interpolation method in its line search step, DFP is implemented with  $\lambda = 0.15$ . The implementations of ASD-POCS and ASD-FT were performed as described in Methods III and IV, respectively. Exceptionally, the true Fourier coefficients which have been computed analytically

once from the original image are used in place of the coefficients of the estimated images. Therefore, we are able to run ASD-FT at its best performance theoretically. The parameters set in both ASD-POCS and ASD-FT are given in Table 5.2. In Method V,  $r = 5$  is used to scale  $\tau$  at every logarithmic barrier iteration.

Table 5.2: Parameters set in ASD-POCS and ASD-FT.

| $\lambda_{art}$ | $\mathbf{r}_{art}$ | $\mathbf{r}_{asd}$ | $\mathbf{r}_{max}$ | $\mathbf{r}^*$ | $\epsilon$ |
|-----------------|--------------------|--------------------|--------------------|----------------|------------|
| 1.0             | 0.995              | 0.95               | 0.95               | 0.2            | 0.1        |

\*  $r$  is set to 0.02 for ASD-FT in  $E3$ .

The  $32 \times 32$  test image is reconstructed by each algorithm using the same  $m = 256$  measurements ( $8 \text{ views} \times 32 \text{ rays/view}$ ) obtained from equiangular (half) scanning of the image. The PSNRs of images estimated at every outer loop iteration are computed and time spent until then is recorded for each algorithm. Figs. 5.6-5.9 show the PSNRs and the cumulative times with respect to the number of iterations together. The information given in these figures is combined in Fig 5.10 where instead of iteration numbers the plots of PSNRs versus cumulative times are shown all together. According to Figs. 5.6 and 5.9, both SOCP and DFP converge to a better solution faster than ASD-POCS shown in Fig. 5.7. On the other hand, the analytic computation of the true Fourier coefficients allows better PSNR in a less period of time for the ASD-FT algorithm.

The CS based solutions including our proposed scheme are efficacious in recovering from few projection data over the traditional methods. Essentially, reformulating the original problem as an unconstrained optimization problem allows having more accurate recoveries in a short time. In particular, the solution of the SOCP problem and the UP in (5.11) results in more qualified estimations at any moment during the reconstruction period. Instances of poor performance of the proposed scheme and the DFP method are observed for large-scale problems. Huge matrix vector multiplications and estimations of large Hessian matrices prolong the processing time and allocate a large memory space.

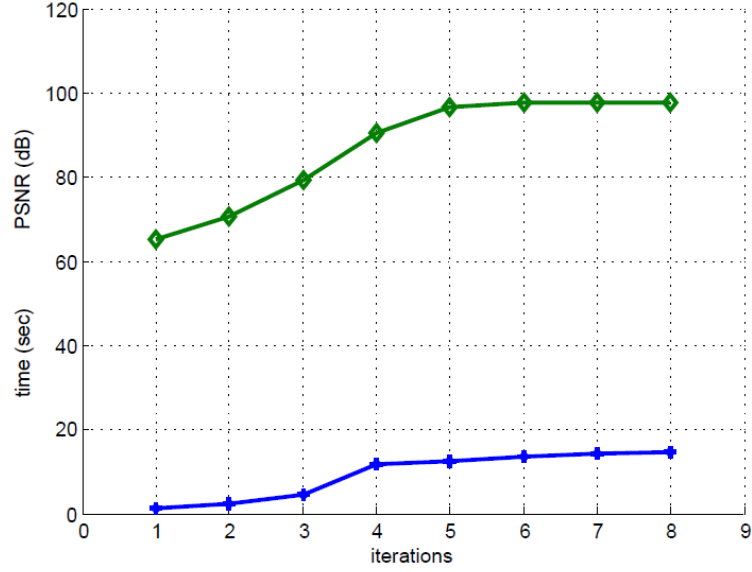


Fig. 5.6: PSNR and time recordings in iterations of SOCP ( $c = 600$ ,  $n_{nw} = 50$ ). The upper (green) line shows the PSNR versus number of iterations. The lower (blue) line shows cumulative reconstruction times versus number of iterations.  $m = 256$  measurements ( $8$  views  $\times$   $32$  rays/view) obtained from equiangular (half) scanning of the test image are used in the reconstruction.

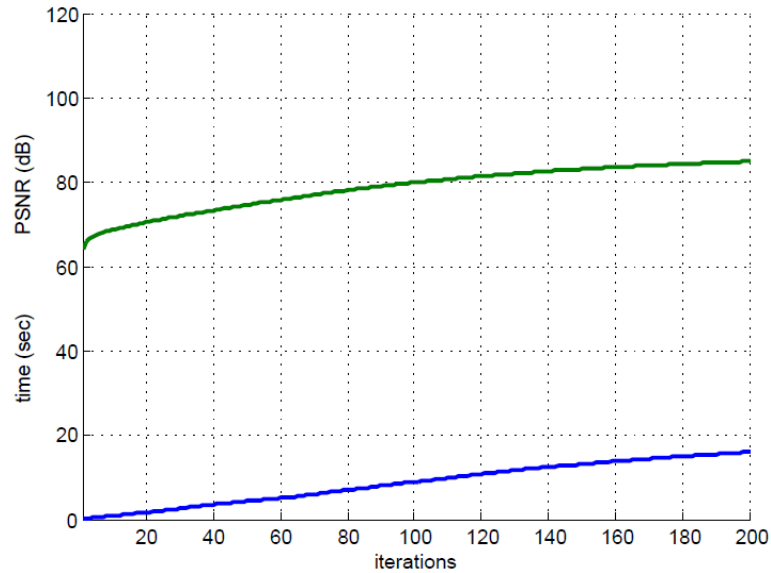


Fig. 5.7: PSNR and time recordings in iterations of ASD-POCS ( $k_p = 200$ ,  $n_{sd} = 20$ ). The upper (green) line shows the PSNR versus number of iterations. The lower (blue) line shows cumulative reconstruction times versus number of iterations.  $m = 256$  measurements ( $8$  views  $\times$   $32$  rays/view) obtained from equiangular (half) scanning of the test image are used in the reconstruction.

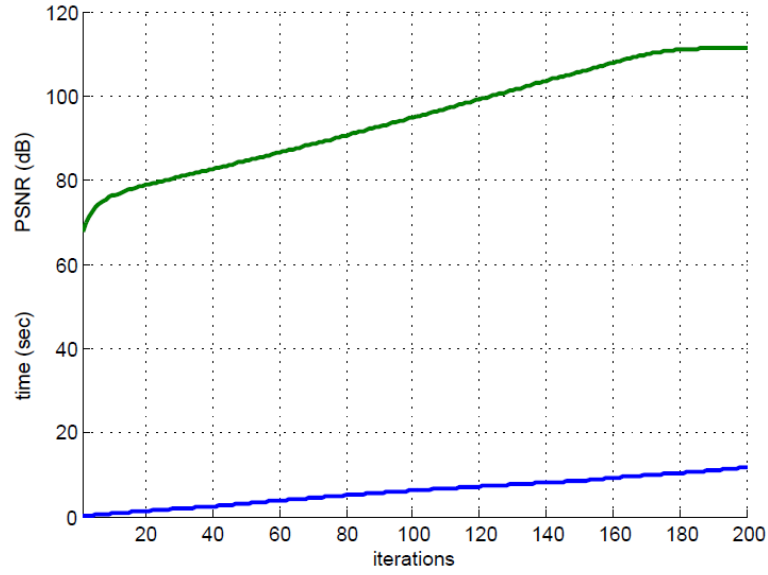


Fig. 5.8: PSNR and time recordings in iterations of ASD-FT ( $k_f = 200$ ,  $n_{sd} = 20$ ). The upper (green) line shows the PSNR versus number of iterations. The lower (blue) line shows cumulative reconstruction times versus number of iterations.  $m = 256$  measurements ( $8 \text{ views} \times 32 \text{ rays/view}$ ) obtained from equiangular (half) scanning of the test image are used in the reconstruction.

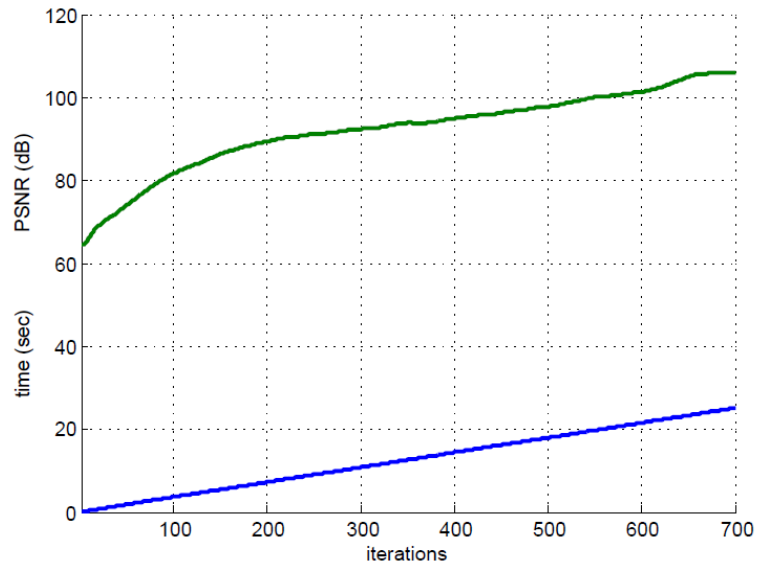


Fig. 5.9: PSNR and time recordings in iterations of DFP. The upper (green) line shows the PSNR versus number of iterations. The lower (blue) line shows cumulative reconstruction times versus number of iterations.  $m = 256$  measurements ( $8 \text{ views} \times 32 \text{ rays/view}$ ) obtained from equiangular (half) scanning of the test image are used in the reconstruction.

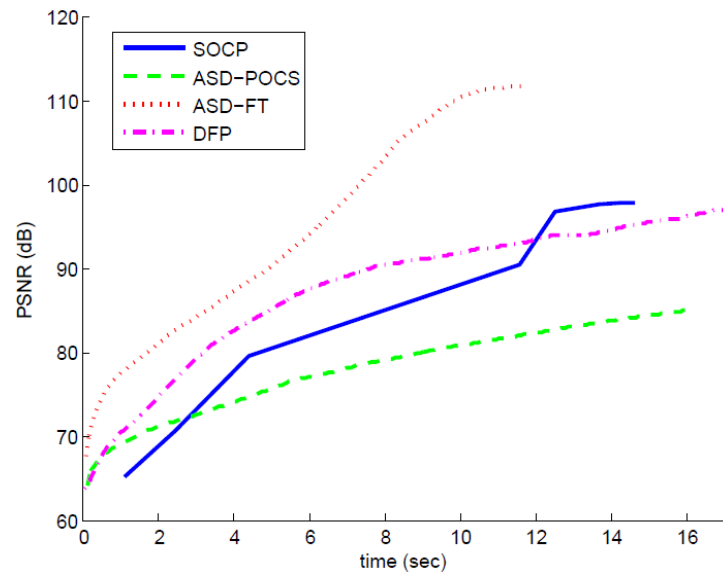


Fig. 5.10: Performance comparison of SOCP with other CS based solutions. It is a combination of all plots in Figs. 5.6-5.9.

## CHAPTER 6

### FAST TOTAL VARIATION MINIMIZATION

In Chapter 5, it has been shown that the logarithmic barrier and DFP methods that solve the SOCP problem and the UP, respectively, outweigh the POCS based solutions especially in small-scale problems. Although FT based solutions seem to be superior to all in numerical experiments, having true Fourier coefficients is infeasible in practice and using estimated values are prone to poorer recoveries than offered by the unconstrained problem solvers. In this chapter, we address the issue of solving large-scale problems in less period of time. For this reason, the original problem is reformulated as an unconstrained problem and solved via a CG-based algorithm. The proposed scheme does not require handling large Hessian matrices or intermediate parameters that are faced with in the DFP or logarithmic barrier methods. Besides, the value of the regularization parameter that is proposed in the unconstrained problem definition is determined reasonably. Therefore, instead of using a suboptimal value as in the DFP method, a generic solution to image reconstruction problems is obtained.

#### 6.1 Problem Reformulation

The solution  $\hat{x}$  to problem (4.6) can be obtained by

$$\hat{x} = \min_x f(x) \quad (6.1)$$

where

$$f(x) = \lambda \|x\|_{\text{TV}} + \frac{(1-\lambda)}{2} \|Wx - P\|_2^2 \quad (6.2)$$

The regularization parameter  $0 < \lambda < 1$  linearly combines the two functions: the TV-norm,  $TV(x)$ , and the residue-norm square,  $RS(x)$ . Specifically,

$$TV(x) = \|x\|_{TV} \quad (6.3)$$

$$RS(x) = 0.5\|Wx - P\|_2^2 \quad (6.4)$$

Contrary to  $RS(x)$ ,  $TV(x)$  is neither strictly convex nor differentiable everywhere. Accordingly, the objective function  $f(x)$  is convex, but not strictly so, and differentiable except where the  $TV(x)$  is non-smooth. The three functions are shown in Fig. 6.1 where different values of  $\lambda$  reshape  $f(x)$ , allowing it to look like more to one of its functional components. Because the descent direction over the surface of  $f(x)$  changes based on  $\lambda$  selection, it is important to make a proper selection for convergence to the true solution rapidly. Later, we will explain exactly how the weighting of  $TV(x)$  and  $RS(x)$  should be considered reasonably while strengthening the data fidelity ( $Wx=P$ ) and minimizing the total variation.

Problem (6.1) can be solved iteratively by a variety of unconstrained optimization methods. For example, the Davidon-Fletcher-Powell method converges faster to a better solution than that of ASD-POCS, but it is only usable for small-scale problems [62]. The necessity of computing large Hessian updates is a common difficulty met in such quasi-Newton methods. The steepest-descent method, on the other hand, is easy to implement. However, its lower convergence rate constitutes the major adversity of gradient descent methods. Having a much quicker convergence than that of the steepest-descent method, the CG method seems to be useful for large scale problems such as (6.1) where it may not be feasible to run even  $N$  iterations. Although the conjugacy gets lost during the execution because of the accumulated floating point round-off errors, the lack of an algorithm to solve (6.1) exactly brings the CG method still forward to be benefited from its rapid convergence. CG is effective for solving systems of the form,  $Hx=h$ , where  $H$  is a square matrix. The solution is equivalent to minimizing the quadratic function of the form,

$$\frac{1}{2}x^T Hx - h^T x + b \quad (6.5)$$



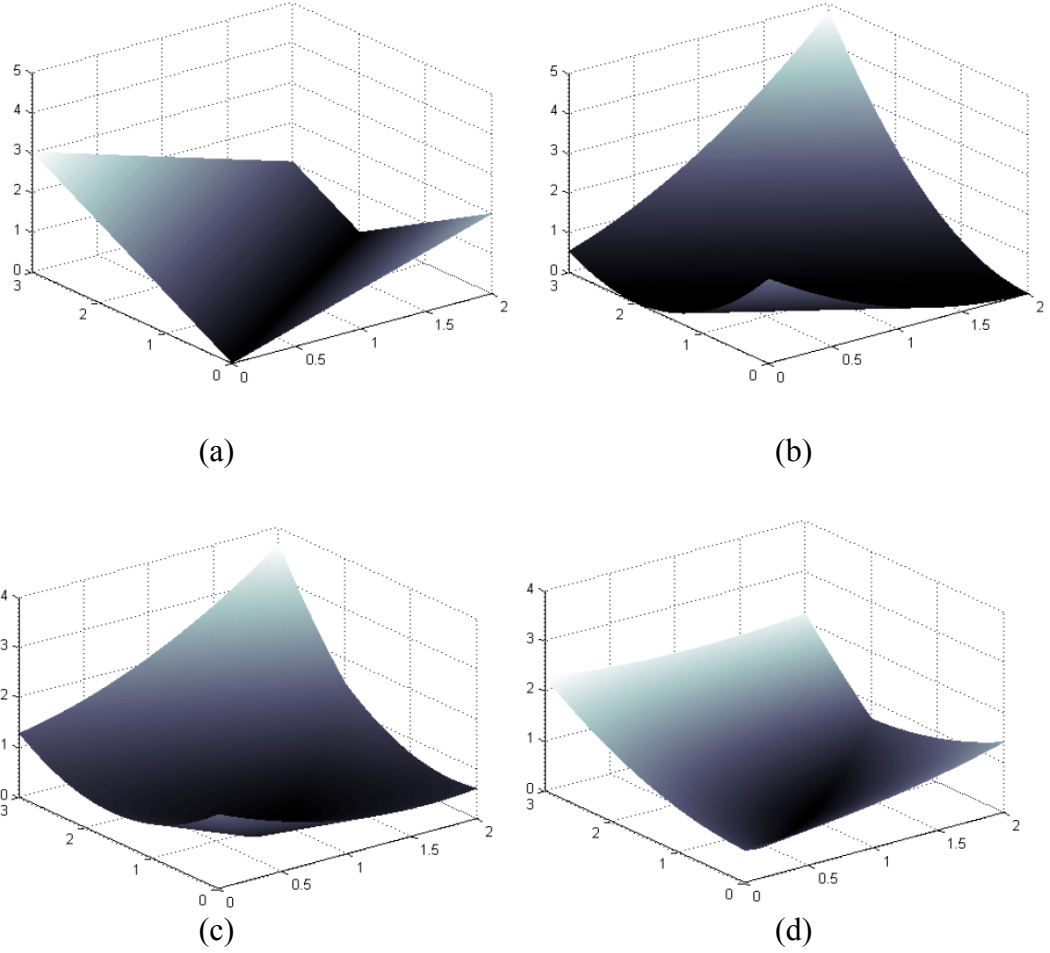


Fig. 6.1: 3-D illustration of  $TV(x)$ ,  $RS(x)$  and  $f(x)$ . (a)  $TV(x)$ , (b)  $RS(x)$  with  $W = (1/4) \times [\sqrt{17} \ \sqrt{17}]$  and  $P = (1/2) \times \sqrt{17}$ . (c)  $f(x)$  with  $\lambda = 0.3$ . (d)  $f(x)$  with  $\lambda = 0.7$ . In all plots, the elements of  $x \in \mathbf{R}^2$  take values on intervals  $[0,3]$  and  $[0,2]$ , respectively, on the two axes. Notice that  $TV(x)$  has two planar surfaces and  $RS(x)$  has parabolic cross-sections.  $TV(x)$  has zero values where  $x$ 's elements are equal ( $x_1=x_2$ ).  $RS(x)$  has zero values where the sum of  $x$ 's elements are two ( $x_1+x_2=2$ ). The weighted sum of  $TV(x)$  and  $RS(x)$  more resembles either of them depending on the weighting factor. The minimum value of  $f(x)$  is positioned at  $x = [1 \ 1]^T$  in (c) and (d).

since its gradient,

$$\frac{1}{2} H^T x + \frac{1}{2} Hx - h \quad (6.6)$$

can be reduced to  $Hx=h$  when  $H$  is symmetric. Therefore, the solution to  $Hx=h$  is a critical point of the quadratic function (6.5). The solution is the minimum if  $H$  is positive-definite at the same time. Likewise, it is possible to minimize  $f(x)$

effectively using the CG method after defining a reasonable quadratic approximation.

## 6.2 Quadratic Approximation

Since  $RS(x)$  is already quadratic, expressing  $TV(x)$  in a quadratic form is sufficient to define a quadratic approximation for  $f(x)$ . Assuming the entries of  $x$  are not the same, i.e.,  $TV(x) \neq 0$ , the TV-norm can be expressed by

$$x^T D^T \Sigma D x \quad (6.7)$$

where  $\Sigma$  is a diagonal and  $D$  is a composite difference operator matrix. The proof that  $D^T \Sigma D$  is both symmetric and positive-definite follows from the definitions at (5.7):

$$\|D_j x\|_2 = \sqrt{(D_{hj}x)^2 + (D_{vj}x)^2} = \frac{(D_{hj}x)^2 + (D_{vj}x)^2}{\|D_j x\|_2} \quad (6.8)$$

and

$$\|x\|_{TV} = \sum_j \|D_j x\|_2, \quad j = 1, 2, \dots, N. \quad (6.9)$$

Using (6.8) and rewriting  $\|x\|_{TV}$  explicitly for all  $j$ :

$$\begin{aligned} \|x\|_{TV} &= \frac{x^T D_{h1}^T D_{h1} x + x^T D_{v1}^T D_{v1} x}{\|D_1 x\|_2} + \dots + \frac{x^T D_{hN}^T D_{hN} x + x^T D_{vN}^T D_{vN} x}{\|D_N x\|_2} \\ &= \frac{x^T D_{h1}^T D_{h1} x}{\|D_1 x\|_2} + \dots + \frac{x^T D_{hN}^T D_{hN} x}{\|D_N x\|_2} + \frac{x^T D_{v1}^T D_{v1} x}{\|D_1 x\|_2} + \dots + \frac{x^T D_{vN}^T D_{vN} x}{\|D_N x\|_2} \\ &= \begin{bmatrix} D_{h1} x \\ \vdots \\ D_{hN} x \end{bmatrix}^T \begin{bmatrix} D_{h1} x / \|D_1 x\|_2 \\ \vdots \\ D_{hN} x / \|D_N x\|_2 \end{bmatrix} + \begin{bmatrix} D_{v1} x \\ \vdots \\ D_{vN} x \end{bmatrix}^T \begin{bmatrix} D_{v1} x / \|D_1 x\|_2 \\ \vdots \\ D_{vN} x / \|D_N x\|_2 \end{bmatrix} \end{aligned} \quad (6.10)$$

Let  $D_h$  and  $D_v$  be horizontal and vertical difference operator matrices, respectively and  $\Sigma_{Dx}$  be the diagonal matrix with entries  $1/\|D_j x\|_2$ ,  $j = 1, 2, \dots, N$ .

$$D_h = \begin{bmatrix} D_{h1} \\ \vdots \\ D_{hN} \end{bmatrix}, \quad D_v = \begin{bmatrix} D_{v1} \\ \vdots \\ D_{vN} \end{bmatrix} \quad \text{and} \quad \Sigma_{Dx} = \text{diag} \left( \frac{1}{\|D_j x\|_2} \right) \quad (6.11)$$

Then, the expression (6.10) ends up with

$$\|x\|_{TV} = x^T D_h^T \Sigma_{Dx} D_h x + x^T D_v^T \Sigma_{Dx} D_v x \quad (6.12)$$

$$\begin{aligned} &= x^T \begin{bmatrix} D_h \\ D_v \end{bmatrix}^T \begin{bmatrix} \Sigma_{Dx} & 0 \\ 0 & \Sigma_{Dx} \end{bmatrix} \begin{bmatrix} D_h \\ D_v \end{bmatrix} x \\ &= x^T D^T \Sigma D x \end{aligned} \quad (6.13)$$

where it is clear that

$$D = \begin{bmatrix} D_h \\ D_v \end{bmatrix} \quad \text{and} \quad \Sigma = \begin{bmatrix} \Sigma_{Dx} & 0 \\ 0 & \Sigma_{Dx} \end{bmatrix} \quad (6.14)$$

The equations starting from (6.9) and leading to (6.13) prove the expression (6.7) to be a quadratic function under the assumption  $TV(x) \neq 0$ . Clearly,  $D^T \Sigma D$  is symmetric since  $\Sigma$  is diagonal. It is also positive-definite because, by definition, the TV-norm is always positive for any  $x$ . Thus, the proof is complete.

$RS(x)$  can be expressed explicitly by

$$\frac{1}{2} (x^T W^T W x - 2x^T W^T P + P^T P). \quad (6.15)$$

Using (6.7) and (6.15),  $f(x)$  is written in quadratic form likewise (6.5) with the analogy that

$$H = 2\lambda D^T \Sigma D + (1 - \lambda) W^T W \quad (6.16)$$

$$h = (1 - \lambda) W^T P \quad (6.17)$$

$$b = \frac{(1 - \lambda)}{2} P^T P \quad (6.18)$$

where offset  $b$  has no importance for the solution.  $(1/2)x^T Hx - h^T x + b$  is an approximation to  $f(x)$  since  $\Sigma$  and hence  $H$  is  $x$ -dependent. It is possible to minimize  $f(x)$  iteratively at successive approximation points based on a CG algorithm, which is explained in detail in Section 6.3.

### 6.3 Conjugate Gradient Based Algorithm

Suppose  $\Sigma = \Sigma_0$  is computed for a certain value of  $x = x_0$ , and  $H$  is computed using  $\Sigma_0$ . The solution to  $Hx = h$  minimizes the quadratic approximation at point  $x_0$  and so does  $f(x)$ . A new approximation for  $f(x)$  is defined at the current solution and its minimum is sought again. The minimization of approximations is a repeated procedure until satisfying a little residue norm. The steps of the solution algorithm are summarized in Method VI.

---

**Method VI:** Pseudo code for CG-based algorithm.

---

```

1   initialize  $\lambda, k_0, \varepsilon_0, x$ 
2    $h \leftarrow$  compute  $h$  using (6.17)
3   repeat for index  $k \leftarrow 1$  to  $k_0$  or until  $\|Hx - h\|_2 / \|h\|_2 < \varepsilon_0$ 
4    $H \leftarrow$  compute  $H$  using (6.16)
5    $x \leftarrow$  compute CG to solve  $Hx = h$ 
6   end

```

---

A great majority of the processing time is spent while running the CG algorithm at line 4. It is detailed in Method VI(a) for the sake of completeness. The parameters  $r$ ,  $d$ , and  $\alpha$  keep the usual residue, conjugate-gradient-direction and step-size, respectively. Both  $r$  and  $d$  are set to negative of the gradient,  $h - Hx$ , initially at line 2 and updated at lines 8 and 9, respectively. A fast recursive computation of the residue,  $r - \alpha Hd$ , is replaced by recalculation of the exact value,  $h - Hx$ , at every  $\sqrt{N}$  CG iteration to remove the accumulated floating point errors.  $\delta$  is used as a placeholder parameter to compute the ratio of the residue-norm square before and after its update at line 8. The residue decrement is not guaranteed in a CG iteration. Therefore,  $x$  values computed only in iterations where a (residue) decrement occurs are subject to return. The output parameter  $x'$  at line 10 keeps the final  $x$  value saved in occurrences of such decrements. CG iterations are ceased if the maximum number of iterations,  $k_c$ , is completed or the final residue-norm is smaller than  $\varepsilon_c$ .

fraction (usually  $\leq 1$ ) of the initial value,  $\sqrt{\delta_0}$ . The implementation can be optimized reusing previously computed  $r^T r$  and  $Hd$  values in following lines, e.g.,  $r^T r$  at lines 6, 10, or  $Hd$  at line 8.

---

**Method VI(a):** Pseudo code for CG algorithm.

---

```

1   initialize  $k_c, \varepsilon_c$ 
2    $(d, r) \leftarrow h - Hx$ 
3    $\delta_0 \leftarrow r^T r$ 
4   repeat for index  $k_c \leftarrow 1$  to  $k_c$  or until  $\|r\|_2 / \sqrt{\delta_0} < \varepsilon_c$ 
5    $\delta \leftarrow r^T r$ 
6    $\alpha \leftarrow r^T r / d^T Hd$ 
7    $x \leftarrow x + \alpha d$ 
8    $r \leftarrow \begin{cases} r - Hx & \text{if } k \bmod \sqrt{N} = 0, \\ r - \alpha Hd & \text{otherwise} \end{cases}$ 
9    $d \leftarrow r + (r^T r / \delta)d$ 
10   $x' \leftarrow x$  if  $r^T r < \delta$ 
11  end

```

---

Turning briefly away from the CG algorithm, there is no need of forming  $H$  explicitly at line 4 in Method VI. In fact,  $\Sigma$  is updated using  $x'$ , and all  $Hx$  and  $Hd$  computations in Method VI are implemented by sequential matrix vector multiplications according to (6.16). The matrices  $W$ ,  $D$  and  $\Sigma$  are not kept entirely in memory. Since they are highly sparse, only the non-zero entries and their locations are kept. The execution speed of the CG algorithm can be increased further by subtracting the elements of a vector  $z$  involved in a  $Dz$  multiplication instead of performing the matrix vector multiplication directly. For example, the row vector  $D_{v,l}$  in (6.11) is  $[-1, 1, 0, \dots, 0]$  according to definition (5.7) and calculating  $D_{v,l}z$  is equivalent to the subtraction,  $z_2 - z_1$ . If direct matrix vector multiplications are preferred, it is possible to simplify the implementation by working with smaller matrices  $D_h$ ,  $D_v$ , and  $\Sigma_{Dx}$  rather than  $D$  and  $\Sigma$  in  $\mathbf{R}^{2N \times N}$ . The CG-based algorithm has an operational complexity of  $O(k_o k_c N^2)$ . The stop condition when the relative residue norm is smaller than  $\varepsilon_o \ll 1$  is usually determined by the maximum number of outer loops,  $k_o$ , which is comparable with  $k_b$  in SOCP. The number of CG iterations, on the other hand, is limited by  $\varepsilon_c \approx 1$  in practice. The setting of  $\varepsilon_c$  close to 1 is reasonable because stopping the CG iterations earlier than  $k_c \approx c$  (the number of CG iterations in SOCP) allows  $\Sigma$  to be updated frequently, resulting in better approximations for  $f(x)$ . These early stops usually keep  $k_c$  below  $\log_2 N$  and

therefore make the CG-based algorithm quite faster than SOCP. It is effective especially when we are far away from the solution. The latency time to get fewer residues, however, prolongs nearby the solution where the CG-based algorithm may be replaced completely by the steepest-descent method with a small, constant step-size. That the conjugate directions lead to the minimum point rapidly over a better regulated  $f(x)$  is also possible by tuning  $\lambda$ , which is the subject of the next section.

#### 6.4 Regularization Parameter

Consider the original constraint  $Wx=P$  in problem (4.6). All points satisfying  $Wx=P$  are also solutions to  $RS(x)=0$ . Therefore, the original problem can be reformulated as

$$\min_x \|x\|_{TV} \quad \text{subject to} \quad \frac{1}{2} \|Wx - P\|_2^2 = 0 \quad (6.19)$$

The constraint minima of  $\|x\|_{TV}$  is a critical point of the Lagrange function,

$$\Lambda(x, \tau) = TV(x) + \tau \cdot RS(x) \quad (6.20)$$

where the Lagrange multiplier  $\tau \in \mathbf{R}$  is a scalar. Using a single constraint in (6.19) instead of  $Wx-P=0$  allows solving a reduced system of  $N+1$  equations derived from setting the partial derivatives of  $\Lambda$  to zero:

$$\frac{\partial \Lambda}{\partial x} = 0, \quad \frac{\partial \Lambda}{\partial \tau} = 0, \quad (6.21)$$

or equivalently,

$$\nabla TV(x) + \tau W^T (Wx - P) = 0 \quad (6.22)$$

$$\|Wx - P\|_2^2 = 0 \quad (6.23)$$

where  $\nabla$  is the  $x$ -gradient operator. The nonlinear system defined by (6.22)-(6.23) can be solved for  $(x, \tau)$  using iterative techniques. Alternatively, a solution for  $\tau$  can be inferred by multiplying (6.22) with  $x^T$  from the left side:

$$x^T \nabla TV(x) + \tau x^T W^T (Wx - P) = 0 \quad (6.24)$$

Using the relation  $x^T \nabla TV(x) = TV(x)$ ,

$$\tau = \frac{-TV(x)}{(Wx)^T (Wx - P)} \quad (6.25)$$

where  $\tau$  is to be calculated only for  $x$  values satisfying (6.23). As  $x$  approaches any vector  $x''$  in the solution set,  $Wx''$  gets closer to  $P$ , and  $\tau$  goes to infinity provided that  $TV(x'') \neq 0$ . Among critical points  $(x'', \infty)$ , the desired  $x''$  is the one that provides the minimum  $TV$ . On the other side, equation (6.22) can be solved for  $x$  by replacing values of  $\tau$  right on the solution. However, an infinite value makes the expression unstable and the equation irresolvable, causing us to stay alone with (6.23) again. Thus situated, accessing all possible solutions of (6.23), without considering its feasibility, makes the actual value of  $\tau$  insignificant.

Although  $f$  is declared in (6.2) as a function of  $x$  only, the right expression is

$$f(x, \lambda) = \lambda TV(x) + (1 - \lambda)RS(x) \quad (6.26)$$

and its minimization with respect to  $x$  and  $\lambda$  should be considered together for converging to the solution of (4.6). Instead of solving two-argument minimization of (6.26), one can benefit from interpretations of the method of Lagrange multipliers above. An analogy between  $\Lambda$  and  $f$  is established by setting  $\tau = \lambda^{-1}(1-\lambda)$ , ( $\tau = \infty$  is equivalent to  $\lambda=0$ ). Since  $f(x, \lambda)$  is an approximately quadratic function,  $f(x'', 0)=0$  is the minimum. Replacing  $\lambda=0$  in advance on (6.26) is useless, because there are infinitely many solutions of  $RS(x)=0$ , and among them it is infeasible to seek an  $x''$  that minimizes  $TV(x)$ .  $\lambda$  is actually desired to act as the Lagrange multiplier right on the solution only. No matter what the initial value of  $\lambda$  is, it should decay towards zero as  $x$  gets closer to  $x''$ . The CG-based algorithm in Method V is based on a fixed regularization parameter which is assumed to be suboptimal. In practice, this suboptimal value is decided based on satisfactory estimations after running the algorithm with different  $\lambda$  values. Too small or large values of  $\lambda$  may cause oscillations over the valley of  $RS(x)$  or at the vertex of  $TV(x)$  in noisy situations.

A reasonable initialization of the regularization parameter and its updates as analogous to the steepest-descent step-size adaptation in ASD-POCS are given by the fast TV-minimization algorithm (FTV) in Method VII.

---

**Method VII:** Pseudo code for FTV.

---

```

1   initialize  $\tau_{\min}, \tau_{\max}, k_o, r, \varepsilon_d$ 
2    $x \leftarrow$  compute CG to solve  $RS(x)=0$ 
3    $\lambda \leftarrow (1+\tau_{\min})^{-1}$ 
4    $(tv_0, rs_0) \leftarrow (TV(x), RS(x))$ 
5   repeat for index  $k \leftarrow 1$  to  $k_o$ 
6    $h \leftarrow$  compute  $h$  using (6.17)
7    $H \leftarrow$  compute  $H$  using (6.16)
8    $x_0 \leftarrow x$ 
9    $x \leftarrow$  compute CG to solve  $Hx=h$ 
10   $d_{tv} \leftarrow |TV(x_0) - TV(x)|$ 
11   $d_{rs} \leftarrow |RS(x_0) - RS(x)|$ 
12  return  $x$  if  $(d_{tv}/tv_0) < \varepsilon_d$  and  $(d_{rs}/rs_0) < \varepsilon_d$ 
13   $\lambda \leftarrow$  median  $\{(1+\tau_{\max})^{-1}, r \cdot \lambda, (1+\tau_{\min})^{-1}\}$ 
14  end

```

---

Having the same spirit with the CG-based algorithm, FTV differs only in insertion of the required steps into Method V to handle dynamic  $\lambda$ . In system configuration,  $\tau_{\min}$  and  $\tau_{\max}$  are defined at line 1 to limit the value of regularization parameter,

$$\frac{1}{1 + \tau_{\max}} \leq \lambda \leq \frac{1}{1 + \tau_{\min}} \quad (6.27)$$

so that oscillations are avoided. Considering the initial point as a solution of  $RS(x)=0$ , the initialization of  $\lambda$  with the upper bound value  $(1+\tau_{\min})^{-1}$  at line 3 weights  $TV(x)$  more compared to  $RS(x)$ . Thus, the decrement in  $f$  after the first iteration is contributed primarily by  $TV(x)$ . In fact, it is the only contributor because the value of  $RS(x)$  increases at the new point. Clearly, the CG algorithm at line 8 ensures a decrement in  $f$  but not necessarily in both functional components. This occurs seldom following an iteration in which the current estimate minimizes only one of the functional components. The variable  $x_0$  is used as a placeholder parameter to compute changes in  $TV(x)$  and  $RS(x)$  at lines 10 and 11. The additional exit condition at line 12 allows FTV to stop earlier than the CG-based algorithm



where the number of main loops is dominated by  $k_o$  only. The exit criterion is based on changes in functional components relative to their initial values computed at line 4. When both relative changes fall below  $\varepsilon_d \ll 1$ , the current estimate is considered to be sufficiently close to the minimum TV solution. The usage of  $\varepsilon_o$  introduced in Method VI is not required any more in FTV, because  $\varepsilon_d$  participates in handling the exit condition.  $\lambda$  is updated by  $r$ ;  $r$  is less than 1 but close to unity. At line 13 where too small values exceeding the lower bound are prohibited as well. Starting with a moderate value by configuring  $\tau_{\min}=1$ , as  $\lambda$  decays in successive iterations, the conjugate directions drift more towards the direction of  $-\nabla RS(x)$ .

Although additional steps increase the number of operations in FTV, the complexity remains the same with the CG-based algorithm. The convergence speed is even accelerated stably with the way  $\lambda$  is updated. It is remarkable that our initial assumption  $TV(x) \neq 0$  can be verified in almost all practices. Even with all flat images, the floating point round-off errors cause nonzero estimates in FTV iterations. Moreover, the setting  $\|D_j x\|_2 = \varepsilon$  (a small, constant positive value) in occasions of  $\|D_j x\|_2 = 0$  eases computations of  $\Sigma$  without bothering the convergence. Another important detail about the implementation is the way of constructing pixel difference operators on boundaries. The mirror imaging of the signal of interest results in zero valued  $D_{hj}x$  and  $D_{vj}x$  on horizontal and vertical ends, and  $D_N x = 0$  for sure. Considering  $x$  as a periodic signal rather than its mirror imaging avoids zero occurrences and therefore relieves the implementation.

## 6.5 Experimental Results

Numerical studies are performed in four experiments to validate FTV and demonstrate its performance. Experiments are tagged with  $EX$  where  $X$  denotes the experiment number 1 to 5. The standard  $256 \times 256$  Shepp-Logan phantom image shown in Fig. 3.3(a) is taken as true object in all experiments except  $E2$  and  $E4$  where a real cranial CT image shown in Fig. 2.2(a) is used. The latter is hosted in [www.flickr.com](http://www.flickr.com) and can be accessed from different medical sites as well. Neither the Shepp-Logan phantom image nor the cranial CT image has sparse object function but their GMIs shown in Fig. 6.2. The number of zero terms owns a ratio

of 42% in the cranial CT image and 97% in the Shepp-Logan phantom image. Assuming roughly 25% of the display area in Fig. 6.2(a) and (b) correspond to the exterior of actual objects, the GMI of cranial CT image itself can reasonably be considered non-sparse.

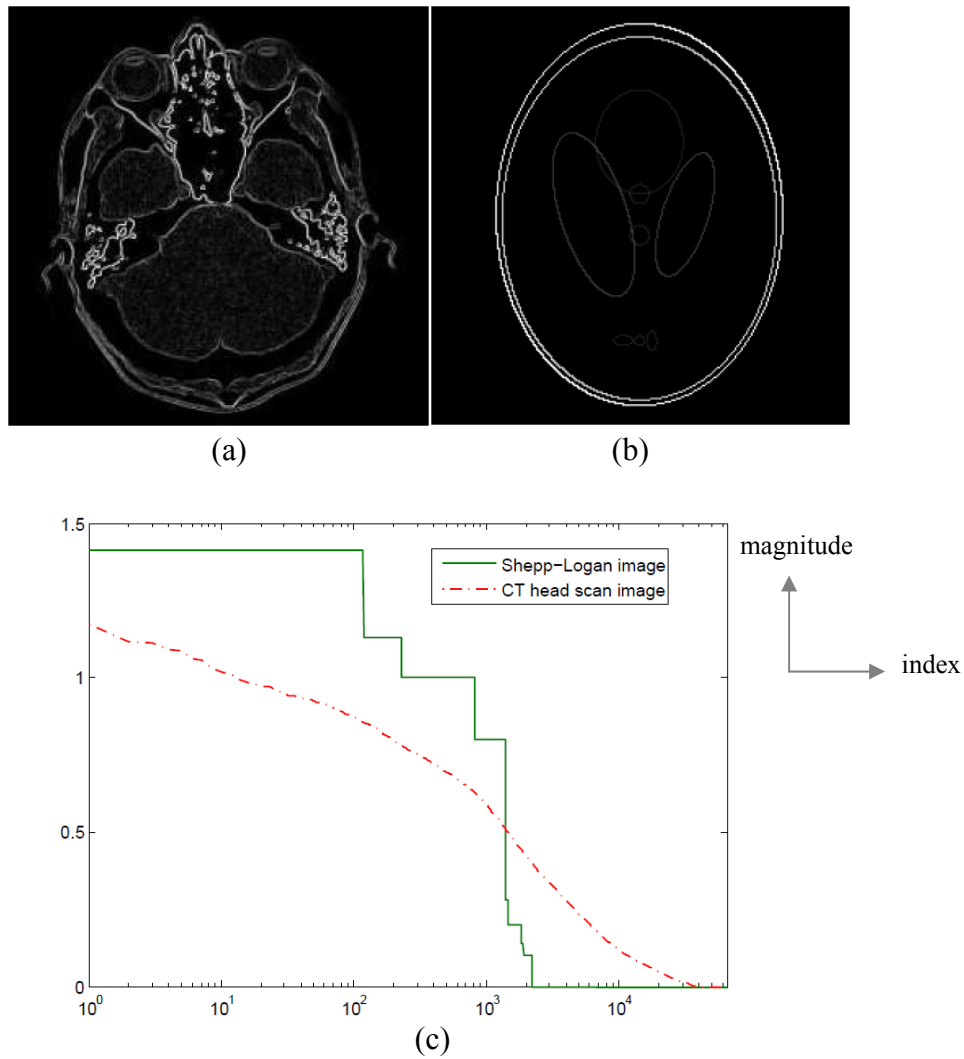


Fig. 6.2: GMIs used in experimenting FTV. (a) GMI of cranial CT (head scan) image. It has 38162 non-zero elements. (b) GMI of Shepp-Logan phantom image. It is 2184-sparse, (same as Fig. 3.3(c)). (c) Plot of the magnitude sorted coefficients in (a)-(b). The  $l_1$ -norm values are 4126 and 1460 for the cranial CT image and Shepp-Logan phantom image, respectively.

In experiments, data is acquired through either a half or full scan of true object using projection matrices that are calculated according to Method I. The parameters  $d$ ,  $\gamma_{\min}$  and  $\gamma_{\max}$  are set to  $1.038 \times 256 \times \sqrt{2}$ ,  $-\pi/7$  and  $\pi/7$ , respectively, in all computations. Equiangular set of detectors are presumed over an angular range of  $[\beta_{\min} = -\pi/2, \beta_{\max} = \pi/2]$  and  $[\beta_{\min} = -\pi, \beta_{\max} = \pi - (2\pi/\text{number of views})]$  for half and full scan configurations, respectively. It is assumed that projection data is obtained without any loss, meaning that there is always a detector reserved for capturing an individual ray-sum value (projection data). A 13-tap, symmetric high-pass filter defined in (2.6) is used to reconstruct images via FBP. Unless otherwise specified, the parameters used in FTV are set as given in Table 6.1.

Table 6.1: FTV parameters setting in the experiments.

|                           | $\tau_{\min}$ | $\tau_{\max}$ | $k_o$ | $r$ | $\epsilon_d$ |
|---------------------------|---------------|---------------|-------|-----|--------------|
| <i>E1,3<sup>*</sup>-4</i> | 1             | 99            | 18    | 0.8 | $10^{-3}$    |
| <i>E2<sup>**</sup></i>    | 1.5           | 99            | 22    | 0.8 | $10^{-4}$    |
| <i>E4<sup>***</sup></i>   | 1.5           | 9             | 26    | 0.8 | $10^{-8}$    |

\* *E3* includes an additional study with  $\tau_{\max}=9$ .

\*\* *E2* includes an additional study with  $\tau_{\max}=999$ ,  $k_o=66$ ,  $\epsilon_d=10^{-8}$ .

\*\*\* *E4* includes an additional study with  $k_o=14, 17$ , and  $34$ .

The displayed images are scaled arbitrarily for illustrative purposes. PSNR is used as an objective quality measure for reconstructions. All implementations are performed in Matlab. Only the non-zero elements of  $W$ ,  $D_h$  and  $D_v$  matrices are kept in memory allowing us to deallocate about 99% of the physical memory as compared to the case of their explicit declarations. Experiments are detailed individually in separate subsections below.

### 6.5.1 *E1*: Comparison with FBP

Few data, namely  $m = 30$  views  $\times$  256 rays/view measurements were collected by half scanning the Shepp-Logan phantom image. The measurements were used by FTV, yielding the reconstructed image shown in Fig. 6.3(b). The elliptic objects in

the recovery are clearly distinguished with nice contrast resolution. The sampled horizontal and vertical profiles of the reconstructed image match well to those of the true one as shown in Fig. 6.4(a)-(b). A significant degradation is only realized at the end of vertical profile, which corresponds to the bottom of head skeleton in Fig. 6.3(b). Since the X-ray source trajectory circulates only over the upper part of the object, the ray separations enlarge at lower portions, causing less information to be

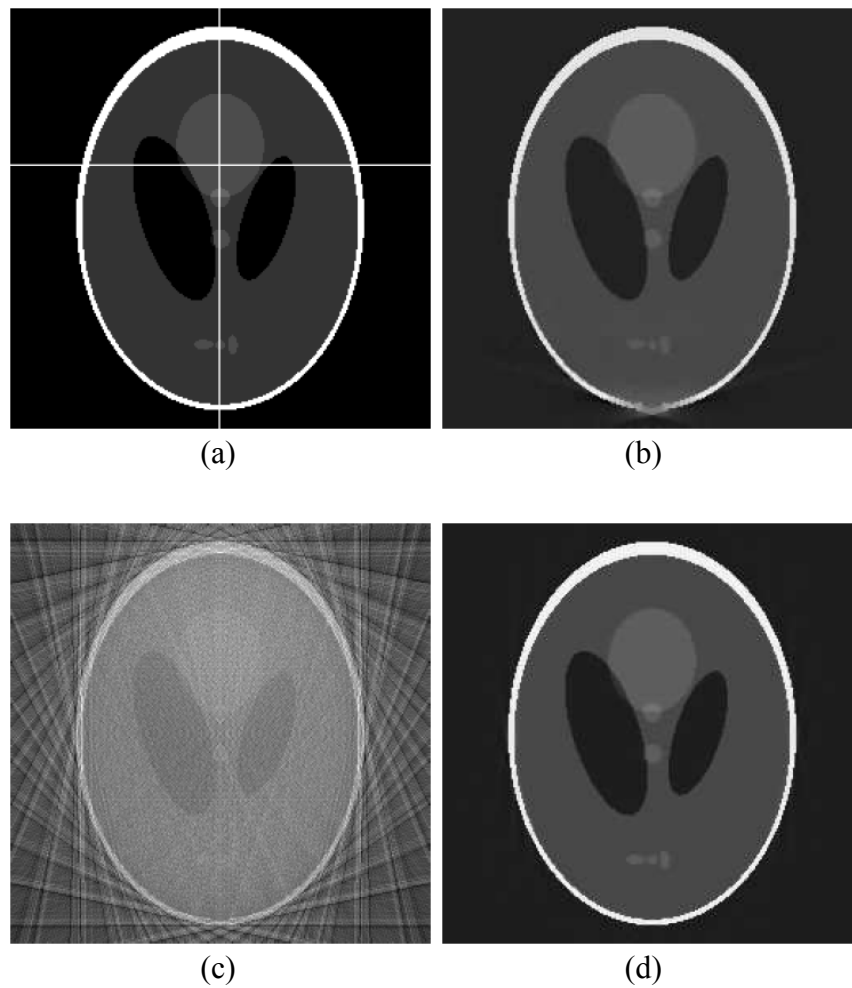


Fig. 6.3: The Shepp-Logan phantom image reconstructed in *EI*. (a) Original  $256 \times 256$  image. The horizontal and vertical lines are positioned respectively at the 96<sup>th</sup> row and the 128<sup>th</sup> column. The images in (b)-(d) are reconstructed using  $30 \text{ view} \times 256 \text{ rays/view}$  measurements that are obtained by either half or full scan of the original image. (b) Image reconstructed by FTV, PSNR = 79.0 dB (half scan). (c) Image reconstructed by FBP, PSNR = 57.1 dB, (full scan). (d) Image reconstructed by FTV, PSNR = 88.5 dB (full scan).

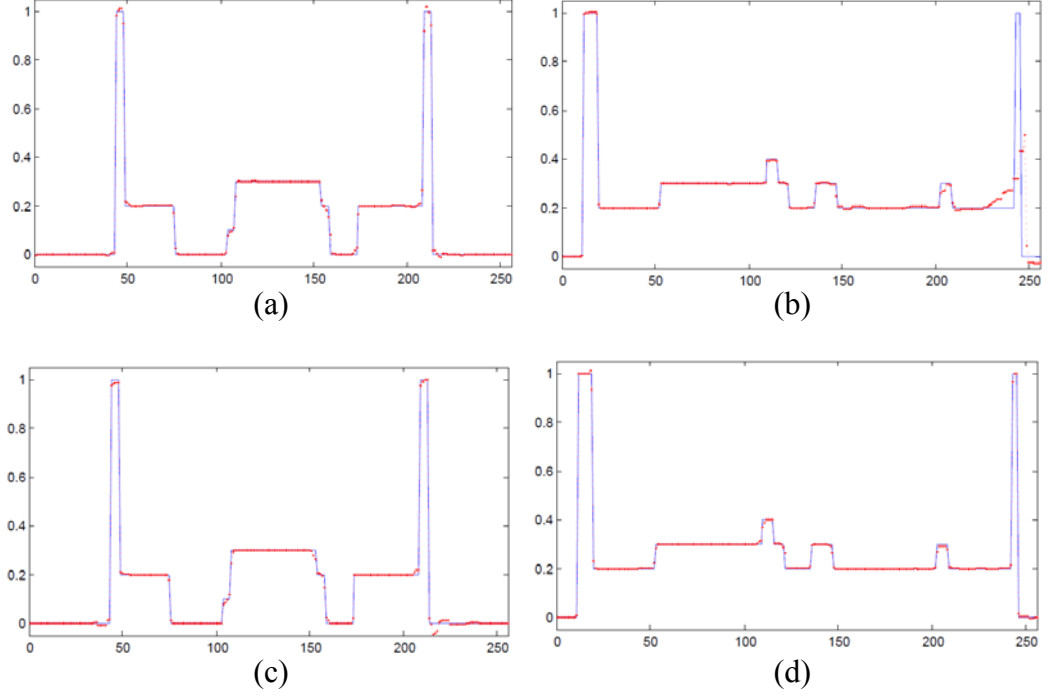


Fig. 6.4: Reconstructed image profiles in *EI*. (a) Horizontal profile at 96<sup>th</sup> row of the reconstruction in Fig. 6.3(b). (b) Vertical profile at 128<sup>th</sup> column of the reconstruction in Fig. 6.3(b). (c) Horizontal profile at 96<sup>th</sup> row of the reconstruction in Fig. 6.3(d). (d) Vertical profile at 128<sup>th</sup> column of the reconstruction in Fig. 6.3(d). The solid (blue) lines in (a)-(d) belong to the original image and the dashed (red) lines belong to FTV reconstructions.

acquired from the bottom regions. The advantage of getting sufficient information can be inferred from the analysis of reconstructed image shown in Fig. 6.3(d) where measurements obtained by full scanning the same object are used. The new vertical profile has significant improvements (see Fig. 6.4(d)). The data acquisition matrix  $W$  constructed in full scan geometry, from CS point of view, obeys UUP better than the one used in the half scan. That is, more information from the true object is gathered into the same number of measurements. In any configuration, FTV provides better recoveries than FBP. Having lower PSNR, the FBP solution shown in Fig. 6.3(c) especially suffers from the contrast resolution. The lower spatial resolution also causes small objects to be unrealized. However, it is remarkable that in many trials with less or more measurements than  $m$ , FBP outputted in no more than a few seconds in general. On the other hand, considering the same

measurements, FTV ended in a few minutes. The behavior of functional components as FTV iterates is analyzed by recording their values at each iteration. Their plots in Fig. 6.5(a)-(b) reveal parallelism in both scanning configurations. Since the initial point only minimizes  $RS(x)$ , its value increases, and  $f(x, \lambda)$  (or  $f(x)$  in short) decreases after the first iteration. As iterations proceed, it is a common tendency here and in other experiments that  $TV(x)$ ,  $RS(x)$  and  $f(x)$  are stabilized at their minimums. Here, in this particular experiment, iterations are halted by the decision mechanism at line 12 of Method VII. The additional iterations result in lower values in Fig. 6.5(b).

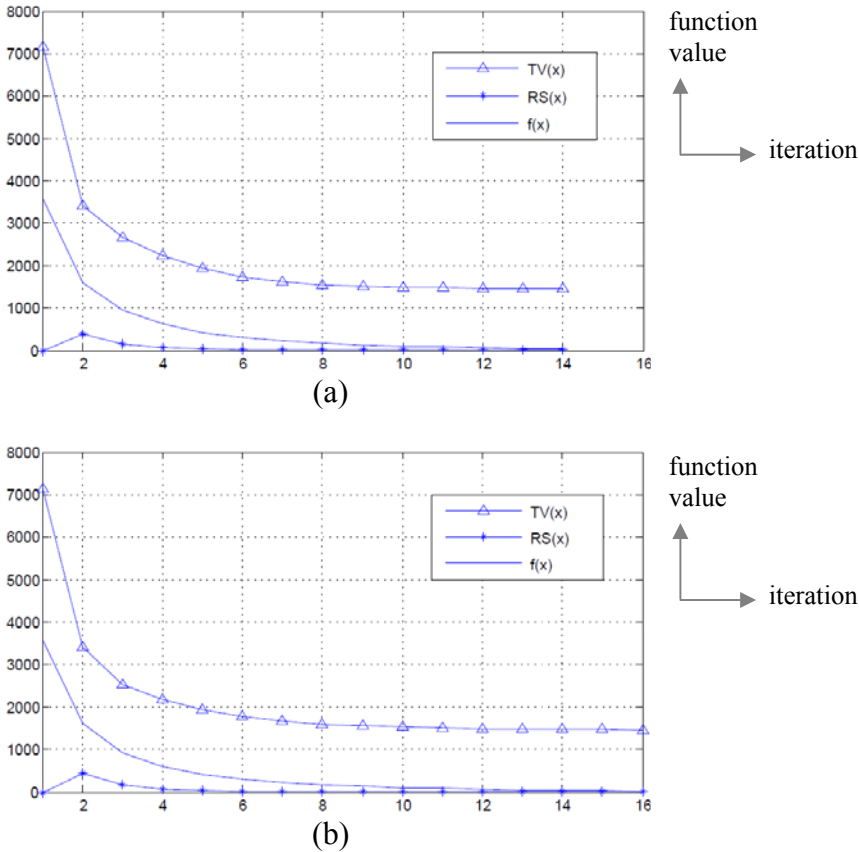


Fig. 6.5: Function values as FTV iterates in  $EI$ . The values of functional components are placed on the  $y$ -axis as iterations proceed on the  $x$ -axis. The plots belong to experiments in (a) Fig. 6.3(b) and (b) Fig. 6.3(d).

### 6.5.2 E2: Extended Comparison with FBP

The Shepp-Logan phantom image does not have fortuitous properties to which FTV is uniquely suited. CS based algorithms including FTV simply requires the object to have a conceivably sparse GMI. Instead of retesting FTV on an additional piece-wise constant phantom, the cranial CT image which does not fulfill the CS requirement properly is used for testing the performance of FTV. It is reconstructed first using full scan  $m = 7680$  ( $30$  views  $\times$   $256$  rays/view) measurements. The resultant FTV reconstruction shown in Fig. 6.6(e) has higher spatial and contrast resolution than the FBP solution in Fig. 6.6(b). As compared to the true image, however, spatial resolution is not satisfactory especially in regions where high frequency components dominate. A much better resolution is obtained when the number of measurements is doubled. Specifically, the reconstructed images in Fig. 6.6(c) and (f) are outputs of FBP and FTV that exploited  $2m = 15360$  ( $60$  views  $\times$   $256$  rays/view) measurements, respectively. The visual improvements relative to their recoveries from 30 views are significant, even much better than the solution of inverse FT shown in Fig. 6.6(d). The reconstruction through randomly selected  $2m$  coefficients, which can be considered analytically the best recovery without regularization, is behind the FTV reconstruction. Analyzing the horizontal and vertical profiles in Fig. 6.6(g)-(h), FTV reasonably traces the true trajectory, averaging the frequent changes in general. Because of its smoothing characteristics, FTV resulted in a lower TV image. It gets closer to the actual TV or a better estimate of the true image is attained when the number of measurements is increased (see the difference between Fig. 6.6(e) and (f)). FTV is initially run with slightly lower  $\lambda$  value to prevent over smooth images at the end. The execution is allowed to complete its maximum number of iterations by decreasing  $\epsilon_d$  tenfold, which serves the purpose of achieving lower  $RS(x)$ . The extra time needed for processing additional iterations is compensated by fast completion of iterations at the beginning. It is our experience that CG executes faster, i.e., exits early especially when the object of interest is non-sparse. Hereby, the execution time of FTV is almost the same in *E1* and *E2*.

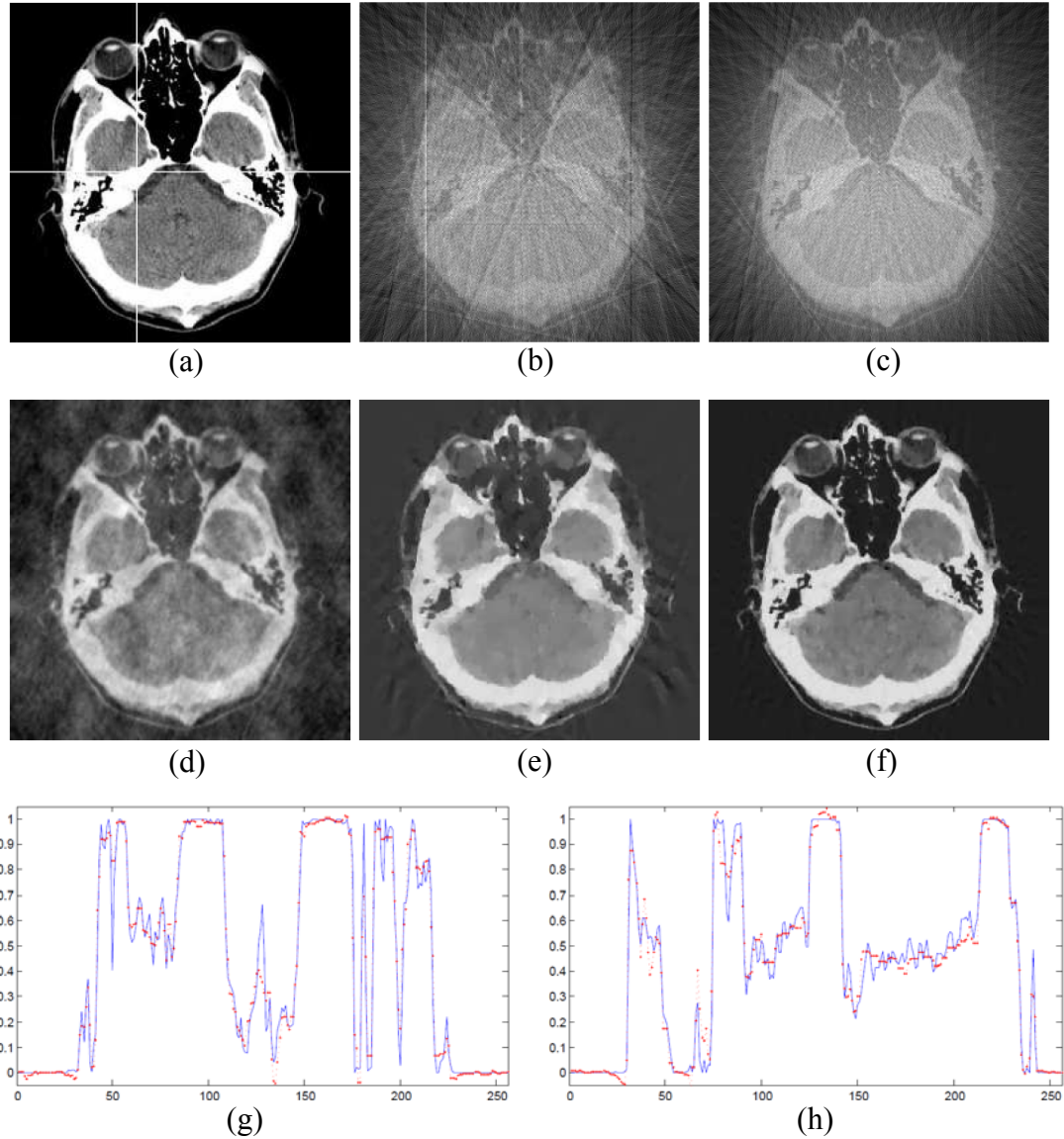


Fig. 6.6: The cranial CT image reconstructed in *E2*. (a) Original  $256 \times 256$  image. The horizontal and vertical lines are positioned respectively at the  $128^{\text{th}}$  row and the  $96^{\text{th}}$  column. The images in (b)-(c) and (e)-(f) are reconstructed using different number of measurements obtained from a full scan of the original image. (b) Image reconstructed by FBP using  $30 \text{ view} \times 256 \text{ rays/view}$  measurements, PSNR=58.9 dB. (c) Image reconstructed by FBP using  $60 \text{ view} \times 256 \text{ rays/view}$  measurements, PSNR=59.1 dB. (d) Image reconstructed by inverse FT using  $2 \times 7680$  noise-free Fourier coefficients, PSNR = 66.4 dB. (e) Image reconstructed by FTV using  $30 \text{ view} \times 256 \text{ rays/view}$  measurements, PSNR = 70.1 dB. (f) Image reconstructed by FTV using  $60 \text{ views} \times 256 \text{ rays/view}$  measurements, PSNR = 75.2 dB. (g) Horizontal profile at the  $128^{\text{th}}$  row of FTV reconstruction. (h) Vertical profile at the  $96^{\text{th}}$  column of FTV reconstruction. The solid (blue) lines in (g)-(h) belong to original image and the dashed (red) lines belong to FTV reconstruction in (f).



As a second part of *E2*, we investigate the improvement in PSNR relative to the amount of radiation absorption in the cranial CT image. FTV is reconfigured using different parameter values and executed unusually for various full scan view configurations. Particularly, starting from a reference  $m = 7680$  (30 views  $\times$  256 rays/view) measurements, they are increased at every reconstruction by adding 8 views  $\times$  256 rays/view data until reaching 94 views  $\times$  256 rays/view measurements. The same initial point computed for the reference reconstruction is used in the others. As a consequence, the CG iterations exit early, decreasing  $f$  faster in the subsequent reconstructions. It is probable that maximum number of iterations is used up without approaching the true object sufficiently, requiring more iterations than set in the first part. Therefore,  $k_o=66$ ,  $\tau_{\max}=999$ , and  $\varepsilon_d=10^{-8}$  are used to make a consistent configuration for all. The amount of radiation absorbed is computed using (2.7). They are expressed in Table 6.2 relative to the amount belonging to the reference reconstruction. FTV results in monotonic increases in PSNR and reliable reconstructions as the dose absorbed increased. FBP has small fluctuations at a lower PSNR level although recoveries show visual improvements gradually. These fluctuations arise mainly from striking artifacts outside the object. They can be removed significantly using much more measurements, e.g., hundredfold, unfortunately.

Table 6.2\*: PSNR versus relative radiation absorbed (RRA).

| <b>RRA</b> | <b>1</b> | <b>1.26</b> | <b>1.53</b> | <b>1.80</b> | <b>2.06</b> | <b>2.33</b> | <b>2.59</b> | <b>2.86</b> | <b>3.13</b> |
|------------|----------|-------------|-------------|-------------|-------------|-------------|-------------|-------------|-------------|
| <b>FBP</b> | 58.93    | 59.06       | 58.48       | 59.24       | 59.13       | 58.89       | 59.17       | 59.17       | 59.28       |
| <b>FTV</b> | 70.17    | 70.27       | 73.09       | 73.88       | 73.89       | 74.74       | 76.50       | 76.89       | 76.99       |

\* The first row displays the relative values of the absorbed radiation amount. The second and third rows display corresponding PSNR values of the images reconstructed via FBP and FTV, respectively. The information given in the first column belongs to the reference reconstruction that is obtained using  $m = 30$  views  $\times$  256 rays/view measurements from the full scanning of cranial CT image.

### 6.5.3 E3: Robustness to Additive Noise

*EI* is essentially repeated with full scan measurements that are contaminated by the zero-mean white Gaussian noise. Many reconstructions are performed at different noise levels. The resultant PSNRs are given in Table 6.3. The reason that the PSNR values corresponding to lower noise levels ( $\sigma = 0.005$  or  $0.01$ ) are greater than the value computed in *EI* is that, in a noisy situation, FTV executes the maximum allowable number of iterations since the relative change of  $TV(x)$  do not fall below  $\varepsilon_d$ . As the noise power gets strengthened, i.e.,  $\sigma^2 \geq 4 \times 10^{-2}$ , degradations become perceivable. For instance, consider the recovery in Fig. 6.7(c) where variations within objects are noticeable. But then, the resolution is much better than the solution of noise-free inverse FT shown in Fig. 6.7(b). The better identification of objects within the recovery in Fig. 6.7(c) is also verified by its sampled profiles. Analyzing these profiles in Fig. 6.8(a)-(b), it is observed that true intensity levels are stably obtained with little ripples. It would be possible to further improve the recovery by truncating pixels outside the feasible region,  $[0, 1]$ . Because of noise, stabilization of  $TV(x)$  gets hard. It tends to increase (see Fig. 6.9(a)) as iterations proceed with a lower regularization parameter. In order to enforce  $TV(x)$  to steadily approach the desired minimum, we rerun FTV by setting  $\tau_{\max} = 9$ . Thus, the lowest value that  $\lambda$  could take is increased tenfold, preventing conjugate directions to move far away from  $-\nabla TV(x)$ . The new reconstructed image that is shown in Fig. 6.7(d) is obtained with better  $TV(x)$  (see Fig. 6.9(b)) and hence PSNR.

Table 6.3 \*\*: PSNR of images reconstructed by FTV using noisy measurements.

| $\sigma$           | 0.005 | 0.01  | 0.02  | 0.05  | 0.1   | 0.2   | 0.2   | 0.5   | 0.5   |
|--------------------|-------|-------|-------|-------|-------|-------|-------|-------|-------|
| $\ Wx\ _2/\ e\ _2$ | 75.88 | 69.86 | 63.84 | 55.88 | 49.86 | 43.84 | 43.84 | 35.88 | 35.88 |
| PSNR               | 89.28 | 88.83 | 87.31 | 84.34 | 81.10 | 78.02 | 81.13 | 73.17 | 73.69 |

\*\* The first row displays values of standard deviations for additive Gaussian white noise  $e$  having  $N(0, \sigma^2)$  characteristics. The second and third rows display corresponding signal to noise ratios and PSNR values of reconstructed images, respectively. All reconstructions are obtained by FTV with  $\tau_{\max} = 99$  except the dashed columns for which  $\tau_{\max}$  is set to 9.  $m = 30$  view  $\times$  256 rays/view measurements from a full scan of the Shepp-Logan phantom image are used.

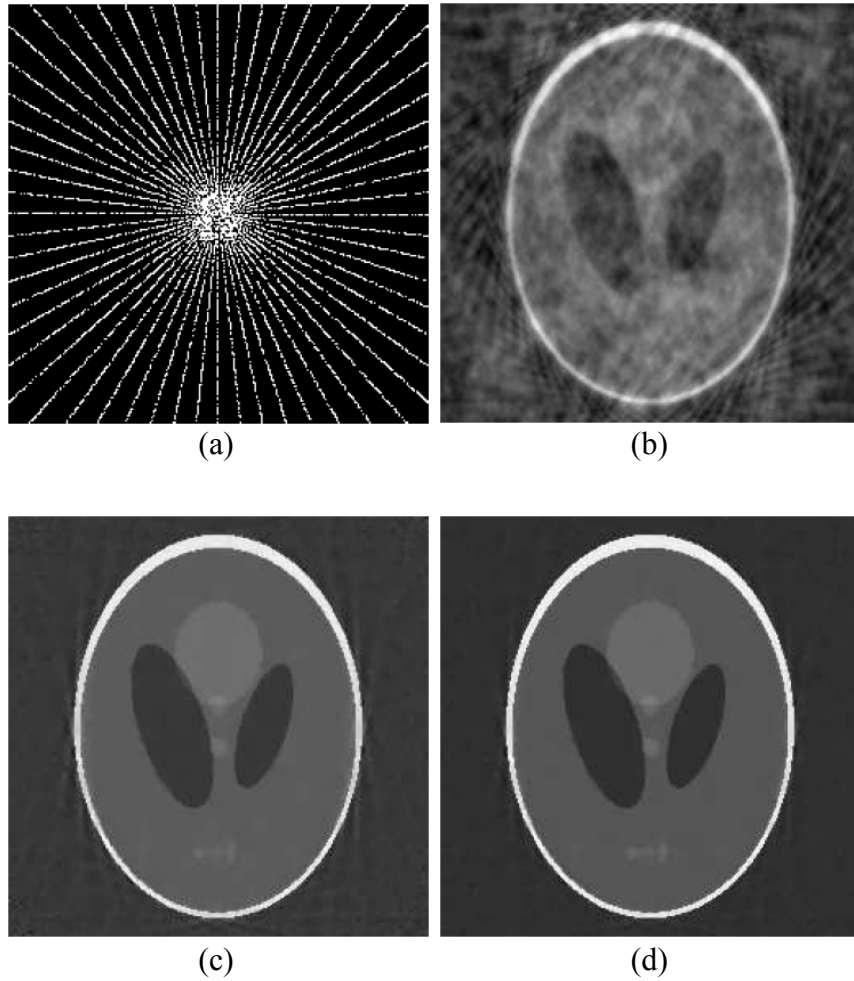


Fig. 6.7: The Shepp-Logan phantom image reconstructed in  $E3$ . A white Gaussian noise having the characteristics of  $\mathcal{N}(0, 4 \times 10^{-2})$  is added to the measurements in (c)-(d). (a) The sampling pattern of Fourier coefficients on 2-D Fourier space. The display area is  $[-\pi, \pi) \times [-\pi, \pi)$ . The sampled coefficients are used for the recovery in (b). (b) Image recovered from 7680 noise-free Fourier coefficients by inverse FT, PSNR = 63.3 dB. (c) Image recovered from noisy measurements via FTV with  $\tau_{\max}=99$ . (d) Image recovered from noisy measurements via FTV with  $\tau_{\max}=9$ .  $m = 30$  views  $\times$  256 rays/view measurements from full scan of the original Shepp-Logan phantom image are used for both reconstructions in (c) and (d). PSNRs are given in Table 6.3.

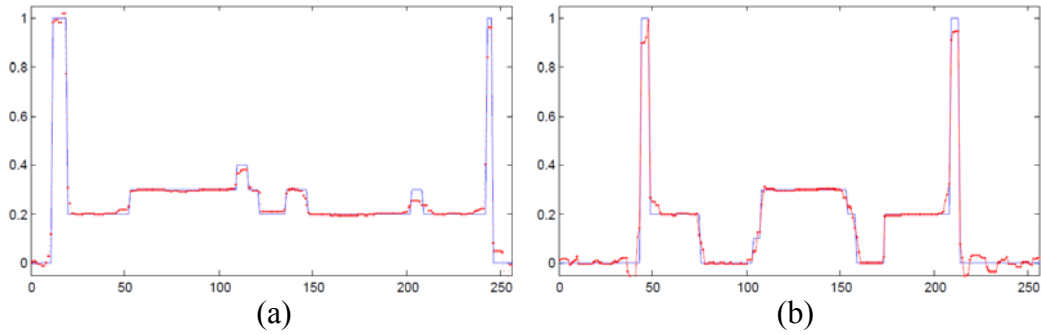


Fig. 6.8: Reconstructed image profiles in  $E3$ . A white Gaussian noise having the characteristics of  $\mathcal{N}(0, 4 \times 10^{-2})$  is added to measurements in Fig. 6.7(c)-(d). (a) Horizontal profile at the 96<sup>th</sup> row of the recovery in Fig. 6.7(c). (b) Vertical profile at the 128<sup>th</sup> column of the recovery in Fig. 6.7(c). Solid (blue) lines in (a)-(b) belong to the original Shepp-Logan image and dashed (red) lines belong to the FTV reconstruction.

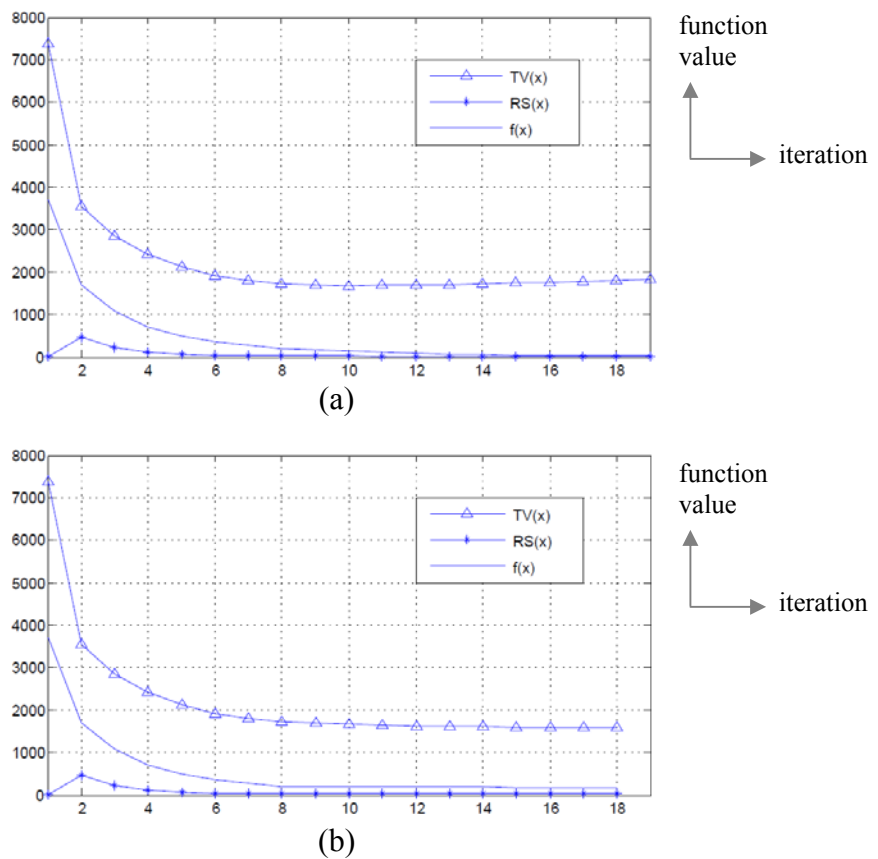


Fig. 6.9: Function values as FTV iterates in  $E3$ . The values of functional components are placed on the  $y$ -axis as iterations proceed on the  $x$ -axis. The plots belong to experiments in (a) Fig. 6.7(c) and (b) Fig. 6.7(d).

#### 6.5.4 *E4*: A Multi-Purpose Performance Test

The performance of FTV is tested against the additive white Gaussian noise and the images recovered from the same number of measurements that are acquired under different scanning configurations are analyzed in two respective parts of *E4*. Regarding these aims, part one and two can be considered as extensions of *E3* and *E1*, respectively. The major difference of *E4* is the use of cranial CT image in both, plus the projection of few X-rays in many views instead of projecting many X-rays in few views in the second part. The details of the experiment are as follows:

The cranial CT image is reconstructed from  $2m = 60 \text{ views} \times 256 \text{ rays/view}$  measurements that are contaminated by zero-mean white Gaussian noise of  $\sigma = 0.5$ . The noise contamination constitutes a SNR of 43.1 dB. Although the GMI of cranial CT image is hardly sparse, a high valued  $\tau_{\max}=9$  is used to smooth the fluctuations because of noise. The maximum number of outer loop iterations allowed is limited to  $k_o=26$  which is slightly higher than the value used in *E2*. A low valued  $\varepsilon_d=10^{-8}$  is used to make the stopping criterion which is based on  $k_o$  come into prominence in particular. While the spatial and contrast resolutions of the reconstructed image shown in Fig. 6.10(b) are poorer than the noise-free recovery shown in Fig. 6.10(a), they are much higher than those of the noise-free FBP solution in Fig. 6.10(c). Regarding the spatial resolution, a similar performance under the same SNR is observed in Fig. 6.10(d) where the recovery is obtained by FBP using  $12m = 180 \text{ views} \times 512 \text{ rays/view}$  measurements corresponding to a sixfold increase in the amount of radiation absorbed. On the other hand, it is remarkable that FBP is not sensitive to noise as much as FTV because images are smoothed naturally in back projection. For example, considering the image shown in Fig. 6.10(d), the noise is hardly perceived until the SNR falls below 30 dB. Its contrast resolution and PSNR can also be improved by tuning the filter parameters so as to suppress the low frequency components more.

In the second part of *E4*, the cranial CT image is reconstructed by FTV and FBP using noise-free  $2m = 120/60/30 \text{ views} \times 128/256/512 \text{ rays/view}$  measurements. The reconstructed images are shown in Fig. 6.11 where an illustration of the

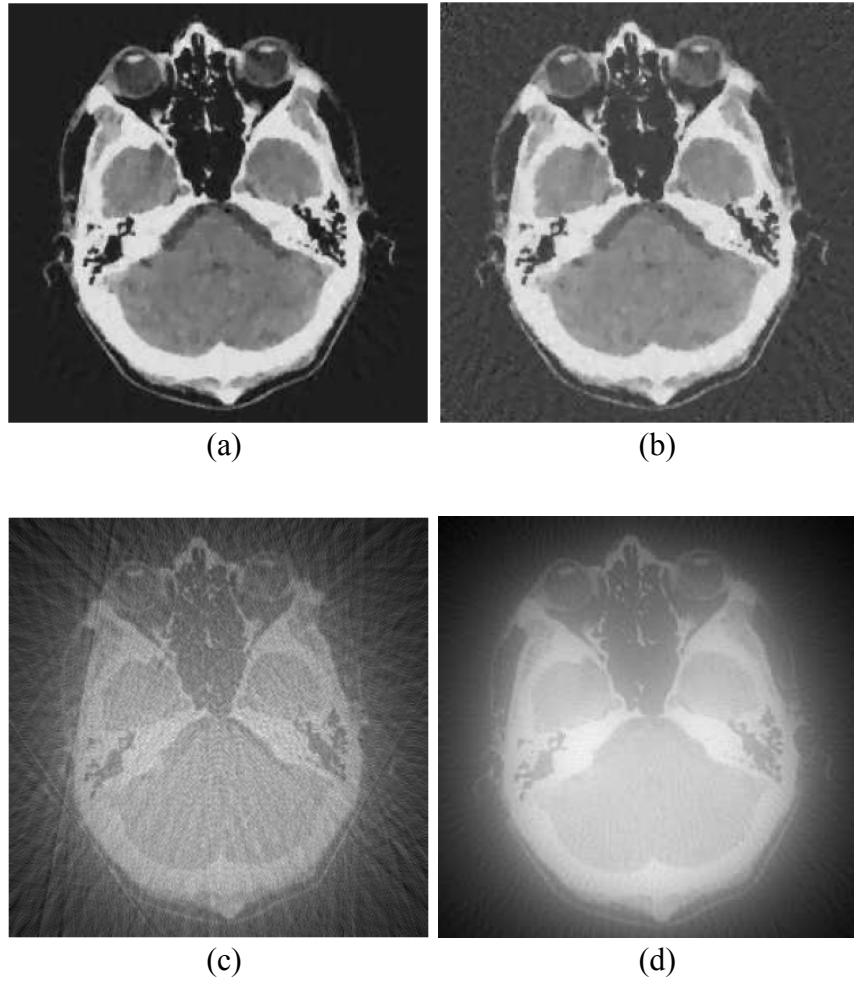


Fig. 6.10: The cranial CT image reconstructed in *E4* (Part 1). (a) The image reconstructed by FTV using noise-free  $2m = 60$  views  $\times$  256 rays/view (full scan) measurements, PSNR = 75.2 dB. It is the same recovery shown in Fig. 6.6(f). (b) The image reconstructed by FTV using noisy  $2m = 60$  views  $\times$  256 rays/view (full scan) measurements, PSNR = 72.5 dB. A white Gaussian noise having the characteristics of  $\mathcal{N}(0, 0.25)$  is added to the measurements, SNR = 43.1 dB. (c) The image reconstructed by FBP using noise-free  $2m = 60$  views  $\times$  256 rays/view (full scan) measurements, PSNR = 59.1 dB. The recovery is the same as shown in Fig. 6.6(c). (d) The image reconstructed by FBP using noisy  $12m = 180$  views  $\times$  512 rays/view (full scan) measurements, PSNR = 58.7 dB. The additive zero mean white Gaussian noise constitutes the same SNR = 43.1 dB.

scanning configurations is given as well. The numbers of X-rays depicted in Fig. 6.11(a)-(c) are proportional with the actual number of measurements used in the experiment. For each configuration, a different value of  $k_0$  is used to let FTV run for about a minute. Our main observation on the reconstructed images is the more

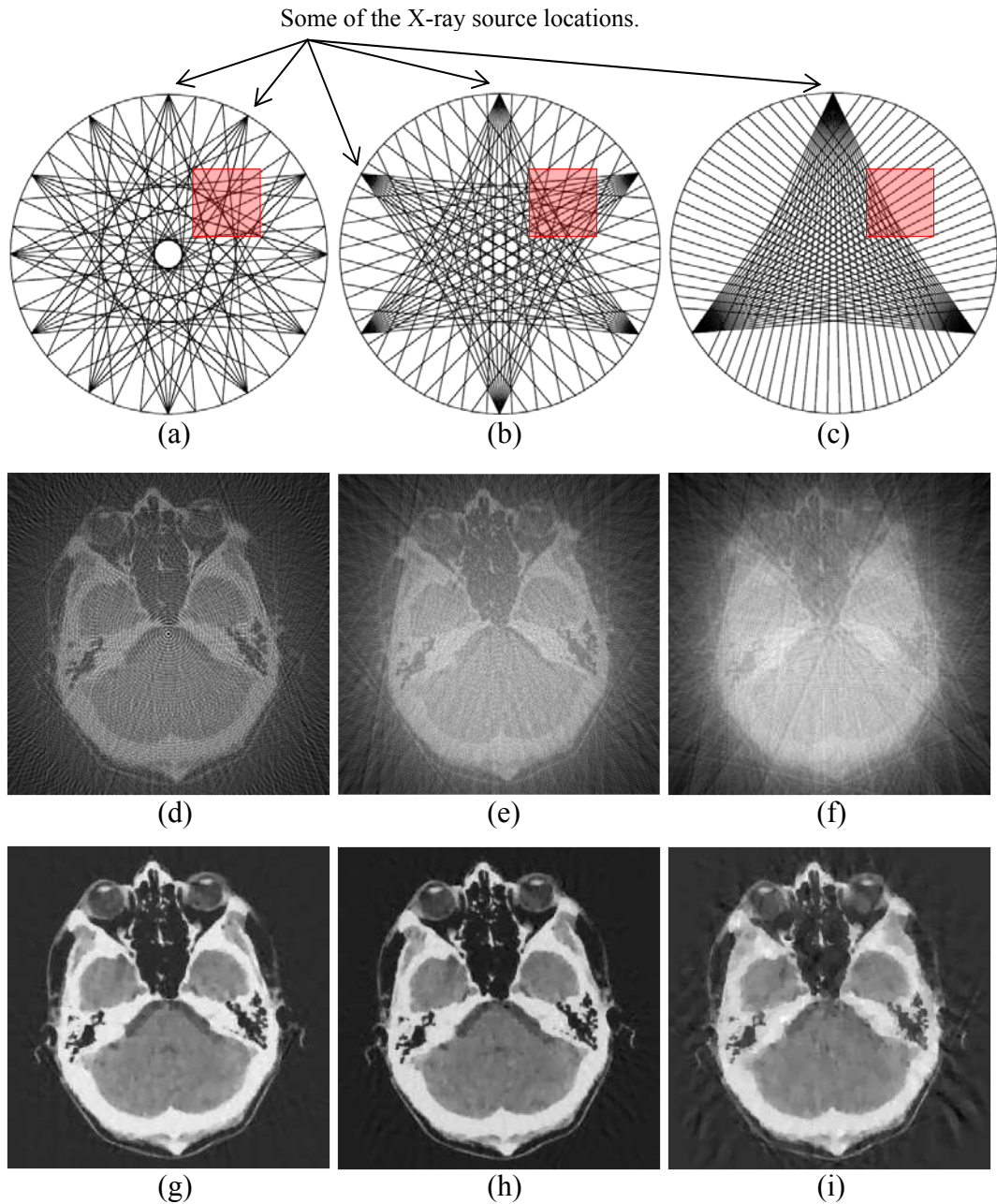


Fig. 6.11: The cranial CT image reconstructed in *E4* (Part 2). Each column corresponds to a different scanning configuration. An illustration of (a) 120 views  $\times$  128 rays/view configuration, (b) 60 views  $\times$  256 rays/view configuration, (c) 30 views  $\times$  512 rays/view configuration. (d) The image reconstructed by FBP using  $2m = 120$  views  $\times$  128 rays/view measurements, PSNR = 59.8 dB. (e) The image reconstructed by FBP using  $2m = 60$  views  $\times$  256 rays/view measurements, PSNR = 59.1 dB. (f) The image reconstructed by FBP using  $2m = 30$  views  $\times$  512 rays/view measurements, PSNR = 58.5 dB. (g) The image reconstructed by FTV ( $k_0=34$ ) using  $2m = 120$  views  $\times$  128 rays/view measurements, PSNR = 74.1 dB. (h) The image reconstructed by FTV ( $k_0=17$ ) using  $2m = 60$  views  $\times$  256 rays/view measurements, PSNR = 74.7 dB. (i) The image reconstructed by FTV ( $k_0=14$ ) using  $2m = 30$  views  $\times$  512 rays/view measurements, PSNR = 70.4 dB.

the information from the object is, the better the recoveries are. As an example, the numbers of X-rays passing through the red square regions shown in Fig. 6.11(a)-(c) are 31, 32, and 22, respectively. The amount of information from these regions is proportional with the number of X-rays passing through them. Therefore, the best recovery shown in see Fig. 6.11(h) is obtained in the case of  $60 \times 256$  measurements. It is notable that incoherent measurements are crucial for FTV to provide satisfactory recoveries. Consider the 14 X-rays in Fig. 6.11(a); they emerge from different sources, pass through the red region, and also coincide. Therefore, only 7 of them make reasonable contributions to the measurements; 24 X-rays are sufficient to be utilized in FTV. On the other hand, the back projection of the same or coherent information changes the contrast resolution of the reconstructed image. They are illuminated more. The filter needs adjustment to compensate it. Like FTV, FBP provides better recoveries as more information is gathered from the object.

### 6.5.5 E5: Comparison with Other CS based Solutions

The performance of FTV configured in *E1* is compared with other CS based algorithms given in Chapters 4 and 5. For this reason, the full-scan measurements ( $m = 30 \text{ views} \times 256 \text{ rays/view}$ ) and initial estimate of the Shepp-Logan phantom image in *E1* are used in all algorithms running on Intel® Core™ i7-2630QM CPU @ 2.00 GHz processor running Windows®7 OS. In SOCP, the numbers of Newton and SYMMLQ iterations are fixed at  $n_{nw} = 20$  and  $c = 5000$ , respectively. In ASD-POCS and ASD-FT, the number of steepest-descent iterations are set to  $n_{sd} = 20$ . While SOCP ends after  $k_b = 10$  iterations, ASD-POCS and ASD-FT are allowed to execute  $k_p = 120$  iterations. Since data collected in fan scan geometry has no counterpart in image's Fourier space, we exploit ASD-FT in a different manner: The discrete Fourier transform coefficients of the estimated image shown in Fig. 6.7(a) are replaced by the true ones that have been analytically computed once from the original image. Regarding its impracticality, putting this implementation into comparison is in fact unfair. However, we approve of it as a golden solution for applications in parallel or diffraction beam tomography and consider useful in comparison with FTV. The results shown in Figs. 6.12-6.15 are based on PSNRs in current estimation and cumulative processing times as iterations proceed. The main



observation is FTV approaches more rapidly to the true object in a less period of time. Although SOCP converges to a better solution in less number of iterations, the processing time of its main loop is longer and its overall execution time is more than that of ASD-POCS. The slowest convergence rate in a single iteration belongs to ASD-POCS and ASD-FT. In particular, ASD-FT hardly provides high PSNR no matter how much iterations are performed. Another observation about the convergence of FTV is its incompleteness in Fig. 6.12. Higher PSNRs could be expected with more iterations. However, this could be achieved only at the expense of prolonged execution time of CG iterations. Recall that when the current estimate gets closer to the true object, more CG iterations and hence time is required to minimize  $f$ . But then, the overall execution time of FTV is at most one tenth of others concerning a high PSNR. The results given in Figs. 6.12 - 6.15 are combined in a single plot shown in Fig. 6.16 where FTV and SOCP come into prominence regarding the higher reconstruction speed and more accurate recovery, respectively. The poor performance of ASD-FT is because of the randomly selected coefficients that are mostly insignificant. It will be poorer if the coefficients are estimated.

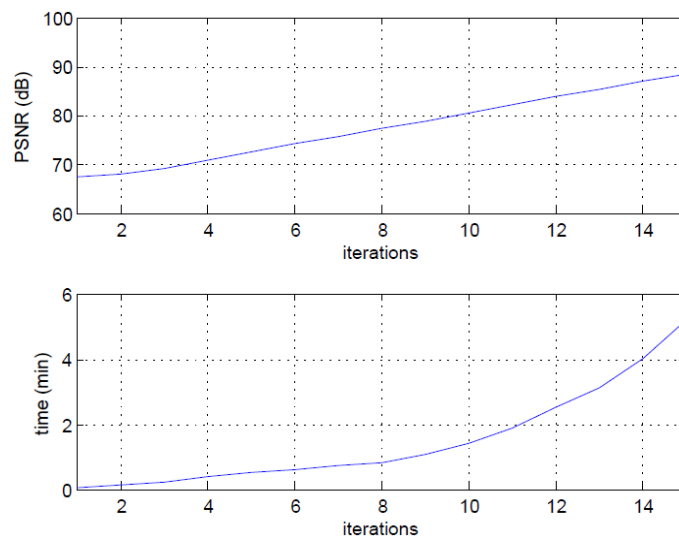


Fig. 6.12: PSNR and time recordings in iterations of FTV. The upper subplot shows PSNR (in dB) versus number of iterations. The lower subplot shows cumulative processing times (in minutes) versus the number of main loop iterations. The plot belongs to the reconstruction of the Shepp-Logan phantom image using (full-scan)  $30 \text{ views} \times 256 \text{ rays/view}$  measurements.

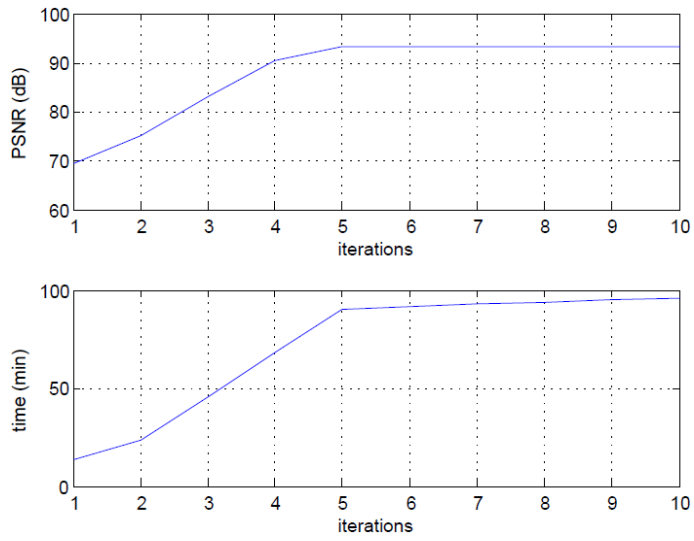


Fig. 6.13: PSNR and time recordings in iterations of SOCP. The upper subplot shows PSNR (in dB) versus number of iterations. The lower subplot shows cumulative processing times (in minutes) versus the number of main loop iterations. The plot belongs to the reconstruction of the Shepp-Logan phantom image using (full-scan)  $30 \text{ views} \times 256 \text{ rays/view}$  measurements.

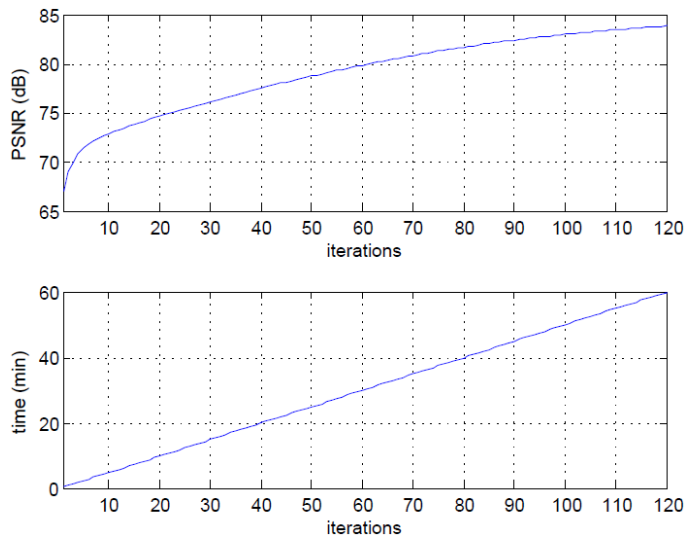


Fig. 6.14: PSNR and time recordings in iterations of ASD-POCS. The upper subplot shows PSNR (in dB) versus number of iterations. The lower subplot shows cumulative processing times (in minutes) versus the number of main loop iterations. The plot belongs to the reconstruction of the Shepp-Logan phantom image using (full-scan)  $30 \text{ views} \times 256 \text{ rays/view}$  measurements.

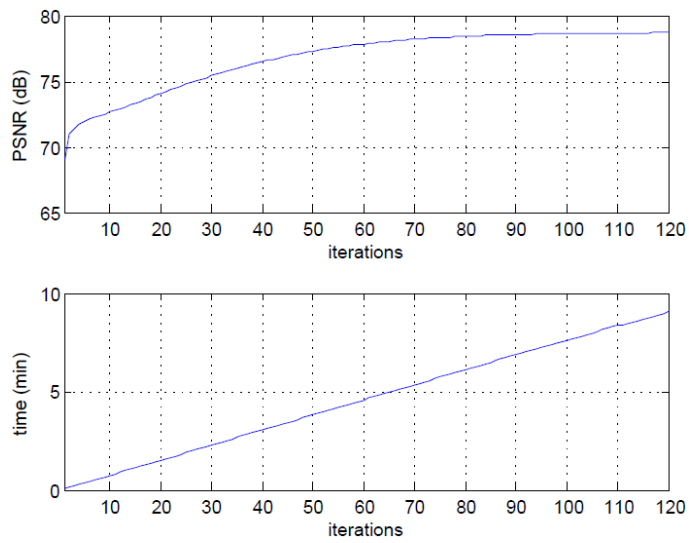


Fig. 6.15: PSNR and time recordings in iterations of ASD-FT. The upper subplot shows PSNR (in dB) versus number of iterations. The lower subplot shows cumulative processing times (in minutes) versus the number of main loop iterations. The plot belongs to the reconstruction of the Shepp-Logan phantom image using (full-scan)  $30 \text{ views} \times 256 \text{ rays/view}$  measurements.

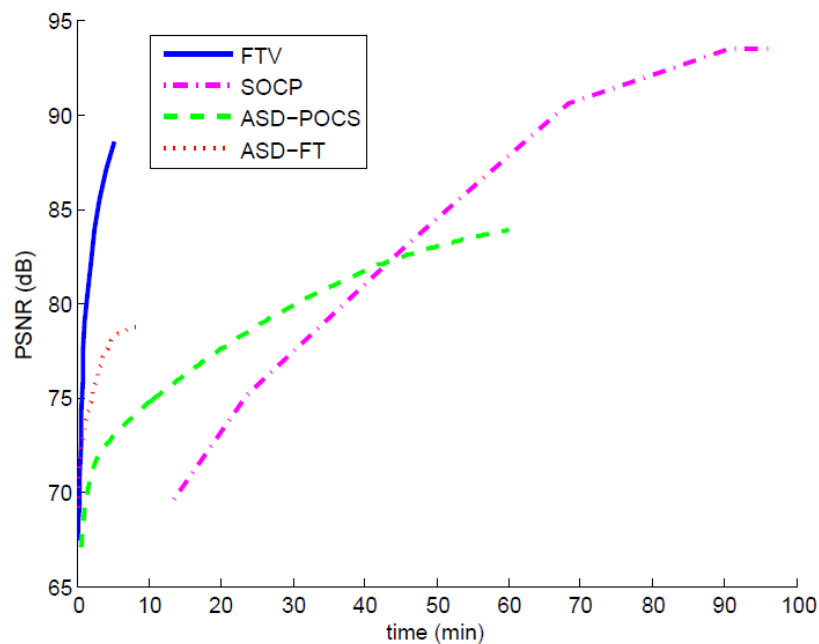


Fig. 6.16: Performance comparison of FTV with other CS based solutions. It is a combination of all plots in Figs. 6.12 - 6.15.

## CHAPTER 7

### CONCLUSIONS

In this study, we aimed to reduce X-ray radiation exposure in CT imaging and therefore decrease the amount of radiation absorbed by patients and/or operators during CT examinations. We concentrated on the notion of compressed sensing based computerized tomography imaging. Among various dose reduction strategies, CS based CT imaging takes participate in improving the image reconstruction algorithms. Namely, the proposed schemes in Chapters 5 and 6 of this thesis provide better recoveries under low dose radiation as compared to traditional methods. To summarize, this thesis involves:

- the review of CT imaging and traditional image reconstruction algorithms,
- the review of CS from theoretical and practical standpoints,
- the discussion of CS integration into the CT imaging systems,
- the review of CS based reconstruction algorithms,
- the proposal of SOCP,
- the proposal of FTV.

The image reconstruction algorithms in commercial CT scanners today are based on processing huge projection data that are obtained by making use of many X-ray beams passing through the object of interest. The efficacy of traditional FBP based algorithms or ARTs used for image reconstruction is remarkable if the number of beams is very high. However, too many beams passing through the body may induce cancer together with the consideration of the fact that the radiation dose in CT is usually higher than those used in other diagnostic imaging. Since every examination causes the risk of cancer induction to increase, it is crucial to decrease

the number of beams and therefore the radiation exposure during examinations. Unfortunately, using less number of beams or measurements from the body causes degradations in reconstructed images. It is possible to get rid of these degradations by exploiting the CS theory. It requires the objects of interest to be sparse or have an approximately sparse representation to recover images from few measurements. Moreover, these measurements should be obtained randomly and carry as much information from the object as possible. Therefore, the objects can be recovered from few measurements by solving a convex optimization problem.

It is possible to fulfill the CS requirements in CT imaging: Most CT images have sparse representation in various transform domains, e.g., Fourier, wavelet, etc. In particular, the image gradient representation is sparser than representations in other domains. The data acquisition model constructed in CT imaging allows incoherent measurements such that it is unlikely that the measurement vectors formed at rows of the projection matrix  $W$  match to the object structure. Therefore, the CS based CT imaging problem can be defined as the  $l_1$ -norm minimization of the image gradient magnitude considering the measurements from the object. Its solution provides better recoveries from fewer measurements than those required by traditional image reconstruction algorithms.

In the first part of our study, we reformulated the CS based CT imaging problem as SOCP and proposed a generic log-barrier algorithm to solve it. The Newton's method which is embedded in the log-barrier algorithm allows accurate solutions. Using few X-ray projections, the CT images are reconstructed almost exactly via SOCP whereas the same visual quality is hardly obtained by traditional methods. Since the X-ray radiation absorption is lowered by decreasing the number of projections, the risk of cancer induction in CT examinations is reduced a lot. Although, the solution algorithm for SOCP has higher convergence rate, its reconstruction time prolongs at large scale problems because of its high order of operational complexity. While the gap between the reconstruction times of FBP and SOCP may extend to an hour especially for large scale problems, it provides solutions faster than POCS based algorithms especially for small scale problems.

SOCP requires more iterations to solve Newton approximations as the size gets larger.

In the second part of our study, we introduced a faster CS based image reconstruction algorithm FTV for recovering CT images from few X-ray projections. Instead of operating nested or consecutive loops as in SOCP or ASD-POCS/ASD-FT, FTV benefits from the CG method which participates as a single block of operation in iterations. Like SOCP, FTV provides more qualified images using less number of measurements than FBP requires. The realizations under noisy circumstances are better than the noise-free solution that is obtained by the inverse Fourier transform of the true coefficients. The operational complexity of FTV is less than the POCS based algorithms. It reconstructs images faster, which becomes evident especially in large scale problems. Instances of poor performance of FTV is observed when the estimate at the current iterate is close to the optimum solution. Then, the execution time of the succeeding iterations prolongs. Optionally, iterations may be ceased in such instances, or, the minimization of the objective function can be continued using the steepest-descent method with a small constant step-size in place of CG. It is possible to improve the proposed scheme also by adapting the stopping criterion to timing constraints.

Currently, none of the CS based algorithms matches the speed of FBP yet. If speeds are put in perspective, we can roughly say that FBP, FTV and others reconstruct a typical  $256 \times 256$  image in a few seconds, minutes, and hours, respectively. Exceptionally, the reconstruction speeds of the FT based algorithms are close to FTV due to the availability of fast FT routines. However, they cannot provide recoveries accurate as much as the recoveries obtained by other CS based algorithms. Although in our study we implement the ASD-FT algorithm using the true FT coefficients, one has to estimate them via interpolations in iterations in practice. The interpolation errors cause degradations at the output images. It is also remarkable that images reconstructed by FBP show less degradation under the same noise power as compared to the CS based algorithms. The back projections smooth noise naturally, making recoveries look better.

Finally, we conclude that the CS based algorithms including our proposed SOCP and FTV are very attractive for CT imaging systems due to their applicability to use fewer measurements from random scanning geometries as opposed to traditional FBP based algorithms or ARTs. Since they are based on iterative techniques, their reconstruction time is much higher than FBP. SOCP takes prominence regarding the accuracy of the reconstructed images. Although its reconstruction speed is higher than POCS based algorithms in small scale problems, it suffers from huge matrix vector multiplications in large scale problems. FTV takes prominence regarding the image reconstruction speed no matter the problem size is. It would be beneficial to validate the performance of the proposed schemes in clinical use. Besides, the theoretical studies can be extended by including a more thorough experimental evaluation involving wider classes of noise. Moreover, constructing the optimum projection matrix and so the scanning configuration seems to remain as an open research subject.

## REFERENCES

- [1] J. Radon, "Über die Bestimmung von Funktionen durch ihre Integralwerte längsgewisser Mannigfaltigkeiten (on the determination of functions from their integrals along certain manifolds)," *Berichte Sächsische Akademie der Wissenschaften*, vol. 29, pp. 262 - 277, 1917.
- [2] G. Hounsfield, "A method of an apparatus for examination of a body by radiation such as x-ray or gamma radiation," Patent specification 1283915, The Patent Office, 1972.
- [3] R.P.V. Rao, R.D. Kriz, A.L. Abbott, C.J. Ribbens, "Parallel implementation of the filtered back projection algorithms for tomographic imaging," [http://www.sv.vt.edu/xray\\_ct/parallel/Parallel\\_CT.html](http://www.sv.vt.edu/xray_ct/parallel/Parallel_CT.html), 1995.
- [4] A. C. Kak, M. Slaney, "Principles of Computerized Tomographic Imaging", 1988, IEEE Press, New York.
- [5] R.H. Bracewell and A.C. Riddle, "Inversion of fan beam scans in radio astronomy," *Astrophysics Journal*, vol. 150, pp. 427 - 434, 1967.
- [6] G.N. Ramachandran and A.V. Lakshminarayanan, "Three dimensional reconstructions from radiographs and electron micrographs: Application of convolution instead of Fourier transforms," *Proceedings of the National Academy of Sciences*, vol. 68, pp. 2236 - 2240, 1971.
- [7] David S. Lalush, Miles N. Wernick, "Chapter 21-Iterative Image Reconstruction," *Emission Tomography (First Edition)*, 2004, Pages 443-472.



- [8] R. Gordon, R. Bender, and G. Herman, "Algebraic reconstruction techniques (ART) for three dimensional electron microscopy and X-ray photography," *Journal of Theoretical Biology*, vol. 36, pp. 105-117, 1970.
- [9] R. Gordon, "A tutorial on ART (Algebraic Reconstruction Techniques)," *IEEE Transactions on Nuclear Science*, vol. NS-21, pp. 78-93, 1974.
- [10] G. Herman and A. Naparstek, "Fast image reconstruction based on a Radon inversion formula appropriate for rapidly collected data," *SIAM Journal of Applied Mathematics*, vol. 33, pp. 511-533, 1976.
- [11] G. Herman and A. Lent, "Iterative reconstruction algorithms," *Comput. Biol. Med.*, vol. 6, pp. 273-294, 1976.
- [12] T. Budinger and G. Gullberg, "Three-dimensional reconstruction in nuclear medicine emission imaging," *IEEE Transactions on Nuclear Science*, vol. NS-21, pp. 2-21, 1974.
- [13] Beckmann, E. C. (January 2006). "CT scanning the early days," *The British Journal of Radiology* 79 (937): 5–8. doi:10.1259/bjr/29444122. PMID 16421398.
- [14] L. Shepp and B. Logan, "The Fourier reconstruction of a head section," *IEEE Transactions on Nuclear Science*, vol. NS-21, pp. 21-43, 1974.
- [15] Health Protection Agency, "X-ray safety leaflet," [www.hpa.org.uk](http://www.hpa.org.uk), Nov. 2007.
- [16] Létourneau EG, "I don't want an x-ray, Doctor: it's too dangerous," *Can Med Assoc J*. 1982 Dec 15; 127(12):1158-9.
- [17] Lautin EM, "CT As a Cause of Cancer: What is Old Is New Again," *AJR Am J Roentgenol*. 2001 Sep; 177(3):717.

[18] McCauley TR, "Radiation Risk of Screening CT," *AJR Am J Roentgenol*. 2003 Feb.; 180(2):540; author reply 540-1.

[19] Twombly R, "Full-Body CT Screening: Prevention or Producing Cancer," *Journal of the National Cancer Institute*, 2004 Nov; 96(22):1650-1.

[20] Diederich S, Lenzen H, "Radiation exposure associated with imaging of the chest: comparison of different radiographic and computed tomography techniques," *American Cancer Society*, 2000 Dec; 89(11 Suppl):2457-60.

[21] Linet MS, Kim KP, Rajaraman P., "Children's exposure to diagnostic medical radiation and cancer risk: epidemiologic and dosimetric considerations," *Pediatr Radiol*. 2009 Feb; 39 Suppl 1:S4-26. Epub 2008 Dec.

[22] Huda W, "Radiation doses and risks in chest computed tomography examinations," *Proc Am Thorac Soc*. 2007 Aug; 4(4):316-20.

[23] Hall EJ, Brenner DJ, "Cancer risks from diagnostic radiology," *Br J Radiol*. 2008 May; 81(965):362-78.

[24] Huang B, Law MW, Khong PL, "Whole-body PET/CT scanning: estimation of radiation dose and cancer risk," *Radiology*. 2009 Apr; 251(1):166-74.

[25] Brenner DJ, Elliston CD, "Estimated radiation risks potentially associated with full-body CT screening," *Radiology*. 2004 Sep; 232(3):735-8.

[26] Chodick G, Ronckers CM, Shalev V, Ron E., "Excess lifetime cancer mortality risk attributable to radiation exposure from computed tomography examinations in children," *Isr Med Assoc J*. 2007 Aug; 9(8):584-7.

[27] Brenner D, Elliston C, Hall E, Berdon W., "Estimated risks of radiation-induced fatal cancer from pediatric CT," *AJR Am J Roentgenol.* 2001 Feb; 176(2):289-96.

[28] Brenner DJ., "Radiation risks potentially associated with low-dose CT screening of adult smokers for lung cancer," *Radiology.* 2004 May; 231(2):440-5.

[29] Berrington de González A, Kim KP, Berg CD, "Low-dose lung computed tomography screening before age 55: estimates of the mortality reduction required to outweigh the radiation-induced cancer risk.," *J Med Screen.* 2008; 15(3):153-8.

[30] de Jong PA, Mayo JR, Golmohammadi K, Nakano Y, Lequin MH, Tiddens HA, Aldrich J, Coxson HO, Sin DD., "Estimation of cancer mortality associated with repetitive computed tomography scanning," *Am J Respir Crit Care Med.* 2006 Jan; 173(2):199-203.

[31] de González AB, Kim KP, Samet JM, "Radiation-induced cancer risk from annual computed tomography for patients with cystic fibrosis," *Am J Respir Crit Care Med.* 2007 Nov; 176(10):970-3.

[32] Griffey RT, Sodickson A, "Cumulative radiation exposure and cancer risk estimates in emergency department patients undergoing repeat or multiple CT," *AJR Am J Roentgenol.* 2009 Apr; 192(4):887-92.

[33] Smart RC, "What are the risks of diagnostic medical radiation?," *Med J Aust.* 1997 Jun; 166(11):589-91.

[34] Donnelly LF, Emery KH, Brody AS, Laor T, Gylys-Morin VM, Anton CG, Thomas SR, Frush DP, "Minimizing Radiation Dose for Pediatric Body Applications of Single-Detector Helical CT Strategies at a Large Children's Hospital," *Am. J. Roentgenol,* 176: 303-306, February 2001.

- [35] D.L. Donoho, M. Vetterli, R.A. DeVore, and I. Daubechies, “Data compression and harmonic analysis,” *IEEE Trans. Inform. Theory*, vol. 44, pp. 2435–2476, Oct. 1998.
- [36] M. Vetterli and J. Kovacevic, “Wavelets and Subband Coding. Englewood Cliffs,” NJ: Prentice-Hall, 1995.
- [37] I. Daubechies, “Ten Lectures on Wavelets,” Philadelphia, PA: SIAM, 1992.
- [38] S. Mallat, “A Wavelet Tour of Signal Processing,” 2nd ed. San Diego, CA: Academic, 1999.
- [39] W.B. Pennbaker and J.L. Mitchell, “JPEG Still Image Data Compression Standard,” New York: Springer-Verlag, 1993.
- [40] A. Skodras, C. Christopoulos, and T. Ebrahimi, “The JPEG2000 still image compression standard,” *IEEE Signal Processing Mag.*, vol. 18, pp. 36–58, Sept. 2001.
- [41] D.L. Donoho, “Compressed sensing,” *IEEE Trans. Inform. Theory*, vol. 52, no. 4, pp. 1289–1306, Apr. 2006.
- [42] E. Candès, J. Romberg, and T. Tao, “Stable signal recovery from incomplete and inaccurate measurements,” *Comm. Pure Appl. Math.*, vol. 59, no. 8, pp. 1207–1223, 2006.
- [43] “Compressive Sensing Resources [Online],” <http://dsp.rice.edu/cs>, last accessed date, January 2012.

[44] L Yu, X Liu, S Leng, JM Kofler, JC Ramirez-Giraldo, M Qu, J Christner, JG Fletcher & CH McCollough, “Radiation dose reduction in computed tomography techniques and future perspective,” *Future Medicine, Imaging in Medicine*, Vol. 1, No. 1, Pages 65-84, Oct 2009.

[45] CH McCollough, AN Primak, N Braun, J Kofler, “Strategies for Reducing Radiation Dose in CT,” *Radiologic Clinics of North America*, Volume 47, Issue 1, Pages 27-40, Jan 2009.

[46] E. Candès and T. Tao, “Near-optimal signal recovery from random projections and universal encoding strategies?” *IEEE Trans. Inform. Theory*, vol. 52, no. 12, pp. 5406–5245, Dec. 2006.

[47] E. Candès, J. Romberg, and T. Tao, “Robust uncertainty principles: Exact signal reconstruction from highly incomplete frequency information,” *IEEE Trans. Inform. Theory*, vol. 52, no. 2, pp. 489–509, Feb. 2006.

[48] M. Lustig, D. Donoho, and J.W. Pauly, “Sparse MRI: The application of compressed sensing for rapid MR imaging,” *Magnetic Resonance in Medicine*, vol. 58, no. 6, pp. 1182-1195, 2007.

[49] Lustig M, Lee JH, Donoho DL, Pauly JM. “Faster imaging with randomly perturbed, under-sampled spirals and  $\ell^1$  reconstruction,” *In Proceedings of the 13th Annual Meeting of ISMRM, Miami Beach*, 2005. p 685.

[50] Lustig M, Santos JM, Donoho DL, Pauly JM. “k-t SPARSE: High frame rate dynamic MRI exploiting spatio-temporal sparsity,” *In Proceedings of the 13th Annual Meeting of ISMRM, Seattle*, 2006. p 2420.

[51] Lustig M, Donoho DL and Pauly JM, “Rapid MR imaging with compressed sensing and randomly under-sampled 3DFT trajectories” *Proc. ISMRM (Seattle, WA)*, 2006.

- [52] Sidky E Y, Kao C-M and Pan X., “Accurate image reconstruction from few-views and limited-angle data in divergent-beam CT,” *J. X-ray Sci. Technol.* 14 119–39, 2006.
- [53] D. Xia, J. Bian, X. Han, E.Y. Sidky, X. Pan, “An Investigation of Compressive-sensing Image Reconstruction from Flying-focal-spot CT Data,” IEEE Nuclear Science Symposium Conf. Medical Imaging Magazine, pp. 3458–3462, May 2009.
- [54] G.H. Chen, J. Tang, S. Leng, “Prior Image Constrained Compressed Sensing (PICCS),” *Proc. SPIE 6856 685618*, 2008.
- [55] G T Herman and R Davidi, “Image reconstruction from a small number of projections,” *Inverse Problems*, 24-045011, Jun 2008.
- [56] H Yu, G Wang, “Compressed sensing based interior tomography,” *Physics in Medicine and Biology*, 54-2791, Apr 2009.
- [57] SJ LaRoque, EY Sidky, X Pan, “Accurate image reconstruction from few-view and limited-angle data in diffraction tomography,” *Journal of the Optical Society of America*, Vol. 25, Issue 7, pp. 1772-1782, Jun 2008.
- [58] X Jia, Y Lou, R Li, WY Song, SB Jiang, “GPU-based Fast Cone Beam CT Reconstruction from Undersampled and Noisy Projection Data via Total Variation,” Arxiv preprint arXiv:1002.3675, 2010.
- [59] EY Sidky, X Pan, SB Jiang, “Image reconstruction in circular cone-beam computed tomography by constrained, total-variation minimization,” *Physics in Medicine and Biology*, 53-4777, Aug 2008.
- [60] EY Sidky, MA Anastasio, X Pan, “Image reconstruction exploiting object sparsity in boundary-enhanced X-ray phase-contrast tomography,” *Optics Express*, Vol. 18, Issue 10, pp. 10404-10422, May 2010.

[61] Lin Yang, Yang Lu, and Ge Wang, "Compressed Sensing Inspired Image Reconstruction from Overlapped Projections," *International Journal of Biomedical Imaging*, vol. 2010, Article ID 284073, 8 pages, 2010. doi:10.1155/2010/284073

[62] A.Bicer, Z.Unver, "X-Ray Radiation Absorption Reduction by Second Order Cone Programming in Computerized Tomography Imaging," *IASTED Conference on Imaging and Signal Processing in Healthcare and Technology*, Washington, D.C., USA, 2011.

[63] Hengyong Yu , Changguo Ji , Ge Wang, "SART-type image reconstruction from a Limited Number of Projections with the Sparsity Constraints", *Journal of Biomedical Imaging*, 2011, p.1-7, January 2011

[64] Xiaochuan Pan et al., "Why do commercial CT scanners still employ traditional, filtered back-projection for image reconstruction," *2009 Inverse Problems* 25 123009.

[65] Jonathan R Shewchuk, "An Introduction to the Conjugate Gradient Method Without the Agonizing Pain," Technical report, CMU-CS-94-125, School of Computer Science, Carnegie Mellon University, Pittsburgh, PA, March 1994.

[66] M. Brooks, "A Survey of Algebraic Algorithms in Computerized Tomography," A Thesis Submitted in Partial Fulfillment of the Requirements for the Degree of Modeling and Computational Science (MSc), University of Ontario Institute of Technology, 2010.

[67] A.H. Andersen, A.C. Kak, "Simultaneous Algebraic Reconstruction Technique (SART): A superior implementation of the ART algorithm," *Ultrasonic Imaging*, Volume 6, Issue 1, January 1984, Pages 81-94.

[68] E. Candès and M.B.Wakin, "An Introduction to Compressive Sampling," *IEEE Signal Processing Magazine*, vol. 1, no. 2, pp. 21–30, Mar. 2008.

- [69] R.G. Baraniuc, “Lecture Notes on Compressive Sensing,” IEEE Signal Processing Magazine, vol. 25, no. 2, pp. 118–124, Mar. 2008.
- [70] E. Candès and J. Romberg, “ $l_1$  MAGIC: Recovery of Sparse Signals via Convex Programming,” a technical report, [www.acm.caltech.edu/l1magic](http://www.acm.caltech.edu/l1magic), October 2005.
- [71] E. Candès, “The Restricted Isometry Property and Its Implications for Compressed Sensing”, a preprint submitted to the Acadèmia des sience, Feb. 2008.
- [72] R. Baraniuk, M. Davenport, R. DeVore, and M. Wakin, “A simple proof of the restricted isometry property for random matrices,” *Constructive Approximation*, vol. 28, no. 3, pp. 253-263, 2008.
- [73] J. Romberg, “Imaging via Compressive Sampling,” IEEE Signal Processing Magazine, vol. 25, no. 2, pp. 14–20, Mar. 2008.
- [74] Xu, H. K., Kim, T. H., “Primary Title: Convergence of Hybrid Steepest-Descent Methods for Variational Inequalities,” *Journal of Optimization Theory and Applications*, vol. 119, no. 1, pp. 185-201, October 2003.
- [75] Wang G. and Jiang M., “Ordered-subset simultaneous algebraic reconstruction techniques (OS-SART)” *J. X-Ray Sci. Technol.* 12 169–77, 2004.
- [76] M. Slaney and A. C. Kak, “Diffraction tomography,” in *Inverse Optics*, Vol. 14, A. J. Devaney, ed. (SPIE, 1983), pp. 2–19.
- [77] Miguel Sousa Lobo, Lieven Vandenberghe, Stephen Boyd, Hervé Lebrét, “Applications of second-order cone programming,” *Linear Algebra and its Applications*, Volume 284, Issues 1-3, 15 November 1998, Pages 193-228, ISSN 0024-3795, 10.1016/S0024-3795(98)10032-0.



[78] F. Alizadeh, D. Goldfarb, "Second-Order Cone Programming," *Mathematical Programming*, Volume 95, Number 1, 3-51, DOI: 10.1007/s10107-002-0339-5.

[79] S. Boyd and L. Vandenberghe, *Convex Optimization*. Cambridge, U.K.: Cambridge Univ. Press, 2004.

[80] Paige, C. C. and M. A. Saunders, "Solution of Sparse Indefinite Systems of Linear Equations," *SIAM J. Numer. Anal.*, Vol.12, 1975, pp. 617-629.

## APPENDIX A

### PROJECTION GEOMETRY

#### A.1 Ray Equation

We give illustrations of the following cases:

Table A.1.1: Projection line cases.

|        |                            |            |
|--------|----------------------------|------------|
| Case 1 | $0 \leq \theta \leq \pi/2$ | $t \geq 0$ |
| Case 2 | $0 \leq \theta \leq \pi/2$ | $t < 0$    |
| Case 3 | $\pi/2 < \theta \leq \pi$  | $t \geq 0$ |
| Case 4 | $\pi/2 < \theta \leq \pi$  | $t < 0$    |

Case 1:  $0 \leq \theta \leq \frac{\pi}{2}$ ,  $0 \leq t$

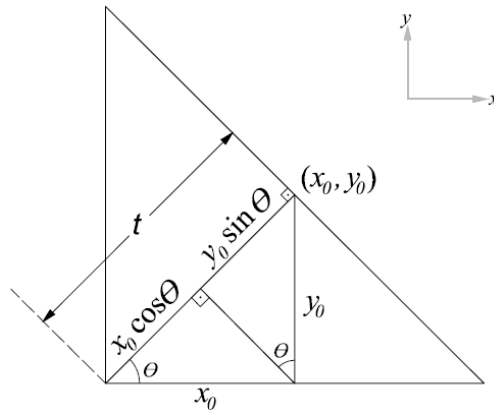


Fig. A.1.1: Ray equation, case 1

$$x_0 \cos \theta + y_0 \sin \theta = t \tag{A.1.1}$$

Case 2:  $0 \leq \theta \leq \frac{\pi}{2}$ ,  $t < 0$

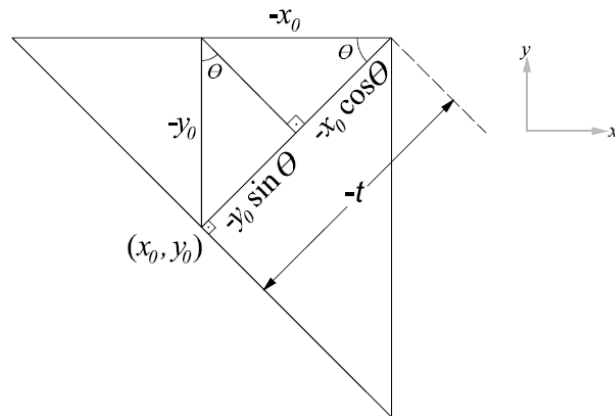


Fig. A.1.2: Ray equation, case 2

$$\begin{aligned} -x_0 \cos \theta - y_0 \sin \theta &= -t \\ x_0 \cos \theta + y_0 \sin \theta &= t \end{aligned} \tag{A.1.2}$$

Case 3:  $\frac{\pi}{2} < \theta \leq \pi$ ,  $0 \leq t$

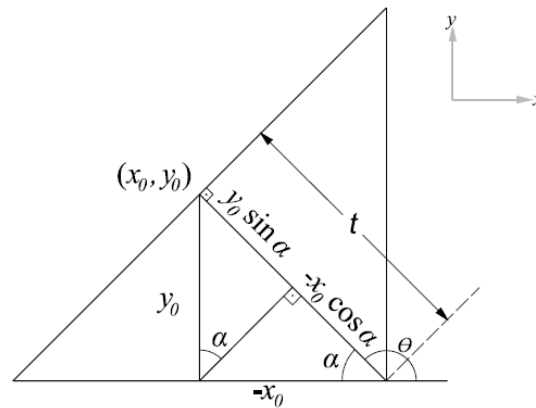


Fig. A.1.3: Ray equation, case 3

$$\begin{aligned} -x_0 \cos \alpha + y_0 \sin \alpha &= t \\ x_0 \cos \theta + y_0 \sin \theta &= t \end{aligned} \tag{A.1.3}$$

Case 4:  $\frac{\pi}{2} < \theta \leq \pi$ ,  $t < 0$

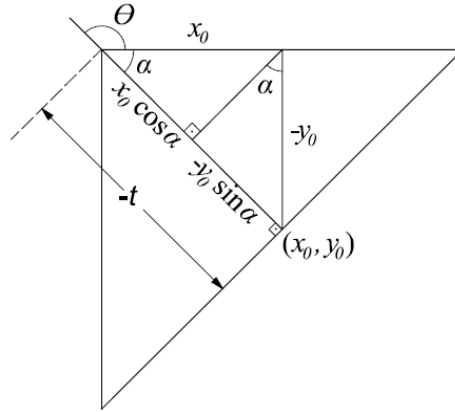


Fig. A.1.4: Ray equation, case 4

$$\begin{aligned}
 x_0 \cos \alpha - y_0 \sin \alpha &= -t \\
 -x_0 \cos \theta - y_0 \sin \theta &= -t \\
 x_0 \cos \theta + y_0 \sin \theta &= t
 \end{aligned}
 \tag{A.1.4}$$

The resultant ray equations in four cases are the same. Given a fixed  $\theta$  and  $t$  value in any case, any point on the ray line satisfies the ray equations. Therefore, (A.1.1)-(A.1.4) can be written in more general form as

$$x \cos \theta + y \sin \theta = t \tag{A.1.5}$$

## A.2 Fan Beam Geometry

We give illustrations of the cases in Table A.2.1. Angular unit is taken as degrees.

Table A.2.1: Fan beam projection cases.

|        |                |            |                   |
|--------|----------------|------------|-------------------|
| Case 1 | $\beta \geq 0$ | $t \geq 0$ | $\gamma_m \geq 0$ |
| Case 2 | $\beta \geq 0$ | $t \geq 0$ | $\gamma_m < 0$    |
| Case 3 | $\beta \geq 0$ | $t < 0$    | $\gamma_m \geq 0$ |
| Case 4 | $\beta \geq 0$ | $t < 0$    | $\gamma_m < 0$    |
| Case 5 | $\beta < 0$    | $t \geq 0$ | $\gamma_m \geq 0$ |
| Case 6 | $\beta < 0$    | $t \geq 0$ | $\gamma_m < 0$    |
| Case 7 | $\beta < 0$    | $t < 0$    | $\gamma_m \geq 0$ |
| Case 8 | $\beta < 0$    | $t < 0$    | $\gamma_m < 0$    |

Case 1:  $\beta \geq 0$ ,  $t \geq 0$ ,  $\gamma_m \geq 0$

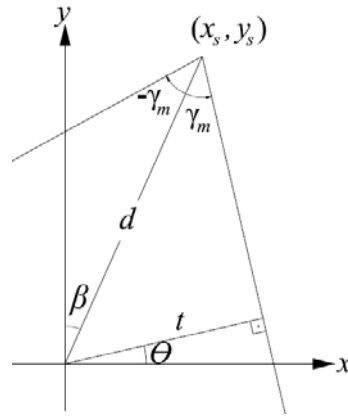


Fig. A.2.1: Fan geometry, case 1

$$\begin{aligned} \theta &= 90 - (\beta + (90 - \gamma_m)) = -(\beta - \gamma_m) \\ (x_s, y_s) &= (d \sin \beta, d \cos \beta) \\ t &= x_s \cos \theta + y_s \sin \theta \end{aligned} \tag{A.2.1}$$

Case 2:  $\beta \geq 0$ ,  $t \geq 0$ ,  $\gamma_m < 0$

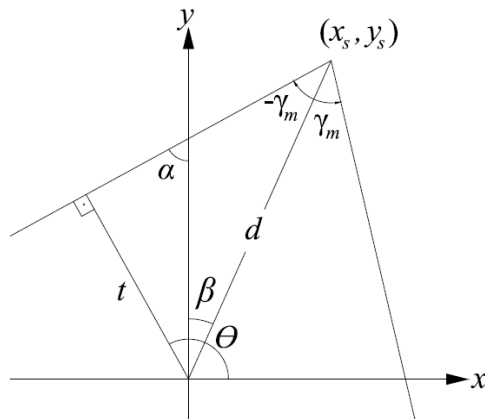


Fig. A.2.2: Fan geometry, case 2

$$\begin{aligned} \theta &= 90 - \alpha + 90 = 180 - (\beta - \gamma_m) \\ (x_s, y_s) &= (d \sin \beta, d \cos \beta) \\ t &= x_s \cos \theta + y_s \sin \theta \end{aligned} \tag{A.2.2}$$

Case 3:  $\beta \geq 0$ ,  $t < 0$ ,  $\gamma_m \geq 0$

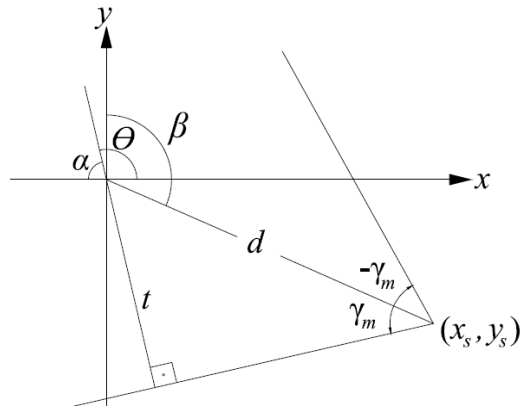


Fig. A.2.3: Fan geometry, case 3

$$\theta = 180 - \alpha = 180 - (\beta - 90 + 90 - \gamma_m) = 180 - (\beta - \gamma_m)$$

$$(x_s, y_s) = (d \sin \beta, d \cos \beta)$$

$$t = x_s \cos \theta + y_s \sin \theta$$

(A.2.3)

Case 4:  $\beta \geq 0$ ,  $t < 0$ ,  $\gamma_m < 0$

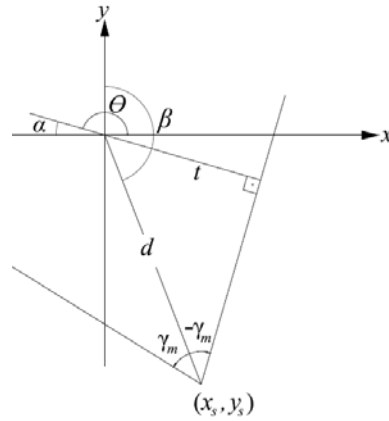


Fig. A.2.4: Fan geometry, case 4

$$\theta = 180 - \alpha = 180 - (\beta - (90 - (-\gamma_m)) - 90) = 360 - (\beta - \gamma_m)$$

$$(x_s, y_s) = (d \sin \beta, d \cos \beta)$$

$$t = x_s \cos \theta + y_s \sin \theta$$

(A.2.4)

Case 5:  $\beta < 0$ ,  $t \geq 0$ ,  $\gamma_m \geq 0$

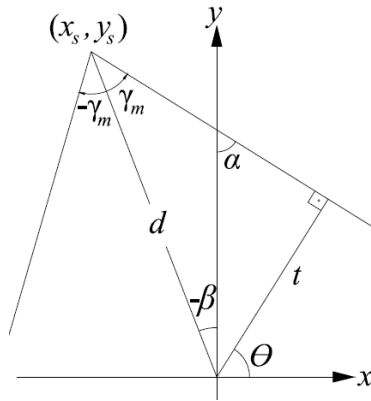


Fig. A.2.5: Fan geometry, case 5

$$\begin{aligned}
 \theta &= \alpha = -(\beta - \gamma_m) \\
 (x_s, y_s) &= (d \sin \beta, d \cos \beta) \\
 t &= x_s \cos \theta + y_s \sin \theta
 \end{aligned}
 \tag{A.2.5}$$

Case 6:  $\beta < 0$ ,  $t \geq 0$ ,  $\gamma_m < 0$

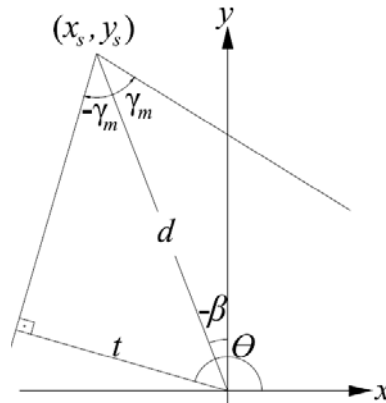


Fig. A.2.6: Fan geometry, case 6

$$\begin{aligned}
 \theta &= 90 - (-\gamma_m) + (-\beta) = 180 - (\beta - \gamma_m) \\
 (x_s, y_s) &= (d \sin \beta, d \cos \beta) \\
 t &= x_s \cos \theta + y_s \sin \theta
 \end{aligned}
 \tag{A.2.6}$$

Case 7:  $\beta < 0$ ,  $t < 0$ ,  $\gamma_m \geq 0$

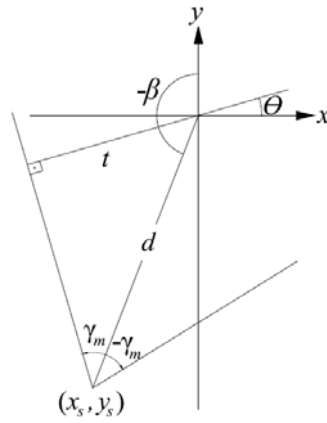


Fig. A.2.7: Fan geometry, case 7

$$\theta = -\beta - 90 - (90 - \gamma_m) = -180 - (\beta - \gamma_m)$$

$$(x_s, y_s) = (d \sin \beta, d \cos \beta)$$

$$t = x_s \cos \theta + y_s \sin \theta$$

(A.2.7)

Case 8:  $\beta < 0$ ,  $t < 0$ ,  $\gamma_m < 0$

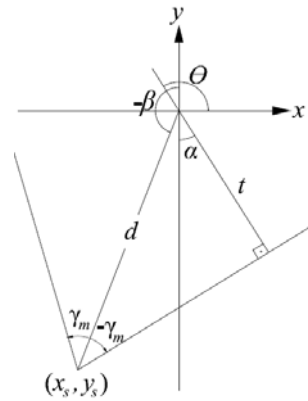


Fig. A.2.8: Fan geometry, case 8

$$\theta = 90 + \alpha = 90 + (90 - ((-\gamma_m) + (180 - (-\beta)))) = -(\beta - \gamma_m)$$

$$(x_s, y_s) = (d \sin \beta, d \cos \beta)$$

$$t = x_s \cos \theta + y_s \sin \theta$$

(A.2.8)



## APPENDIX B

### LOGARITHMIC BARRIER METHOD FOR SOCP

#### B.1 Total Variation Minimization with Equality Constraints

Consider the problem,

$$\begin{aligned} \min_{u,x} \sum_j u_j \quad \text{subject to} \quad & \|D_j x\|_2 \leq u_j \\ & Wx = P \end{aligned} \tag{B.1.1}$$

After defining the inequality functions as second order conic

$$\frac{1}{2} \left( \|D_j x\|_2^2 - u_j^2 \right) \tag{B.1.2}$$

the inequality constraints are incorporated into the objective function by means of the logarithmic barrier method:

$$\min_{u,x} \left[ 1^T u + \frac{1}{\tau^k} \sum_{j=1}^N -\log \frac{1}{2} \left( u_j^2 - \|D_j x\|_2^2 \right) \right] \quad \text{subject to} \quad Wx = P \tag{B.1.3}$$

We turn briefly away from solving (B.1.3) to investigate the solution of a more general problem,

$$\min_z \left[ f(z) + \frac{1}{\tau} \phi(z) \right] \quad \text{subject to} \quad Az = b \tag{B.1.4}$$

where  $z$  is a vectorial variable and  $\phi(z)$  is the logarithmic barrier function. The equality constraints are incorporated into the objective function using the Lagrange multipliers  $\nu$ ,

$$\min_z \left[ f(z) + \frac{1}{\tau} \phi(z) + v^T (Az - b) \right] \quad (\text{B.1.5})$$

Problem (B.1.5) can be solved using Newton's method. The quadratic approximation of the objective function

$$g(z) = f(z) + \frac{1}{\tau} \phi(z) + v^T (Az - b) \quad (\text{B.1.6})$$

around a point  $z$  is given by

$$g(z + \Delta z) \approx g(z) + \Delta z^T g_z + \frac{1}{2} \Delta z^T H_z \Delta z = q(z + \Delta z) \quad (\text{B.1.7})$$

where  $g_z$  is the gradient and  $H_z$  is the Hessian matrix,

$$g_z = \nabla f(z) + \frac{1}{\tau} \nabla \phi(z) + A^T v \quad (\text{B.1.8})$$

$$H_z = \nabla^2 f(z) + \frac{1}{\tau} \nabla^2 \phi(z) \quad (\text{B.1.9})$$

The  $\Delta z$  that minimizes  $q(z + \Delta z)$  in (B.1.7) is obtained by setting its derivative to zero:

$$\frac{\partial}{\partial \Delta z} q(z + \Delta z) = g_z + H_z \Delta z = 0 \quad (\text{B.1.10})$$

Suppose  $z$  is a feasible point, i.e.,  $Az = b$ . The new point,  $(z + \Delta z)$  should also satisfy the constraint, i.e.,  $A(z + \Delta z) = b$ , requiring  $A\Delta z = 0$ . Therefore,  $\Delta z$  and  $v$  are obtained by solving the following system of linear equations:

$$H_z \Delta z = -g_z \quad (\text{B.1.11})$$

$$A\Delta z = 0 \quad (\text{B.1.12})$$

Let the term  $\nabla f(z) + (1/\tau)\nabla \phi(z)$  in the right hand side of (B.1.8) be expressed by  $g_0$ . Then, (B.1.11)-(B.1.12) can be written in matrix form:

$$\begin{bmatrix} H_z & A^T \\ A & 0 \end{bmatrix} \begin{bmatrix} \Delta z \\ v \end{bmatrix} = \begin{bmatrix} -g_0 \\ 0 \end{bmatrix} \quad (\text{B.1.13})$$

Suppose  $f(z)$  and  $\phi(z)$  are in the form of

$$f(z) = c_0^T z \quad (\text{B.1.14})$$

$$\phi(z) = \sum_{j=1}^N -\log(g_j(z)) \quad (\text{B.1.15})$$

where  $g_j(z)$  is either a linear or second-order conic function. Then, (B.1.13) defines a symmetric but not necessarily positive definite system. It can be solved using SMMLQ algorithm when the problem is large-scale. The minimization of (B.1.4) requires solving (B.1.13) repeatedly with a new  $\tau^k > \tau^{k-1} > 0$  ( $k$  is the log-barrier iteration index). Using the Newton step direction  $\Delta z$ , the new point  $z + \Delta z$  is set as a starting point of the next iteration.

For future reference, we note that the gradients of  $f(z)$  and  $\phi(z)$  are

$$\nabla f(z) = c_0 \quad (\text{B.1.16})$$

$$\nabla \phi(z) = \sum_{j=1}^N \frac{1}{g_j(z)} \nabla g_j(z) \quad (\text{B.1.17})$$

and the Hessians are given by

$$\nabla^2 f(z) = 0 \quad (\text{B.1.18})$$

$$\nabla^2 \phi(z) = \sum_{j=1}^N \frac{1}{g_j(z)^2} \nabla g_j(z) \nabla g_j(z)^T + \sum_{j=1}^N \frac{1}{g_j(z)} \nabla^2 g_j(z) \quad (\text{B.1.19})$$

As analogous to the way of solving problem (B.1.4), (B.1.3) can be solved for a two-vectorial variable  $z = [x^T, u^T]^T$ . That is, (B.1.3) is rewritten as

$$\min_{x,u} g(x,u) \quad (\text{B.1.20})$$

with

$$g(x, u) = 1^T u + \frac{1}{\tau^k} \sum_j -\log \frac{1}{2} \left( u^T \delta_j \delta_j^T u - \|D_j x\|_2^2 \right) + v^T (Wx - P) \quad (\text{B.1.21})$$

(B.1.21) is in the same form as (B.1.6) with the analogy that

$$f(x, u) = 1^T u \quad (\text{B.1.22})$$

$$\phi(x, u) = \sum_{j=1}^N -\log(-g_j(x, u)) \quad (\text{B.1.23})$$

$$g_j(x, u) = \frac{1}{2} \left( \|D_j x\|_2^2 - \|\delta_j^T u\|_2^2 \right) \quad (\text{B.1.24})$$

The gradients are

$$\nabla f(x, u) = \begin{bmatrix} \nabla_x f(x, u) \\ \nabla_u f(x, u) \end{bmatrix} = \begin{bmatrix} 0 \\ 1 \end{bmatrix} \quad (\text{B.1.25})$$

$$\nabla g_j(x, u) = \begin{bmatrix} \nabla_x g_j(x, u) \\ \nabla_u g_j(x, u) \end{bmatrix} = \begin{bmatrix} D_j^T D_j x \\ -\delta_j \delta_j^T u \end{bmatrix} \quad (\text{B.1.26})$$

$$\nabla \phi(x, u) = \sum_{j=1}^N \frac{1}{-g_j(x, u)} \begin{bmatrix} D_j^T D_j x \\ -\delta_j \delta_j^T u \end{bmatrix} \quad (\text{B.1.27})$$

and expressions needed for the Hessian are given by

$$\nabla g_j(x, u) \nabla g_j(x, u)^T = \begin{bmatrix} D_j^T D_j x x^T D_j^T D_j & -D_j^T D_j x u^T \delta_j \delta_j^T \\ -\delta_j \delta_j^T u x^T D_j^T D_j & \delta_j \delta_j^T u u^T \delta_j \delta_j^T \end{bmatrix} \quad (\text{B.1.28})$$

$$\nabla^2 g_j(x, u) = \begin{bmatrix} \nabla_x (\nabla_x g_j(x, u)) & \nabla_x (\nabla_u g_j(x, u)) \\ \nabla_u (\nabla_x g_j(x, u)) & \nabla_u (\nabla_u g_j(x, u)) \end{bmatrix} = \begin{bmatrix} D_j^T D_j & 0 \\ 0 & -\delta_j \delta_j^T \end{bmatrix} \quad (\text{B.1.29})$$

The expressions (B.1.25)-(B.1.29) are used to form system of equations in (B.1.13) which is solved for  $\Delta z = [\Delta x^T, \Delta u^T]^T$ . It is possible to reduce the size of the Newton system by eliminating  $\Delta u$  from (B.1.13) (see [70]).

## B.2 Total Variation Minimization with Quadratic Constraints

Consider the problem,

$$\begin{aligned} \min_{u, x} \sum_j u_j \quad \text{subject to} \quad & \|D_j x\| \leq u_j, \\ & \|Wx - P\| \leq \varepsilon \end{aligned} \quad (\text{B.2.1})$$

After defining the inequality functions as second order conic

$$\frac{1}{2} \left( \|D_j x\|_2^2 - u_j^2 \right) \quad (\text{B.2.2})$$

$$\frac{1}{2} \left( \|Wx - P\|_2^2 - \varepsilon^2 \right) \quad (\text{B.2.3})$$

the inequality constraints are incorporated into the objective function by means of the logarithmic barrier method:

$$\min_{u,x} \left[ 1^T u + \frac{1}{\tau^k} \left[ \sum_{j=1}^N -\log \frac{1}{2} \left( \|D_j x\|_2^2 - u_j^2 \right) - \log \frac{1}{2} \left( \varepsilon^2 - \|Wx - P\|_2^2 \right) \right] \right] \quad (\text{B.2.4})$$

We turn briefly away from solving (B.2.4) to investigate the solution of a more general problem,

$$\min_z \left[ f(z) + \frac{1}{\tau} \phi(z) \right] \quad (\text{B.2.5})$$

where  $z$  is a vectorial variable and  $\phi(z)$  is the logarithmic barrier function. Problem (B.2.5) can be solved using Newton's method. The quadratic approximation of the objective function,

$$g(z) = f(z) + \frac{1}{\tau} \phi(z) \quad (\text{B.2.6})$$

around a point  $z$  is given by

$$g(z + \Delta z) \approx g(z) + \Delta z^T g_z + \frac{1}{2} \Delta z^T H_z \Delta z = q(z + \Delta z) \quad (\text{B.2.7})$$

where  $g_z$  is the gradient and  $H_z$  is the Hessian matrix,

$$g_z = \nabla f(z) + \frac{1}{\tau} \nabla \phi(z) \quad (\text{B.2.8})$$

$$H_z = \nabla^2 f(z) + \frac{1}{\tau} \nabla^2 \phi(z) \quad (\text{B.2.9})$$

The  $\Delta z$  that minimizes  $q(z+\Delta z)$  in (B.2.7) is obtained by setting its derivative to zero:

$$\frac{\partial}{\partial \Delta z} q(z + \Delta z) = g_z + H_z \Delta z = 0 \quad (\text{B.2.10})$$

Therefore,  $\Delta z$  are obtained by solving the following system of linear equations:

$$H_z \Delta z = -g_z \quad (\text{B.2.11})$$

Suppose  $f(z)$  and  $\phi(z)$  are in the form of

$$f(z) = c_0^T z \quad (\text{B.2.12})$$

$$\phi(z) = \sum_{j=1}^N -\log(g_j(z)) - \log(g_\varepsilon(z)) \quad (\text{B.2.13})$$

where  $g_j(z)$  and  $g_\varepsilon(z)$  are either linear or second-order conic functions. Then, (B.2.11) defines a symmetric, positive definite system. It can be solved using CG algorithm when the problem is large-scale. The minimization of (B.2.5) requires solving (B.2.11) repeatedly with a new  $\tau^k > \tau^{k-1} > 0$  ( $k$  is the log-barrier iteration index). Using the Newton step direction  $\Delta z$ , the new point  $z+\Delta z$  is set as a starting point of the next iteration.

For future reference, we note that the gradients of  $f(z)$  and  $\phi(z)$  are

$$\nabla f(z) = c_0 \quad (\text{B.2.14})$$

$$\nabla \phi(z) = \sum_{j=1}^N \frac{1}{-g_j(z)} \nabla g_j(z) + \frac{1}{-g_\varepsilon(z)} \nabla g_\varepsilon(z) \quad (\text{B.2.15})$$

and the Hessians are given by

$$\nabla^2 f(z) = 0 \quad (\text{B.2.16})$$

$$\begin{aligned} \nabla^2 \phi(z) = & \sum_{j=1}^N \frac{1}{g_j(z)^2} \nabla g_j(z) \nabla g_j(z)^T + \sum_{j=1}^N \frac{1}{-g_j(z)} \nabla^2 g_j(z) + \\ & \frac{1}{g_\varepsilon(z)^2} \nabla g_\varepsilon(z) \nabla g_\varepsilon(z)^T + \frac{1}{-g_\varepsilon(z)} \nabla^2 g_\varepsilon(z) \end{aligned} \quad (\text{B.2.17})$$

As analogous to the way of solving problem (B.2.5), (B.2.4) can be solved for a two-vectorial variable  $z = [x^T, u^T]^T$ . That is, (B.2.4) is rewritten as

$$\min_{x,u} g(x,u) \quad (\text{B.2.18})$$

with

$$g(x,u) = 1^T u + \frac{1}{\tau^k} \sum_j -\log \frac{1}{2} \left( u^T \delta_j \delta_j^T u - \|D_j x\|_2^2 \right) - \log \frac{1}{2} \left( \varepsilon^2 - \|Wx - P\|_2^2 \right) \quad (\text{B.2.19})$$

(B.2.19) is in the same form as (B.2.6) with the analogy that

$$f(x,u) = 1^T u \quad (\text{B.2.20})$$

$$\phi(x,u) = \left( \sum_{j=1}^N -\log(-g_j(x,u)) \right) - \log(-g_\varepsilon(x,u)) \quad (\text{B.2.21})$$

$$g_j(x,u) = \frac{1}{2} \left( \|D_j x\|_2^2 - \|\delta_j^T u\|_2^2 \right) \quad (\text{B.2.22})$$

$$g_\varepsilon(x,u) = \frac{1}{2} \left( \|Wx - P\|_2^2 - \varepsilon^2 \right) \quad (\text{B.2.23})$$

The gradients are

$$\nabla f(x,u) = \begin{bmatrix} \nabla_x f(x,u) \\ \nabla_u f(x,u) \end{bmatrix} = \begin{bmatrix} 0 \\ 1 \end{bmatrix} \quad (\text{B.2.24})$$

$$\nabla g_j(x,u) = \begin{bmatrix} \nabla_x g_j(x,u) \\ \nabla_u g_j(x,u) \end{bmatrix} = \begin{bmatrix} D_j^T D_j x \\ -\delta_j \delta_j^T u \end{bmatrix} \quad (\text{B.2.25})$$

$$\nabla g_\varepsilon(x,u) = \begin{bmatrix} \nabla_x g_\varepsilon(x,u) \\ \nabla_u g_\varepsilon(x,u) \end{bmatrix} = \begin{bmatrix} W^T (Wx - P) \\ 0 \end{bmatrix} \quad (\text{B.2.26})$$

$$\nabla \phi(x,u) = \sum_{j=1}^N \frac{1}{-g_j(x,u)} \begin{bmatrix} D_j^T D_j x \\ -\delta_j \delta_j^T u \end{bmatrix} + \frac{1}{-g_\varepsilon(x,u)} \begin{bmatrix} W^T (Wx - P) \\ 0 \end{bmatrix} \quad (\text{B.2.27})$$

and expressions needed for the Hessian are given by

$$\nabla g_j(x,u) \nabla g_j(x,u)^T = \begin{bmatrix} D_j^T D_j x x^T D_j^T D_j & -D_j^T D_j x u^T \delta_j \delta_j^T \\ -\delta_j \delta_j^T u x^T D_j^T D_j & \delta_j \delta_j^T u u^T \delta_j \delta_j^T \end{bmatrix} \quad (\text{B.2.28})$$

$$\nabla^2 g_j(x,u) = \begin{bmatrix} \nabla_x (\nabla_x g_j(x,u)) & \nabla_x (\nabla_u g_j(x,u)) \\ \nabla_u (\nabla_x g_j(x,u)) & \nabla_u (\nabla_u g_j(x,u)) \end{bmatrix} = \begin{bmatrix} D_j^T D_j & 0 \\ 0 & -\delta_j \delta_j^T \end{bmatrix} \quad (\text{B.2.29})$$

$$\nabla g_\varepsilon(x,u)\nabla g_\varepsilon(x,u)^T = \begin{bmatrix} W^T(Wx-P)(Wx-P)^T W & 0 \\ 0 & 0 \end{bmatrix} \quad (\text{B.2.30})$$

$$\nabla^2 g_\varepsilon(x,u) = \begin{bmatrix} \nabla_x(\nabla_x g_\varepsilon(x,u)) & \nabla_x(\nabla_u g_\varepsilon(x,u)) \\ \nabla_u(\nabla_x g_\varepsilon(x,u)) & \nabla_u(\nabla_u g_\varepsilon(x,u)) \end{bmatrix} = \begin{bmatrix} W^T W & 0 \\ 0 & 0 \end{bmatrix} \quad (\text{B.2.31})$$

The expressions (B.2.28)-(B.2.31) are used to form system of equations in (B.2.11) which is solved for  $\Delta z = [\Delta x^T, \Delta u^T]^T$ . It is possible to reduce the size of the Newton system by eliminating  $\Delta u$  from (B.2.11) (see [70]).



## CURRICULUM VITAE

### PERSONAL INFORMATION

Surname, Name: Biçer, Aydın  
Nationality: Turkish (TC)  
Date and Place of Birth: 14 October 1978, Çorum  
Phone: +90 312 8475300 - 4983  
Fax: +90 312 847 5320  
email: [abicer@aselsan.com.tr](mailto:abicer@aselsan.com.tr)

### EDUCATION

| Degree | Institution                           | Year of Graduation |
|--------|---------------------------------------|--------------------|
| M.Sc.  | METU, Electrical and Electronics Eng. | 2005               |
| B.Sc.  | METU, Electrical and Electronics Eng. | 2000               |

### WORK EXPERIENCE

| Year         | Position                                     |
|--------------|--|
| 2010-Present | ASELSAN Inc. Software Design Leader          |
| 2007-2010    | ASELSAN Inc. Senior Expert Software Engineer |
| 2004-2007    | ASELSAN Inc. Expert Software Engineer        |
| 2000-2004    | ASELSAN Inc. Software Engineer               |
| 1999-2000    | ASELSAN Inc. Part-time Researcher            |